





# Colloidal Quantum Dots as the Active Material for Silicon Nitride Photonics

Colloïdale 'quantum dots' als actief materiaal voor geïntegreerde fotonische circuits  
in siliciumnitride

Yunpeng Zhu

Promotoren: prof. dr. ir. D. Van Thourhout, prof. dr. ir. Z. Hens  
Proefschrift ingediend tot het behalen van de graad van  
Doctor in de ingenieurswetenschappen: fotonica

Vakgroep Informatietechnologie  
Voorzitter: prof. dr. ir. B. Dhoedt  
Faculteit Ingenieurswetenschappen en Architectuur

Vakgroep Chemie  
Voorzitter: prof. dr. I. Van Driessche  
Faculteit Wetenschappen

Academiejaar 2017 - 2018



UNIVERSITEIT  
GENT

ISBN 978-94-6355-126-7

NUR 965, 971

Wettelijk depot: D/2018/10.500/44

**Promotor:**

Prof. dr. ir. Dries Van Thourhout  
Prof. dr. ir. Zeger Hens

**Examencommissie:**

Prof. dr. ir. Daniël De Zutter (voorzitter)	Universiteit Gent
Prof. dr. ir. Dries Van Thourhout (Promotor)	Universiteit Gent
Prof. dr. ir. Zeger Hens (Promotor)	Universiteit Gent
Prof. dr. ir. Iwan Moreels	Universiteit Gent
Prof. dr. ir. Nicolas Le Thomas	Universiteit Gent
Prof. dr. Johan Lauwaert	Universiteit Gent
Prof. dr. ir. Pascal Kockaert	Université libre de Bruxelles
Dr. ir. Pieter Geiregat	Universiteit Gent

Universiteit Gent  
Faculteit Ingenieurswetenschappen en Architectuur

Vakgroep Informatietechnologie  
Technologiepark-Zwijnaarde 15, B-9052 Gent, België

Tel.: +32-9-264.33.30

Fax.: +32-9-331.35.93



# Dankwoord

Before I start my master degree, I have no idea where the city Ghent is. The Belgium country is just a name for me. However, as a master student who was studying integrated photonics, I have read a lot of papers from Photonics Research Group (PRG) at Ghent University. These papers are well written which act as most cited papers in the integrated/silicon photonics field. By tracking down to the group website, I was astonished by the well-organized layout. Moreover, visitors can download these papers freely, which is not common but quite useful for junior researchers like me. Another advantage of the group website is that it always posts vacancies on the main page. Some of these topics are quite interesting which also encourage me to pursue a PhD degree.

I was lucky that I got accepted as a PhD student and became one member of the PRG family. My research topic is combining novel light emitting material, colloidal quantum dots (CQDs), with the integrated silicon nitride (SiN) photonics platform. The original ambitious goal seems to be pretty straightforward. However, the path towards the final goal is full of obstacles, challenges and failures. These difficulties can really result in a fading enthusiasm for my PhD topic. Without the support from the professors, colleagues, friends and family, I would not be able to conquer all these difficulties and finish my degree. Here, I would like to take the chance to thank you all.

First and foremost, I would like to thank my promotor Prof. Dries Van Thourhout, for providing me two opportunities to work in the PRG group. I can still remember the weekly meeting with him, during which I have learned a lot from his valuable suggestions for my first year PhD. As a professor who has been working in integrated photonics area for more than 20 years, his experience can always point me the right direction. He encourages me to try new ideas, and I cherish this kind of freedom for my PhD study.

I would like to also thank my co-promotor Prof. Zeger Hens from the group of Physics and Chemistry of Nanostructures in Ghent University. Although he is a professor from Chemistry department, I was astonished by his solid foundation in physics and mathematics. His expertise in CQDs helped me a lot. I would like to also thank Dr. Edouard Brainis for his help on single photon project. Dr. Pieter Geiregat, we will never make a working laser without your belief and

enthusiasm on CQDs lasing. I wish you a good academic career in the future. Dr. Suzanne Bisschop, thanks for your help on provide CQDs information and gain measurement.

I would like to also thank the jury members of my PhD defense, Prof. Iwan Moreels, Prof. Nicolas Le Thomas, Prof. Johan Lauwaert, Prof. Pascal Kockaert, for their careful review of my thesis and valuable comments, suggestions and questions.,

My special thanks to Prof. Yuqing Jiao from TU/e. Our friendship starts from the cleanroom of Zhejiang University. I can still remember the nights we spend together preparing silica integrated circuit samples, which is about nine years ago. Who knows that the same experience would happen again in Europe, in the cleanroom of TU/e, where you helped me to prepare ebeam samples also during the night? I cannot finish my PhD without your selfless help. I cherish our friendship and wish you the best in your future academic career.

I would like to also thank Dr. Weiqiang Xie. You help me a lot for providing me tricks for SiN and CQDs sample preparation. Together we fabricated and characterized the lowest loss SiN waveguide and the highest Q SiN ring resonator in UGent; the 1<sup>st</sup> integrated CQDs lasers in the world. All these experiences will always be treasuries for me.

PRG is like a big family to everybody in the group. I would like to express my gratitude to our group leader Prof. Roel Baets, who always makes his best effort to make PRG group more open and friendly. I am very happy to work in this big family. I would like to express my thanks to our administrative team in our group, Ilse Van Royen, Kristien De Meulder, Ilse Meersman, Mike Van Puyenbroeck, Bert Coryn; to our technical staff, Liesbet Van Landschoot, Steven Verstuyft, Muhammad Muneeb, Michael Vanslembrouck; to my colleagues who share their experience and knowledge with me, Ananth Subramanian, Amin Abbasi, Thijs Spuesens, Francois Leo, Pijush Kumar Pal, Ashwyn Srinivasan, Chandrasekaran Vigneshwaran and Lukas Elsinger.

I wish to thank my Chinese colleagues: Yufei, Bin, Chen, Yu, Hui, Yanlu, Zhechao, Ruijun, Lianyan, Jing, Haolan, Ang, Haifeng, Xin, Qiangsheng, Jie, Xiaomin, Yuting, Xiaoning, Yuxin, Ye, Guanyu, Jinghao, Qiang, Zhengzhou, Chonghuai, Mi and Yang; my friends in Europe: Mengfei, Youxuan, Xiaogang, Shidan, Yunfeng and Qizhi. With you guys, I felt less lonely in Europe.

Lastly, I would like to thank my parents, who love and support me unconditionally. It is time for me to give a period to my studying career and start to take care of you two. Special thanks to Xi, who gives me company during my thesis writing period.

*Hangzhou, May 2018*  
*Yunpeng Zhu*

# Table of Contents

<b>Dankwoord</b> .....	<b>i</b>
<b>Nederlandse samenvatting</b> .....	<b>xxi</b>
<b>English summary</b> .....	<b>xxv</b>
<b>1 Introduction</b> .....	<b>1</b>
1.1 Photonics integration .....	1
1.1.1 Silicon photonics.....	4
1.1.2 Silicon nitride photonics .....	6
1.1.3 Heterogeneous integration .....	6
1.1.4 Colloidal quantum dots .....	7
1.2 Definition of research objectives .....	11
1.3 Structure of thesis .....	12
1.4 Publications.....	13
References.....	16
<b>2 Colloidal quantum dots as novel light emitting material</b> .....	<b>21</b>
2.1 Colloidal quantum dots as gain material .....	21
2.1.1 Colloidal quantum dots optical gain .....	23
2.1.2 Single exciton gain.....	25
2.1.3 Biexciton gain .....	28
2.1.4 Biexciton lasing threshold analyze.....	32
2.2 Colloidal quantum dots as single photon emitter .....	36
References.....	40
<b>3 Silicon nitride platform optimization for colloidal quantum dots integration</b> .....	<b>45</b>
3.1 SiN deposition.....	47
3.2 SiN waveguide loss.....	49
3.2.1 Design and fabrication .....	49

---

3.2.2	Waveguide loss characterization.....	50
3.3	Waveguide loss with embedded monolayer QDS.....	52
3.3.1	Fabrication process .....	52
3.3.2	Waveguide loss characterization.....	54
3.3.3	Embedded QDs luminescence .....	55
3.4	SiN layer stress characterization .....	56
3.5	SiN fluorescence measurement.....	59
3.6	Conclusion .....	61
	References.....	62
<b>4</b>	<b>Colloidal quantum dots as gain material in SiN platform .....</b>	<b>67</b>
4.1	Colloidal QDs material gain characterization .....	68
4.2	Waveguide modal gain .....	74
4.2.1	Fabrication process .....	76
4.2.2	Waveguide modal gain measurement .....	79
4.3	DFB laser design, fabrication and characterization.....	84
4.3.1	Laser cavity design .....	85
4.3.2	Fabrication process .....	87
4.3.3	Laser characterization .....	88
4.3.3.1	Femtosecond laser pumping .....	88
4.3.3.2	Nanosecond laser pumping .....	92
4.3.4	Results analysis.....	94
4.4	Gain-coupled DFB laser design, fabrication and characterization ...	96
4.4.1	Fabrication process .....	98
4.4.2	Gain-coupled DFB laser characterization .....	101
4.4.3	Conclusion .....	102
4.5	Colloidal nano-platelets integration .....	103
4.5.1	Transient absorption spectroscopy for the NPLs .....	103
4.5.2	Waveguide modal gain measurement .....	106
4.5.3	Conclusion .....	108
4.6	Conclusion .....	109
	References.....	111
<b>5</b>	<b>Colloidal quantum dots as single photon source in SiN platform ....</b>	<b>117</b>
5.1	Ultra-compact SiN grating coupler for microscopy system .....	122
5.1.1	Grating coupler design.....	124
5.1.2	Fabrication process .....	129
5.1.3	Characterization .....	132
5.1.4	Conclusion and discussion .....	134
5.2	Waveguide with embedded monolayer QDs.....	135

---

5.2.1 Fabrication process .....	135
5.2.2 Characterization .....	138
5.2.3 Conclusion and discussion .....	140
5.3 Conclusion .....	141
References .....	142
<b>6 Conclusions and perspectives .....</b>	<b>146</b>
6.1 Conclusions.....	146
6.2 Perspectives .....	148



# List of Figures

<b>Figure 1.1:</b> A diagram of the electromagnetic spectrum, showing various properties across the range of frequencies and wavelengths.[2].....	2
<b>Figure 1.2:</b> The components of the 1st ruby laser by T.H. Maiman [4]. .....	2
<b>Figure 1.3:</b> The structure of the normal optical fiber [6].....	3
<b>Figure 1.4:</b> Silicon wafer with integrated photonics circuits. Left: 400 mm silicon wafer; right: diced small chips. ....	4
<b>Figure 1.5:</b> The energy wave vector comparison with direct bandgap semiconductor material and indirect bandgap semiconductor material. Adapted from ref [12].....	5
<b>Figure 1.6:</b> The left picture: SEM view of a silicon photonic wire waveguides fabricated with the process from [14]; the right picture: SEM view of a silicon micro ring resonator [15]. ....	5
<b>Figure 1.7:</b> Bonding active III-V chips to the top of silicon photonics circuits. Adapted from ref [12][23]......	7
<b>Figure 1.8:</b> When they are excited by ultraviolet light (pictured), colloidal quantum dots fluoresce at different colors depending on the particle size. ....	8
<b>Figure 1.9:</b> An idealized model of electronic states in a spherical QD made of the same material (right) and a bulk semiconductor (left). Continuous bands of a bulk semiconductor with a parabolic dispersion of carrier kinetic energies ( $E_k \propto k$ ; $k$ is the wave vector) in the valence and conduction bands (denoted VB and CB, respectively) has been transformed into discrete atomic-like levels in the case of the atomic-like colloidal QD. Adapted from ref [39]......	9
<b>Figure 1.10:</b> Emission wavelength and sizes of colloidal QDs of different composition. Colloidal QDs can be synthesized using different types of semiconductor materials (II-VI: CdS, CdSe, CdTe; III-V: InP, InAs; IV-VI: PbSe) with different bulk band gap energies. The curves in the figure represent experimental data from the literature on the dependence of peak emission wavelength on colloidal QDs diameter. The range of emission wavelength is 400 to 1350 nm, with size varying from 2 to 9.5 nm (organic passivation/solubilization layeris not included). All spectra typically have full width at half maximum around 30 to 50 nm. Inset: The emission spectra for different materials covering from 400 nm to 1350 nm. Adapted from ref [41]......	10

- Figure 2.1:** Left: a packaged laser diode shown with a USD penny for scale. Right: the laser diode is removed from the above package and placed on the eye of a needle for scale [4].....22
- Figure 2.2:** The energy-band structure of InP-based metamorphic type-I QW laser. The injection directions of electrons and holes are indicated. Adapted from [5].....22
- Figure 2.3:** Calculated maximum gain as a function of injection current density for the GaAs/Ga<sub>0.8</sub>Al<sub>0.2</sub>As quantum box (i.e., QD), quantum wire, quantum film (i.e., quantum well), and bulk crystal (conventional double heterostructure). Dashed lines mark the lasing threshold for each material. Adapted from ref [6] .....23
- Figure 2.4:** Scheme of Auger effects. (A) Auger relaxation effect of a biexciton into a neutral QD. The remaining excited carrier is in a higher state but still confined in the QD. (A') Auto-ionization effect of a neutral QD by Auger process. The remaining excited electron is excited out of the QD. (B) Auger relaxation effect of a biexciton in an ionized QD. Adapted from ref [17]. ....25
- Figure 2.5:** Scheme of simplified 2 fold model. (a) The transparency situation when there is no exciton–exciton interactions. The single exciton (electron–hole pair) in a QD results in optical transparency. (b) With the presence of exciton–exciton interactions, the second absorption event transition is displaced with an energy shift  $\Delta_{xx}$  from that whereby the original electron–hole pair. A stark shift is created by the first electron–hole pair. The balance between stimulated emission and absorption becomes broken; hence the lasing can occur with the help of this shift. Adapted from ref [24].....27
- Figure 2.6:** Simplified scheme for three different interaction regimes of a semiconductor colloidal QD with a photon resonant with the band-edge transition. It has a 2-fold spin-degenerate conduction-band (CB) and valence-band (VB) levels. Adapted from [24].....29
- Figure 2.7:** (a) The quasi-three-state model of optical gain in QDs, which comprises a nondegenerate ground state ( $|0\rangle$ , bottom), a four-fold degenerate single-exciton state, ( $|X\rangle$ , middle) and a nondegenerate biexciton state ( $|XX\rangle$ , top). (b) A quasi-three-level transition scheme with photon absorption (up arrows) and stimulated emission (down arrows). The rates of different transitions are indicated in the figure (per unit photon density);  $\gamma$  is the transition probability per single spin-allowed transition (shown by black arrows in panel a). Adapted from ref [32]. .....30
- Figure 2.8:** The plot of the CW lasing threshold  $J_{las}$  as a function of  $\tau_{xx}$ . The different colors indicate different cavity photon lifetime:  $\tau_c = 1$  ns (black squares), 0.1 ns (red circles), 0.01 ns (green triangles), 0.005 ns (blue diamonds), 0.002 ns (magenta pentagons), and 0.001 ns (brown hexagons). The pump wavelength is 400 nm. Adapted from ref [32]. .....34
- Figure 2.9:** Hanbury Brown-Twiss interferometer set-up. (a) The schematic of the setup. (b) The correlation amplitude measurement results of a single photon source by using the Hanbury Brown-Twiss interferometer set-up. The blue

- curve is the result of CW excitation; the red curve is the result of pulsed excitation. Adapted from ref [47].....38
- Figure 3.10:** Measured distribution  $n(\tau)$  of photon pair separation times  $\tau$  for a CdSe/ZnS cluster and a single quantum dot. The line represents a fit to an exponential law. Adapted from ref [50]. .....39
- Figure 3.1:** (a) The ellipsometry measurement results for refractive indices  $n$  of SiN films deposited using different conditions. H-F, L-F and M-F stand for high frequency, low frequency and mixed frequency RF bias. H-SiN stands for high temperature (270 °C) chamber; L-SiN stands for low temperature (120 °C) chamber. (b) The extinction coefficients  $k$  of SiN deposited under different conditions. ....48
- Figure 3.2:** The lithography process flow for SiN waveguide loss measurement. (a) Prepare substrate, (b) apply resist, (c) exposure, (d) after development. Adapted from ref [31].....49
- Figure 3.3:** Picture of the horizontal alignment fiber setup. Left picture is the overview of the whole setup. Right picture is the waveguide chip with already well aligned lensed fibers. The insets are zoomed pictures with microscope. ....50
- Figure 3.4:** The measured waveguide losses of H-SiN (270 °C) and L-SiN (120 °C) SiN layers deposited with low RF frequency bias. The thickness of all SiN waveguides is ~200 nm and the waveguide width are varied from 0.8  $\mu\text{m}$  to 2.0  $\mu\text{m}$ . The inset picture shows the linear fits for H-SiN waveguide and L-SiN with 2.0  $\mu\text{m}$  width . The result has been normalized to the reference waveguides. Waveguide support multimode for width larger than 1  $\mu\text{m}$ . Adapted from ref [31].....51
- Figure 3.5:** (a) Schematics of SiN waveguide with embedded monolayer colloidal QDs fabrication flow. (b) SEM image of the LB deposited monolayer colloidal QDs. The inset shows the zoom in details of the close-packed LB colloidal QDs film. (c) PL of a 2x2 cm LB colloidal QDs film illuminated with a UV lamp. Adapted from ref [31]. .....54
- Figure 3.6:** Waveguide losses with different widths of H-SiN/L-SiN and H-SiN/QD/L-SiN stacked layers. The inset shows the detailed linear fitting of the normalized transmissions of 2  $\mu\text{m}$  wide waveguides. Adapted from ref [31].....55
- Figure 3.7:** The collected PL spectra from hybrid SiN waveguides with colloidal QDs on top/embedded. A red shift and an increased intensity can be observed at the longer wavelength, which can be explained by the wavelength-dependent reabsorption and probably also the change of emission profile from the defects. Adapted from ref [31] .....56
- Figure 3.8:** Types of applied stress. (a) Tensile stress; (b) Compressive stress; (c) Shear stress. Adapted from ref [35].....57
- Figure 3.9:** General principle of the stress measurement Adapted from ref [37]. .....58
- Figure 3.10:** Photon counting system for material fluorescence measurement. Adapted from [38].....60
- Figure 3.11:** Photoluminescence measurements from different SiN layers.....61

- Figure 4.1:** The TEM picture of flash CdSe/CdS colloidal QDs, the inset is the solution luminescence under UV lamp. Adapted from ref [10]. .....69
- Figure 4.2:** Absorption (expressed as intrinsic absorption coefficient ( $\mu_i$ ) and emission (red) spectrum after excitation at 400 nm. The QDs have a luminescence quantum yield of 80%. Inset: photoluminescence (PL) decay showing an average decay time of 58.5 ns, a single exciton lifetime of 26.8 ns. ....70
- Figure 4.3:** Transient Absorption Spectroscopy (TAS) system. (a) The principle of the TAS system. Pump-probe method is used to determine the absorption change of the sample. (b) The schematic of the TAS system. (c) The picture of the TAS system. ....71
- Figure 4.4:** The time dependent dynamics of A at a fixed probe wavelength of 630 nm after 520 nm excitation. We can see the optical gain builds up very fast ( $< 2$  ps) and can last up to 270 ps. Importantly, from the TA traces, we estimate that the process that causes the decay of the non-linear absorbance at the lowest fluences used has a rate constant of  $\sim 2 \text{ ns}^{-1}$  (500 ps bi-exciton lifetime). ....73
- Figure 4.5:** Material gain at 2.5 ps with 520 nm pumping at different pumping intensity, the total bandwidth can be as large as 130 nm reaching ca.  $1200 \text{ cm}^{-1}$  at 615 nm. ....74
- Figure 4.6:** Sketch of the variable stripe length configuration. The amplified spontaneous emission intensity  $I_{ASE}(z)$  is collected from the edge of the sample as a function of the excitation length  $z$ . The optical pumping beam is usually focused on a thin stripe with a cylindrical lens. Adapted from ref [15]. ....75
- Figure 4.7:** The fabrication flow of waveguide with variable stripe length. (a)  $\sim 100$  nm thick L-F H-SiN is deposited on top of silicon wafer with  $3 \mu\text{m}$  thermal oxide. Then the *flash* CdSe/CdS core/shell colloidal QDs are spin coated on top of this SiN. (b)  $\sim 100$  nm thick M-F H-SiN is deposited onto the colloidal QDs layer. (c) Lithography is used to define the waveguides with variable stripe length. (d) Reactive ion etching (RIE) is used to define the waveguides. Note the sample is cleaved before etching. Oxygen plasma cleaning is followed to remove the residual resist. ....76
- Figure 4.8:** Optical microscope images of the surface morphologies of SiN/QD/SiN layer stack after deposition of top SiN at different PECVD frequency mode. (a) Low-frequency and (b) mixed-frequency modes. The scale bar is  $50 \mu\text{m}$ . ....77
- Figure 4.9:** SEM picture of the fabricated sample. (a) The titled SEM picture showing the top SiN layer and waveguide side wall. (b) The cross section of waveguide. ....78
- Figure 4.10:** Microscope image of the fabricated sample. The adjacent waveguide has a length difference  $10 \mu\text{m}$ . Uniform facets can be seen from the picture. ....79
- Figure 4.11:** Measurement setup. The pumping laser beam is tuned using a neutral density (ND) filter. A 50/50 beam splitter is used to split the beam and one beam is sent to a detector to monitor the beam fluence. A cylindrical lens is used to focus the beam into a rectangular shape to pump the waveguide.

- The emission from the waveguide is collected by a multimode fiber (NA=0.2) and send to detector to record the intensity or spectrometer to record the spectrum.....80
- Figure 4.12:** The power distribution of the pumping beam after the cylindrical lens focusing. (a)The focused beam shape record by the CCD from the beam profile. (b) The field distribution from X-axis. (c) The field distribution from Y-axis. ....81
- Figure 4.13:** Power dependence measurement. The measurement is performed with a 4  $\mu\text{m}$  wide, 600  $\mu\text{m}$  long waveguide. The ASE onset pumping fluence is around 12  $\text{uJ}/\text{cm}^2$ . The black, blue and red line indicate the pumping fluence we will use for the later gain coefficient measurement, which are 56  $\text{uJ}/\text{cm}^2$ , 34  $\text{uJ}/\text{cm}^2$  and 30  $\text{uJ}/\text{cm}^2$  respectively.....82
- Figure 4.14:** Emission spectrum of a 4  $\mu\text{m}$  wide 600  $\mu\text{m}$  long waveguide with pumping fluence 54  $\mu\text{J}/\text{cm}^2$  @ 400 nm. ....83
- Figure 4.15:** Measured output power versus the waveguide length with 3 different pumping fluences. The inset is the mode profile of the fundamental TE mode of the waveguide structure.....84
- Figure 4.16:** The simulated stop band of the grating has been shown in the picture as the region between the gray and red areas. The ASE spectrum has been inserted as a comparison for the grating periods choosing. ....85
- Figure 4.17:** DFB optical cavity design. (a) The reflection spectrum with different number of periods. The grating period is 188 nm and the etching depth is 35 nm. The stopband is around 13.7 nm with 100 periods of grating. (b) The reflection spectrum with different etching depth. The period is 188 nm and the number of period is 100. With the increased etching depth, grating are becoming stronger, with higher reflection and wider stopband. ....86
- Figure 4.18:** Fabrication overview. (a) First, a L-F H-SiN layer is deposited on a silicon substrate with a 3  $\mu\text{m}$  thermal silicon oxide grown on top. Next, the QD layer is spin coated on top and another M-F H-SiN layer is deposited on the QD layer to encapsulate the QDs and form the hybrid SiN/QD/SiN stack. (b) Electron beam lithography to pattern the grating. (c) RIE etching to transfer the grating patterning to the top-SiN layer. (d) Contact lithography and RIE etching to pattern the waveguide.....87
- Figure 4.19:** SEM graph of fabricated samples. (a) Tilted SEM picture near the phase shifter region. We could see well patterned grating on top of the waveguide. (b) FIB cross section picture taken in the phase shifter region. The grating period is 188 nm and the etching depth is around 35 nm as designed. ....88
- Figure 4.20:** (a) Light (in)-light (out) measurement on double linear scale for DFB laser with 188nm period. The pump laser is the same femtosecond laser used in the gain measurement. (b) The evolution of the spectral width (FWHM) under the different pump intensity. The inset is the spectra under different pump fluence. Note that the noise level is around 600 .....89
- Figure 4.21:** (a) Spectra measured from an unpatterned waveguide (black) and DFB lasers with different grating periods (colored).(b) Spectra measured

	from laser with 188 nm period at different pumping fluence. The inset is the log-scale measured spectra under different pump fluence .....	90
<b>Figure 4.22:</b>	Captured microscope pictures of the laser under/above threshold. (a) Under lasing threshold. (b) Above lasing threshold.. .....	91
<b>Figure 4.23:</b>	Multimode lasing with multi peaks in the spectrum. The laser's waveguide width is 4 $\mu\text{m}$ width with a 400- $\mu\text{m}$ cavity length. The grating period is 188 nm.....	92
<b>Figure 4.24:</b>	Beam calibration for the nanosecond laser along x-axis (a) and y-axis (b). The fitted results shows the $\omega_x$ is 1115 $\mu\text{m}$ and $\omega_y$ is 26 $\mu\text{m}$ .....	92
<b>Figure 4.25:</b>	(a)The light(in)-light(out) curve on a double linear scale, with indication of the lasing threshold around 270 $\mu\text{J}/\text{cm}^2$ , which has an equivalent CW power density of 39 $\text{kW}/\text{cm}^2$ . (b) The light(in)-light(out) curve on a double log-scale with rate equation fit (black solid). A spontaneous emission factor ( $\beta$ ) 0.009 is extracted. ....	93
<b>Figure 4.26:</b>	Below threshold spontaneous emission spectrum from DFB-laser before (black) and after (red) normalizing with spectrum of unpatterned waveguide. ....	94
<b>Figure 4.27:</b>	Effect of biexciton lifetime on lasing threshold. The CW lasing threshold is plotted as a function of biexciton lifetime $\tau_{xx}$ . Different cavity lifetimes are plotted with different color: $\tau_c=0.1$ ns (black); $\tau_c=0.01$ ns (red); $\tau_c=0.002$ ns (green); $\tau_c=0.001$ ns (blue). ....	95
<b>Figure 4.28:</b>	Schematic drawing of the longitudinal cross section of the gain-coupled DFB laser structure. Adapted from ref [35]. ....	98
<b>Figure 4.29:</b>	Fabrication overview. (a) First, an L-F H-SiN layer is deposited on a silicon substrate with a 3 $\mu\text{m}$ thermal silicon oxide grown on top. (b) Ebeam is used to pattern the grating for the lift off process. (c) Colloidal QDs layer are spin-coated on top of the sample followed by a lift off process. Periodical structures of the gain section are formed. (d) Contact lithography and RIE etching to pattern the waveguide. The gain sections are buried in the waveguide periodically to form the gain-coupled DFB laser. ....	99
<b>Figure 4.30:</b>	SEM quality checking for the colloidal QDs layer lift off. (a) The overall of the patterned grating. (b) The detail check of the patterned grating. A 200 nm period is achieved as designed with no residual colloidal QDs in the grating trench region. ....	100
<b>Figure 4.31:</b>	SEM picture of the fabricated gain-coupled DFB laser. (a) The tilted sidewall of the fabricated sample. (b) The cross section picture of the fabricated sample.....	100
<b>Figure 4.32:</b>	(a)The light(in)-light(out) curve on a double linear scale, with indication of the lasing threshold around 950 $\mu\text{J}/\text{cm}^2$ , which has an equivalent CW power density of 135.7 $\text{kW}/\text{cm}^2$ . (b) The light (in)-light (out) curve on a double log-scale with rate equation fit (black solid). A spontaneous emission factor ( $\beta$ ) 0.007 is extracted. ....	102
<b>Figure 4.33:</b>	Emission spectra of three devices with varying grating period (pumping fluence = 1100 $\mu\text{J}/\text{cm}^2$ @ 532 nm).pectra measured from DFB lasers with different grating periods. ....	102

- Figure 4.34:** (a) Transmission Electron Microscope (TEM) image of 4 monolayer thick CdSe nano-platelets with an average lateral area of 34 by 9.6 nm<sup>2</sup>. (b) Photoluminescence (blue) linear absorption spectrum (black) of CdSe NPLs dispersed in hexane, normalized to represent the intrinsic absorption coefficient.....104
- Figure 4.35:** Overview of pump-probe and luminescence spectroscopy under low-excitation conditions. (a) 2D time-wavelength map of the negative part of the absorbance  $A(\lambda,t)$ , for photo-excitation at 400 nm with 45  $\mu\text{J}/\text{cm}^2$ , creating  $\langle N \rangle = 10$  electron hole-pairs at time zero. The gain is red shifted from the HH exciton peak at 510 nm and initially extends from 528 nm to 570 nm, only to narrow down and vanish after *ca.* 100 ps. Note that the gain spectrum extends up to 250 meV redshifted from the HH exciton line. (b) Photoluminescence as function of wavelength and time for similar excitation conditions as (a). A clear asymmetric broadening towards longer wavelengths is observed at early times, vanishing on a timescale similar to the net gain in (a). (c) At 2.5 ps, we take horizontal cuts from data sets as shown in (a) and normalize them appropriately to represent the intrinsic absorption coefficient  $\mu_i$  for increasing pump fluence expressed as  $\langle N \rangle$ . The shaded region indicates the gain band where intrinsic gain up to 1000  $\text{cm}^{-1}$  is achieved for densities of 10 electron hole pairs per platelet. Bottom spectra show the photoluminescence spectra at 2.5 ps showing an increased contribution from a red-shifted (lower energy) component. Note that the gain spectrum  $\mu_i < 0$  overlaps perfectly with the region of increased PL bandwidth. (d) Threshold density of electron hole pairs for net optical gain to occur at a given wavelength. The minimum density is 5.3 ( $\pm 0.3$ ) and remarkably no gain is achieved at the position of the HH exciton line itself.105
- Figure 4.36:** The microscopy picture comparison. (a) SiN stack sample with embedded *flash* dots. (b) SiN stack sample with embedded NPLs.....106
- Figure 4.37:** SEM picture of the fabricated sample. (a) The titled SEM picture showing the top SiN layer and waveguide side wall. (b) The cross section of waveguide. ....107
- Figure 4.38:** (a) Emission spectrum of a 4  $\mu\text{m}$  wide 100  $\mu\text{m}$  long waveguide with pumping fluence 440  $\mu\text{J}/\text{cm}^2$  @ 400 nm. (b) Measured output power versus the waveguide length with pumping fluence 440  $\mu\text{J}/\text{cm}^2$  @ 400 nm.....108
- Figure 5.1:** SEM picture of lift off results with LB colloidal QDs layer deposition, using  $\sim 33$  nm thickness resist with pattern holes  $\sim 31.6$  nm in diameter. The 5 by 5 grid image has the same scale bar of 50 nm. The scale bar has been put at the right bottom corner. Adapted from ref [20].....119
- Figure 5.2:** The coupling factor and polarization ratio for a suspended SiN waveguide with a dipole-like emitter in the middle of the waveguide. (a) Total coupling factor  $\beta$  to the guided modes as a function of the waveguide width  $W$  for two different waveguide heights  $H = 100$  nm (red) and 220 nm (blue). (b) Polarization dependent coupling factors  $\beta_y$  (dashed line) and  $\beta_z$  (plain line) as a function of the waveguide width  $W$  for two different waveguide heights  $H = 100$  nm (red) and 220 nm (blue). Adapted from ref [21].....120

- Figure 5.3:** The coupling factor and polarization ratio of a suspended SiN slot-waveguide with a dipole-like emitter in the middle of the waveguide.. (a) Total coupling factor  $\beta$  to the guided modes as a function of the waveguide width  $W$  for two different waveguide heights  $H = 300$  nm (red) and  $500$  nm (blue). (b) Polarization dependent coupling factors  $\beta_y$  (dashed line) and  $\beta_z$  (plain line) as a function of the waveguide width  $W$  for two different waveguide heights  $H = 300$  nm (red) and  $500$  nm (blue). Adapted from ref [21]. ..... 121
- Figure 5.4:** Anti-bunching established with both continuous and pulse excitation proving that the *flash* CdSe/CdS core/shell QD is a good single photon emitter. .... 122
- Figure 5.5:** (a) The schematic of the grating coupler design; (b) The top view of the proposed circular shape grating coupler, a small supporting beam is added between the grating coupler and the waveguide to ensure a fully suspended structure realistic. .... 125
- Figure 5.6:** (a) 3D FDTD simulation results of period length vs power up/power collected with  $NA = 0.65$ ; (b) 3D FDTD simulation results of number of periods vs power up/power collected  $NA = 0.65$  (the period length is  $600$  nm). .... 125
- Figure 5.7:** the power coupled upwards as function of the filling factor with 3 periods grating with  $600$  nm period length. .... 126
- Figure 5.8:** The reflectance with different metal layer thickness at  $632.8$  nm. Al layer and Au layer is compared. .... 127
- Figure 5.9:** (a) 3D FDTD simulation results of total power radiated upwards and power collection with  $NA = 0.65$  versus distance  $D_{\text{clad}}$ . Results for substrates with/without Al coating are shown. (b) 3D FDTD simulation of far field radiation pattern of the grating coupler with optimized parameters ( $600$  nm period length;  $950$  nm  $D_{\text{clad}}$  distance). (c) Simulation results of coupling efficiency with different NA. (d) Simulation results of bandwidth and collecting efficiency comparison of different grating couplers. .... 128
- Figure 5.10:** Proposed device structure to measure the efficiency of the ultra-compact grating coupler. The structure contains suspended waveguide with grating couplers at both sides. .... 129
- Figure 5.11:** Schematics of the fabrication flow. (a) Deposition of  $50$  nm Aluminium layer on top of the silicon substrate. Thin layer of Aluminium oxide ( $5$  nm) and silicon oxide ( $5$  nm) are later deposited on the Al layer to protect the Al layer from oxidation and wet etching. (b)  $950$  nm of a-Si is deposited on top of Al layer. (c)  $220$  nm of SiN is deposited on top of a-Si layer as the waveguide layer. (d) E-beam is used to pattern the test structure and RIE etching transfers the pattern from e-beam resist to SiN layer. (e) Wet etching is used to undercut the grating and the waveguide. Some a-Si is left to support the pillar, as shown in the figure. (f) CPD process is used to release the structure and oxygen plasma cleaning is used to remove the residual e-beam resist. .... 130

- Figure 5.12:** SEM picture of the structures after release with L-F H-SiN layer. From the picture. The compressive stress introduced by the SiN layer leads to a failure released structure.....131
- Figure 5.13:** SEM picture of fabricated device array with H-F SiN layers. The tensile stress introduced by the SiN layer guarantees a successful release after wet etching. ....131
- Figure 5.14:** Microscopy system setup for the measurement. The laser is focused by a lens with NA = 0.65. There is an iris to block the reflection from the input laser in the image plane. The light from the out coupling grating can be measured with the detector. Insert: optical microscope picture of the grating couplers with input reflection and output spot (without the iris).....132
- Figure 5.15:** 1.5  $\mu\text{m}$  waist radius Gaussian laser beam coupling in efficiency with changed grating period. ....133
- Figure 5.16:** Measurement results: the black curve is the simulated power couple to a microscopy system with NA=0.65; the blue curve is the measured results with a 950 nm distance between the grating coupler and the Al substrate. .134
- Figure 5.17:** Proposed device structure to embed monolayer QDs into waveguide. Optimized grating couplers are at both sides. The QDs section will be pumped by a blue laser and emission will be coupled into waveguide mode and couple out by the grating coupler at both sides.....133
- Figure 5.18:** Schematics of the fabrication flow. (a) Deposition of 110 nm H-F H-SiN layer on top of the silicon substrate. (b) Au marker patterning has been done with e-beam and lift off process (c) First overlay e-beam and L-B process is used to pattern the monolayer colloidal QDs layer (d) 110 nm H-F L-SiN is deposited to encapsulate the colloidal QDs layer (e) Second overlay e-beam is use to pattern the grating (f) Alkaline based TMAH wet etching is used to remove the silicon under the waveguide and make the structure free hanging. CPD process is used to release the structure and oxygen plasma cleaning is used to remove the residual e-beam resist. ....136
- Figure 5.19:** SEM image of the fabricated sample. (a) The monolayer QDs layer deposited on top of the SiN layer by overlay e-beam, L-B process and lift off process. The strip QDs layer has a width about 50 nm. (b) The fabricated sample after the CPD release. The whole device is well free hanging. The embedded QDs are in the middle of the free hanging waveguide. ....137
- Figure 5.20:**The schematic of the micro-photoluminescence setup diagram .....138
- Figure 5.21:** The captured image with the EMCCD camera. A top view SEM image of the device structure is also shown on the right as a compare. The scale bar is 10  $\mu\text{m}$ .....139
- Figure 5.22:** The spectra of the emission from the pumping spot and the grating couplers using the imaging spectrometer. ....140



# List of Tables

<b>Table 3.1:</b> The detailed recipe for gas ratio, RF bias frequency and power for Advanced Vacuum Vision 310 PECVD SiN deposition. The mixed frequency receipt used a mixed high frequency bias and low frequency bias with a 6:1.5 time ratio.....	47
<b>Table 3.2:</b> Stress type and average stress of different type of SiN layer. ....	58
<b>Table 5.1:</b> Reflectance at 632.8 nm of commonly used metals. ....	127



# List of Acronyms

## A

ASE Amplified Spontaneous Emission

## C

CMOS Complementary Metal-Oxide-Semiconductor

CMP Chemical Mechanical Planarization

CPD Critical Point Drying

CW Continuous-Wave

## D

DFB Distributed Feedback

## E

EM Electromagnetic

EBL Electron-Beam Lithography

FWHM Full-Width at Half-Maximum

## F

FDTD Finite-Difference Time-Domain

FIB Focused Ion Beam

## L

LPCVD Low-Pressure Chemical Vapor Deposition

LB Langmuir-Blodgett

## N

NA	Numerical Aperture
NPL	Nanoplatelet
<b>P</b>	
PICs	Photonic Integrated Circuits
PR	Photoresist
PECVD	Plasma-Enhanced Chemical Vapor Deposition
PL	Photoluminescence
<b>Q</b>	
QDs	Quantum Dots
<b>R</b>	
RIE	Reactive-Ion Etching
<b>S</b>	
SiN	Silicon Nitride
SOI	Silicon on Insulator
SEM	Scanning Electron Microscope
<b>T</b>	
TE	Transverse electric
TEM	Transmission electron microscopy
TAS	Transient Absorption Spectroscopy
<b>U</b>	
UV	Ultraviolet
<b>V</b>	
VSL	Variable Strip Length
<b>W</b>	
WGMs	Whispering Gallery Modes

# Nederlandse samenvatting

## –Summary in Dutch–

Colloïdale quantum dots, een nieuwe klasse van materialen, hebben veel veelbelovende eigenschappen. Door het kwantum opsluitingseffect is een groot bereik van emissiegolflengten toegankelijk met slechts één enkel materiaal. Met behulp van een enkele chemische synthesesetechniek waarbij slechts één parameter wordt aangepast, de QD-grootte, zijn ze een zeer veelzijdig en goedkoop emissiemateriaal. Een breed absorptiespectrum in combinatie met een smalle fotoluminescentie, instelbaar van het zichtbare tot het infrarood met een hoge fotoluminescentiekwantumopbrengst, maakt ze zeer aantrekkelijk voor toepassingen in de opto-elektronica. Bovendien plaatsen de lage kosten van de QD-synthese en depositiewerkwijzen, meestal door niet-vacuümtechnieken zoals spincoating of Langmuir-Blodgett-depositie, ze al op de voorgrond van uiteenlopende toepassingen zoals displays en verlichting. Dezelfde pluspunten van instelbare optische eigenschappen en eenvoudige verwerking maakt colloïdale QDs het meest aantrekkelijk voor hybride geïntegreerde fotonica, waar ze kunnen worden gebruikt als bouwstenen voor coherente lichtbronnen zoals lasers, incoherente breedband-LED's of zelfs 'single' foton bronnen.

Siliciumnitride is een veelbelovend dielektrisch materiaal met een grote verboden zone (5 eV) dat compatibel kan zijn met hetzelfde CMOS-raamwerk als silicium. Het heeft niet alleen een relatief groot indexcontrast in vergelijking met siliciumoxide en polymeer, maar heeft ook een zeer breed transparant venster, dat zich uitstrekt van 0,4  $\mu\text{m}$  tot ongeveer 4  $\mu\text{m}$ . Het nieuwe golflengtebereik van 0,4  $\mu\text{m}$  tot 1,1  $\mu\text{m}$ , waar silicium absorbeert, opent nieuwe toepassingen voor bio-detectie en Raman-spectroscopie op chip. De voordelige eigenschappen van SiN zijn aangetoond door talrijke groepen aangetoond, maar de meeste resultaten bleven beperkt tot puur passieve functionaliteiten zonder actieve functies, met in het bijzonder lichtemissie, die nog grotendeels ontbrak voor het SiN-platform. Dit laatste is essentieel voor het bouwen van volledig on-

chip geïntegreerde systemen. Siliciumnitride is echter, net als silicium, geen ideaal materiaal om licht te genereren.

In dit proefschrift hebben we een heterogeen integratieplatform ontwikkeld dat de uitstekende optische emissie-eigenschappen van colloïdale QDs combineert met het SiN-golfgeleiderplatform. Ten eerste is een passief SiN-fotonisch-golfgeleiderplatform ontwikkeld en gedemonstreerd op basis van een door plasma versterkt chemisch dampdepositieproces. Met het geoptimaliseerde depositie- en etsrecept hebben we golflengten met weinig verlies bereikt, met  $\sim 1$  dB / cm optisch verliezen voor golflengten rond 900 nm. Bovendien kunnen de colloïdale QDs ingebed worden tussen twee SiN-lagen zonder de fotoluminescentie-eigenschappen te verliezen. Met het geoptimaliseerde depositie- en etsrecept, vertoont een SiN-golfgeleider, die een laag colloïdale QDs bevat, nog steeds golfgeleiderverliezen van  $\sim 2$ -3 dB / cm, laag genoeg voor de meeste golfgeleidercircuits. We hebben ook in detail de stress- en materiaalfluorescentie van SiN-lagen die met verschillende recepten zijn afgezet gekarakteriseerd, waardoor ze kunnen worden geoptimaliseerd voor verschillende toepassingen.

Het ontwikkelde hybride SiN/colloïdale QDs-platform combineert colloïdale QDs met het SiN-golfgeleiderplatform waarbij de ingebedde QDs nog steeds licht kunnen uitzenden. Dit is een grote stap in de richting van ons doel om on-chip lichtgeneratie te demonstreren. Wanneer deze ingebedde QDs worden gepompt met femtoseconde gepulste laserpulsen, tonen ze versterkte spontane emissie (ASE), die op efficiënte wijze in een golfgeleider kan gekoppeld worden. We hebben de traditionele VSL-methode (variabele strooklengte) aangepast in een op golfgeleider gebaseerde VSL-meting, wat helpt om de inherente problemen zoals licht spreiden in de laag, positieafhankelijkheid van de uitkoppeling, enz. van de standaard VSL-methode te elimineren. Op basis van deze verbeterde op golfgeleider gebaseerde VSL-meting, kunnen we de modale winst van golfgeleiders met ingebedde colloïdale QDs extraheren. Omdat de geometrie van de golfgeleider ons ook in staat stelt om de mode-opsluiting te berekenen, samen met de gekende volumefractie van de colloïdale QDs, kunnen we daaruit ook de intrinsieke materiaalversterking berekenen van de ingebedde compacte colloïdale QD-laag. De resultaten komen overeen met de resultaten die we behaalden met Transit Absorptie Spectroscopie (TAS). Gebruikmakend van deze optische winst, hebben we gedistribueerde feedbacklasers op het hybride SiN colloïdale QDs-platform ontworpen, gefabriceerde en gekarakteriseerd. De laser toont laserwerking in één mode onder femtoseconde gepulste pumping met een laserdrempel rond  $12 \mu\text{J} / \text{cm}^2$  bij 400 nm. Om de laserprestaties verder te onderzoeken, gebruikten we een Q-switched frequentie verdubbelde Nd: YAG laser (532 nm) met een 7 nanoseconden pulsbreedte en een 938 Hz herhalingsnelheid. De laser vertoont nog steeds laserwerking met een laserdrempel van ongeveer  $270 \mu\text{J} / \text{cm}^2$ . Voor

de flash CdSe / CdS kern / schil colloïdale QDs die we voor onze laser hebben gebruikt, laten de metingen die worden gerapporteerd in sectie 4.1 zien dat deze deeltjes een 2 ns-1 biexciton-verval vertonen, wat overeenkomt met een levensduur van 500 ps. In vergelijking met deze biexciton-levensduur kan onze 7 ns-pomp feitelijk worden beschouwd als quasi-CW-pompen, met een equivalente laserdrempel rond 39 kW / cm<sup>2</sup>. Dit opent perspectieven in termen van CW-werking en, bijgevolg, een uitgebreid toepassingspotentieel. De intrinsieke combinatie met het mature SiN-golfgeleiderplatform opent dan onmiddellijk het pad naar meer complexe apparaten zoals afstembare lasers en arrays van lasers met een enkele mode of integratie met passieve structuren zoals on-chip spectrometers.

Interessant is dat deze colloïdale QDs die tegen een lage kostprijs in dispersie kunnen worden gemaakt, direct op een substraat kunnen worden gedeponereerd in patronen. We hebben deze eigenschap gebruikt om versterkingsgekoppelde DFB-lasers te demonstreren op basis van een geoptimaliseerde colloïdale patroon-depositie techniek. De laser toont laserwerking in één mode zonder fase verschuiver in het midden van de lasercaviteit. De drempel ligt rond 950 μJ / cm<sup>2</sup> bij 532 nm onder gepulste optisch pomp. We hebben ook geprobeerd colloïdale nanoplaatjes (NPL's) te combineren met het SiN-golfgeleiderplatform. De NPL's tonen nog steeds hun ASE nadat ze in de SiN-laagstapels zijn ingesloten. Een materiaalversterkingscoëfficiënt rond 3500 cm<sup>-1</sup> kan uit de VSL-meting worden geëxtraheerd. Dit toont de veelzijdigheid van het ontwerp van hybride geïntegreerde fotonica-platformen. Ons geoptimaliseerde hybride SiN-golfgeleiderplatform kan mogelijk ook worden gebruikt voor de integratie van nog andere colloïdale nano-kristallen.

Colloïdale QD's zijn uitstekende kandidaten voor het realiseren van 'single' fotonemitters die werken bij kamertemperatuur. Ons ontwikkeld SiN-golfgeleiderplatform kan ook worden gebruikt om colloïdale QDs te integreren om on-chip 'single' fotonenbronnen te realiseren. Om deze op QD gebaseerde geïntegreerde 'single' fotonbronnen en de bijbehorende fotonische circuits te karakteriseren, zijn echter compacte, efficiënte en breedbandige koppelaars nodig die licht van een chip naar een objectief kunnen koppelen. In dit proefschrift hebben we het ontwerp, de fabricage en karakterisatie van een ultracompacte SiN-roosterkoppelaar aangetoond. De roosterkoppelaar is ontworpen om de koppeling tussen een gesuspendeerde SiN-golfgeleider en een microscopisch systeem te maximaliseren. Met de geoptimaliseerde parameters en slechts 3 perioden, hebben we experimenteel een koppelingsrendement van 53% aangetoond voor de fundamentele TE-mode (@ 632,8 nm) naar een microscopisch systeem met 0,65 NA. Een 116 nm 1dB bandbreedte kan theoretisch worden bereikt, vanwege het hoge contrast van het rooster en de grote verzamelhoek van het microscopisch systeem. We hebben geprobeerd om

nano-vlakjes van monolaag colloïdale QDs in de zwevende golfgeleider in te bedden. Met optisch pompen kan de emissie van de ingebedde QDs goed worden gekoppeld aan de optische modes van de golfgeleider. Met behulp van de roosterkoppelaar kunnen deze emissies ook worden gekoppeld aan het objectief.

In conclusie, dit proefschrift toont een succesvol ontwikkeld platform voor hybride integratie-fotonica, dat de uitstekende optische emissie-eigenschappen van colloïdale QDs combineert met het SiN-golfgeleiderplatform. Op basis van dit platform hebben we hybride laserbronnen met lage drempels gedemonstreerd. Er is ook gewerkt aan de realisatie van on-chip ‘single’-foton bronnen met dit platform. De resultaten tonen het potentieel om geïntegreerde ‘single’ fotonbronnen en de bijbehorende fotonische circuits met dit platform te bouwen.

# English summary

Colloidal quantum dots, a new class of materials, have lots of promising properties. Through the quantum confinement effect, a large range of emission wavelengths is accessible from just a single material. Using a single chemical synthesis technique with only one parameter to adjust, the QDs size, they are a highly versatile and low cost emission materials. A broad absorption spectrum combined with narrow photoluminescence, tunable from the visible to the infrared with a high photoluminescence quantum yield makes them very appealing for applications in opto-electronics. Additionally, the low cost of the QD synthesis and deposition methods, typically through non-vacuum techniques such as spin coating or Langmuir-Blodgett deposition, already puts them at the forefront of diverse applications such as displays and lighting. The same asset of tunable optical properties and easy processing makes colloidal QDs most appealing for hybrid integrated photonics, where they could be used as building blocks for coherent light sources like lasers, incoherent broadband LEDs or even single photon sources.

Silicon nitride is a promising dielectric material with a large band gap (5 eV) that can be compatible with the same CMOS framework as silicon. It not only has a relatively large index contrast compared with silicon oxide and polymer but also has a very wide transparency window, spanning from 0.4  $\mu\text{m}$  to around 4  $\mu\text{m}$ . The new wavelength range from 0.4  $\mu\text{m}$  to 1.1  $\mu\text{m}$ , where silicon is absorbing opens new applications for on-chip bio sensing and Raman spectroscopy. The advantageous properties of SiN have been demonstrated by numerous groups, yet most results remained limited to purely passive functionality without active functionality and in particular light emission is still largely missing for the SiN-platform. The latter is essential for building fully on-chip integrated systems. However, like silicon, silicon nitride is not an ideal material to generate light.

In this thesis, we have developed a heterogeneous integration platform which combines the excellent optical emission property of colloidal QDs with the SiN waveguide platform. First, a passive SiN photonics waveguide platform based on a plasma enhanced chemical vapor deposition process has been developed

and demonstrated. With the optimized deposition and etching recipe, we have achieved low-loss waveguides with  $\sim 1$  dB/cm optical loss for wavelengths around 900 nm. Moreover, the colloidal QDs can be embedded in between two SiN layers without quenching the photoluminescence properties. With the optimized deposition and etching recipe, a SiN waveguide containing a layer of colloidal QDs in between still exhibits waveguide losses as low as  $\sim 2$ -3 dB/cm, low enough for most waveguide circuits applications. We have also characterized in detail the stress and material fluorescence of SiN layers deposited with different recipes, allowing to optimize them to different applications.

The developed hybrid SiN colloidal QDs platform combines colloidal QDs with the SiN waveguide platform. The embedded QDs still emit light, a big step towards our goal of demonstrating on-chip light generation. Under femtosecond pulsed laser pumping, the embedded QDs show amplified spontaneous emission (ASE), which can be efficiently coupled to the waveguide. We have adapted the traditional variable stripe length (VSL) method into a waveguide based VSL measurement, which helps to eliminate the inherent problems of the standard VSL method, such as light spreading in the layer, position dependence of the out coupling etc. By using this improved waveguide based VSL measurement, we could extract the modal gain of waveguides containing embedded colloidal QDs. Since the waveguide geometry allows us to also calculate the mode confinement, with the known volume fraction from the colloidal QDs, we could also calculate the intrinsic material gain of the embedded compact colloidal QDs layer. The results are consistent with the results we got from Transient Absorption Spectroscopy (TAS).

Exploiting this optical gain, we have designed, fabricated and characterized distributed feedback lasers based on the hybrid SiN colloidal QDs platform. The laser shows single mode lasing under femtosecond pulsed laser pumping with a lasing threshold around  $12 \mu\text{J}/\text{cm}^2$  @ 400 nm. To further investigate the laser performance, we used a Q-switched frequency doubled Nd:YAG laser (532 nm) with a 7 nanosecond pulse width and a 938 Hz repetition rate for pumping. The laser still shows lasing with a lasing threshold around  $270 \mu\text{J}/\text{cm}^2$ . For the *flash* CdSe/CdS core/shell colloidal QDs we used for our laser, measurements reported in section 4.1 show these dots exhibit a  $2 \text{ ns}^{-1}$  biexciton decay rate, which corresponds to a 500 ps biexciton lifetime. Compared to this biexciton lifetime, our 7 ns pump actually can be considered as quasi-CW pumping, with an equivalent lasing threshold around  $39 \text{ kW}/\text{cm}^2$ . This opens prospects in terms of CW operation and, consequently, an extended application potential. The intrinsic combination with the mature SiN-waveguide platform then immediately opens the path towards more complex devices such as tunable lasers and arrays of single mode lasers or integration with passive structures such as on-chip spectrometers.

Interestingly, colloidal QDs as solution processed materials at low cost, can be directly patterned onto a substrate. We have used this feature to demonstrated gain-coupled DFB lasers based on an optimized colloidal patterning technique. The laser shows single mode lasing without phase shifter in the middle of the laser cavity. The threshold is around  $950 \mu\text{J}/\text{cm}^2$  @532 nm under the pulsed optical pump.

We have tried to combine colloidal nano-platelets (NPLs) with the SiN waveguide platform. The NPLs still show their ASE after embedding them into the SiN layer stacks. A material gain coefficient around  $3500 \text{ cm}^{-1}$  can be extracted from the VSL measurement. This showcases the design versatility of hybrid integrated photonics platforms. Our optimized hybrid SiN waveguide platform can potentially be used for other colloidal nano-crystals integration.

Colloidal QDs are candidates for realizing single photon emitters operating at room temperature. Our developed SiN waveguide platform can also be used to integrate colloidal QDs to realize on-chip single photon sources. However, to characterize these QD based integrated single photon sources and the associated photonic circuits, compact, efficient and broad-band couplers are needed to couple light from a chip to an objective. In this thesis, we have demonstrated the design, fabrication and characterization of an ultra-compact SiN grating coupler. The grating coupler is designed to maximize the coupling between a suspended SiN waveguide and a microscopy system. With the optimized parameters and using only 3 periods, we experimentally demonstrated a 53% coupling efficiency from the fundamental TE mode (@ 632.8 nm) to a microscopy system with 0.65 NA. 116 nm 1dB bandwidth can be theoretically achieved, due to the high contrast of the grating and a large collection angle from the microscopy system. We have tried to embed nano patches of monolayer colloidal QDs into the suspended waveguide. With optical pumping, the emission from the embedded nano patches can be well coupled to the optical mode of the waveguide. With the help of the grating coupler, these emissions can also be coupled out to the collection objective.

In conclusion, this thesis has shown a successfully developed hybrid integration photonics platform, which combines the excellent optical emission properties of colloidal QDs with the SiN waveguide platform. Based on this platform, we have demonstrated hybrid laser sources with low thresholds. Work towards the realization of on-chip single photon sources with this platform has been carried out. The results demonstrate the potential to build integrated single photon sources and the associated photonic circuits with this platform.



# 1

## Introduction

### 1.1 Photonics integration<sup>1</sup>

The word light is originally derived from the old English word *lēoht*, which means the power of vision. With the help of our eyes, humans are able to detect the existence of the light. The curiosity about how light generates and interacts with matter led to the development of a very ancient physical science, Optics. The Chinese philosopher Mozi, who lived from 470 BC to 391 BC, already described eight fundamental laws about optics. The founder of the School of Alexandria, Euclid, has also published the book called “Optics”, in around 280 BC, which also contains the fundamental understanding of light.

In the 19<sup>th</sup> century, with the development of modern science, people started to get a further understanding about light: it is an electromagnetic (EM) wave, which has a wavelength range extending from the ultra-violet (UV) at around 50 nm to the far infrared at around 1 mm. The detailed EM wave spectrum with the scale of wavelength is shown in Figure 1.1 [2].

In 1917, Einstein elaborated on two forms of light generation when he studied atomic radiation. One is the spontaneous emission; the other is stimulated radiation generated by the induced excitation of external photons. Based on his

---

<sup>1</sup> This part is partly inspired by the introduction of ref [1].

research, he predicted that stimulated radiation could produce monochromatic light with very high brightness that propagates in a certain direction. T. H. Maiman demonstrated the 1<sup>st</sup> laser in 1960 at Hughes Research Laboratories in Malibu. The components and structures are presented in Figure 1.2 [3]. His invention experimentally demonstrated a new light source with exceptional coherence and brightness.

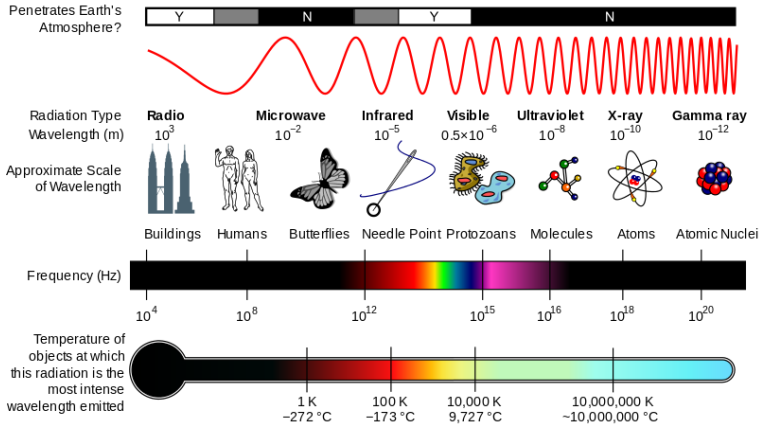


**Figure 1.1:** A diagram of the electromagnetic spectrum, showing various properties across the range of frequencies and wavelengths.[2]

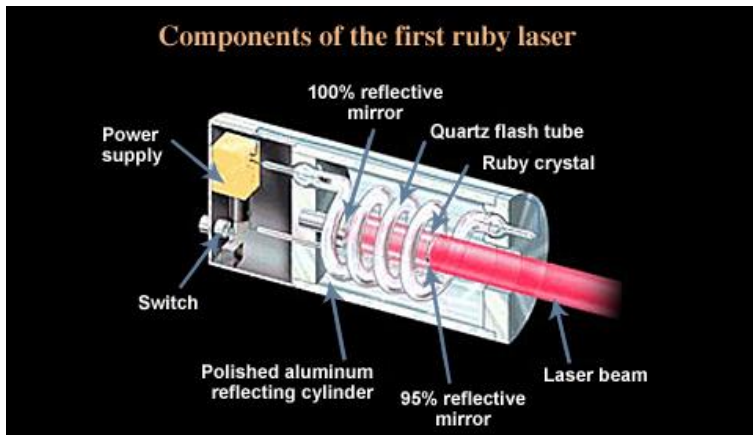


**Figure 1.2:** The components of the 1st ruby laser by T.H. Maiman [4].

It was immediately understood that the coherence of the laser potentially could enable high-speed telecommunications. But was there a medium that can support light transmission with ultra-low loss? In 1966, British Chinese Charles Kao published a paper proposing the production of glass fiber using quartz, which can keep the propagation loss down to 20 dB/km [5]. At that time, only a

few people believed such a fiber could be demonstrated experimentally. In 1970, Corning demonstrated a silica fiber with a loss as low as 20 dB/cm for the first time, with a length about 30 meters, costing around \$30 million.

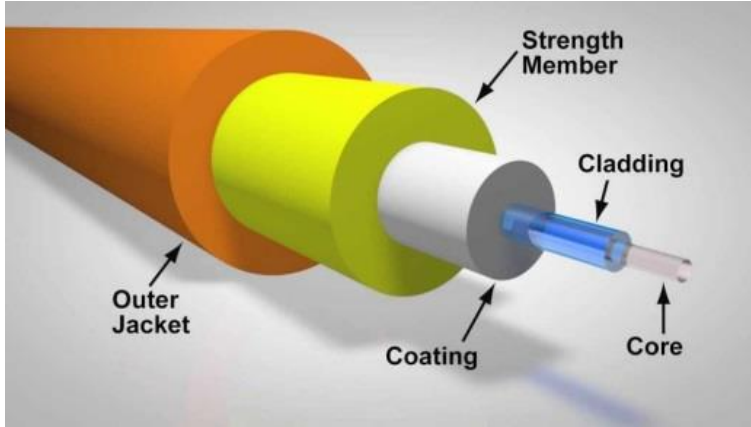


**Figure 1.3:** The structure of the normal optical fiber [6].

With further development of the fabrication process, nowadays people can get fibers with loss less than 0.5dB/km for a price less than \$ 5/km (Figure 1.3).

The matured semiconductor technologies also enable us to generate and detect light with very efficient and compact opto-electronic devices. In 1976, Bell labs set up an experimental fiber circuit with LEDs as light sources, in Atlanta, Washington, with a transmission rate of only 45 Mb/s. This rate can support only hundreds of telephone calls while using a coaxial cable can transmit 1800 telephone lines. In 1984, by using a semiconductor laser, the rate of optical fiber communication could reach 144 Mb/s, equivalent to 1920 telephone. In 2017, the newest record shows it is possible to have a transmission distance of one Pbit/s capacity over a single strand of optical fiber within a single optical amplifier bandwidth (C-band) [7].

With the development of semiconductor technology, microelectronics can realize the same functionalities as bulky devices within a micro-sized silicon chip. In 1972, Somekh and Yariv proposed to use semiconductor technology to build an on-chip platform, combining the optical functions and the electronic functions. In this platform, light or photons, are confined in dielectric material waveguides. Since electronics can be considered to describe the flow of electrons, the word “photonics” is used to describe the flow of photons. This proposal has now become a new branch of optics, called integrated photonics. The classical optics components, like lenses, mirrors, filters, etc., are switched with a new family of integrated photonics components including waveguides, beam splitters, gratings, couplers, polarizers, interferometers, sources, modulators and detectors. By combining these components as building blocks,

complex integrated photonics systems can be built to perform a wide range of functions with applications like optical communication systems, optical sensors etc., with much smaller dimensions compared with systems realized in bulk materials. A second major step forward came with the development of semiconductor optical devices allowing the generation and detection of light, which permitted very efficient and compact optoelectronic devices [1].

### 1.1.1 Silicon photonics

Silicon photonics has become one of the leading integrated photonics solutions that target applications such as high-performance computing [8], optical communications (telecom/datacom) [9], optical sensors [10] and on-chip optical interconnects [11]. Silicon integration platforms are usually realized with silicon-on-insulator (SOI) wafers, which are supported by the already matured complementary metal-oxide-semiconductor (CMOS) technology platform that has dominated the microelectronics industry during the last 40 years.

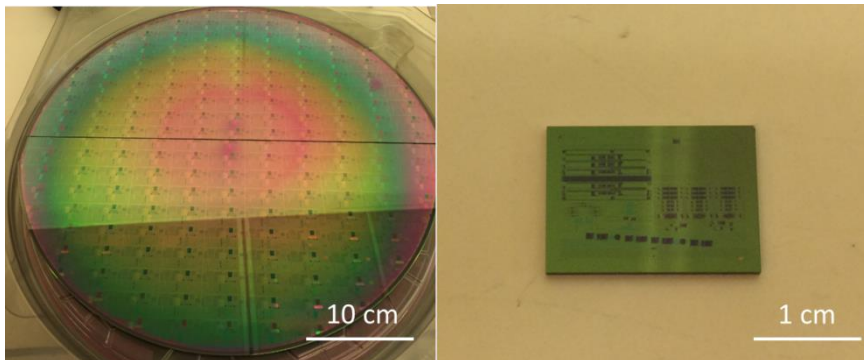


**Figure 1.4:** Silicon wafer with integrated photonics circuits. Left: 400 mm silicon wafer; right: diced small chips.

The SOI wafer layer stack comprises a thin layer of crystalline silicon. This layer of crystalline silicon is separated from the silicon substrate by a buried oxide (BOX) layer. SOI technology has been developed and shown impressive performance for passive and active functions as a mature photonics integrated platform during the past years. Compared to III-V materials and polymers, SOI has the advantage of having a high refractive index, and hence a high refractive index contrast with both silicon oxide and air. Therefore it can confine light in much smaller waveguide cross section and also makes the typical dimensions of the photonics circuits more compact. Moreover, as the preferred material system in the electronics industry, it is fully compatible with the fabrication techniques and facilities used in the mature microelectronics industry and can easily be

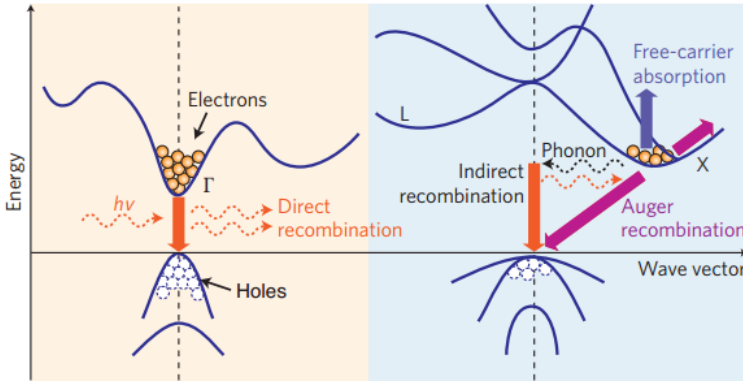


**Figure 1.5:** The energy wave vector comparison with direct bandgap semiconductor material and indirect bandgap semiconductor material. Adapted from ref [12].

combined with electronics for richer, and more complex applications. The drawback is that silicon is an indirect bandgap semiconductor material (Figure 1.4), meaning that light generation is inefficient and difficult to achieve.

The success of silicon photonics has opened the research directions towards new applications with new wavelengths extending silicon material's transparent window (from 1.1  $\mu\text{m}$  to 4  $\mu\text{m}$ ), to visible and near infrared. These wavelengths could be relevant for several types of sensing applications. To provide a transparent window for visible and near infrared photonics, the field of silicon photonics has been broadened to include silicon nitride (SiN) as an alternative integrated photonics platform [13].

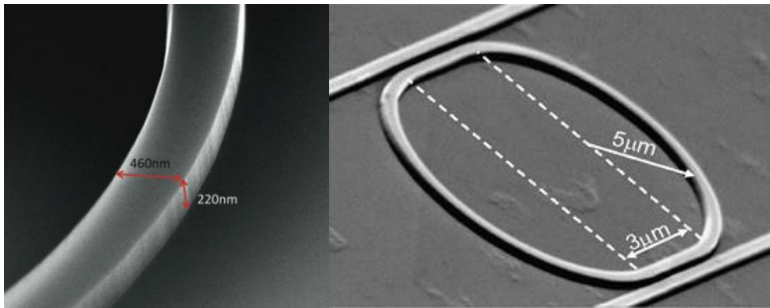


**Figure 1.6:** The left picture: SEM view of a silicon photonic wire waveguides fabricated with the process from [14]; the right picture: SEM view of a silicon micro ring resonator [15].

### 1.1.2 Silicon nitride photonics

SiN is commonly used for masking, strain engineering and passivation in CMOS foundries. The material stack used for the SiN-based photonics integration platform is similar to that of the SOI-based photonics integration platform. The only difference is that the layer that forms the optical waveguide is replaced by a layer of SiN layer. Compared with the SOI platform, SiN platform has a wider transparency window, extending from the visible to the near-infrared, which provides possibilities to realize photonics integration applications in this wavelength range. The SiN platform provides lower index contrast compared with the SOI platform, resulting in a larger footprint for the integrated components. However, as we know, the waveguide propagation loss, is typically proportional to  $\Delta n^2$  [16],

$$\Delta n^2 = n_{core}^2 - n_{cladding}^2 \quad (1.1)$$

That means the waveguide propagation loss can be much lower due to the lower index contrast. A waveguide propagation loss with 0.003 dB/cm is reported in ref [17]. The waveguide used in this reference has a cross section size at 2.8  $\mu\text{m}$  by 80 nm, which leads to low optical confinement. For high optical confinement SiN waveguide, a waveguide propagation loss at 0.37 dB/cm with 800 nm by 800 nm in dimension has been reported in [18]. Moreover, other than the silicon layer on top of the SOI wafer, SiN is usually deposited with plasma enhanced chemical vapor deposition (PECVD) or low pressure chemical vapor deposition (LPCVD) systems, which provides the flexibility for choosing the substrate and makes 3D waveguides and 3D integration possible [19]. Besides the advantages mentioned above, the SiN waveguide platform also exhibits other advantages, e.g. the lack of two-photon absorption, temperature insensitivity and less distributed backscattering compared to the SOI platform.

Applications like on-chip Raman spectroscopy [20] and biosensors [21] based on the SiN integration platform have been studied and demonstrated in the NIR and visible wavelength range.

However, like silicon, SiN is also not a good material for light emission. Some early demonstrations focused on using nonlinear optics to achieve light generation with SiN waveguides [22]. This technique needs a high power pulsed laser as the pumping source, which is not very practical in the long term.

### 1.1.3 Heterogeneous integration

To solve the light generation problem, researchers have attempted to integrate other active materials on silicon photonics circuits. For the traditional datacom/telecom application of light generation (1300 nm – 1600 nm),

significant advances have been made by bonding active III-V chips to the top of silicon photonics circuits [12] [23].

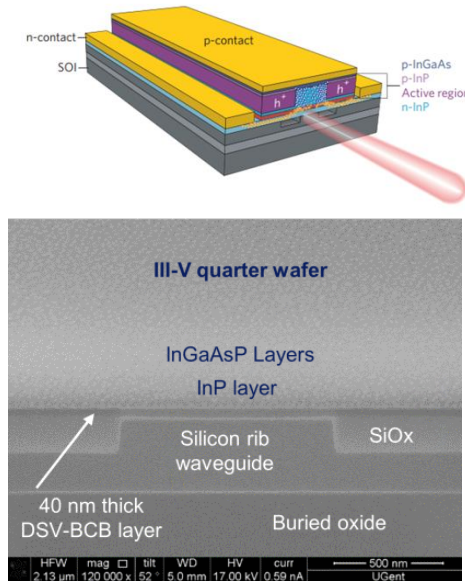


**Figure 1.7:** Bonding active III-V chips to the top of silicon photonics circuits. Adapted from ref [12] [23].

Electrically pumped III-V distributed feedback (DFB) lasers with very high modulation speed have been demonstrated (up to 56 Gbps) [24], which make them very promising coherent light sources for today's silicon photonics applications in telecom/datacom wavelength range.

Some other directions have also been explored. Techniques to directly grow III-V material on top of silicon have been studied and optically and electrically pumped lasing has been recently demonstrated [25][26].

Colloidal quantum dots (QDs), compared with other epitaxial materials, have advantages in terms of costs and emission efficiency in the visible range. In this thesis, we aim at using the heterogeneous integration principle to explore the possibilities to integrate colloidal QDs as an alternative material for light generation on the silicon nitride platform, specifically in the visible light range.

### 1.1.4 Colloidal quantum dots

One of the defining features of semiconductors is their band gap ( $E_g$ ), which separates the valence band and the conduction band. The wavelength of the light emitted by this semiconductor material and the optical absorption spectrum is both directly determined by the width of this special band gap feature. In

semiconductors with macroscopic sizes, the band gap width is a pre-determined parameter, which is related to the material composition and structure. However, band gap width is a bit different in nanometer-sized semiconductor particles (typical dimensions are less than 10-20 nm). In these nanometer-sized semiconductor particles, the band gap is not only dependent on the material composition and structure but also dependent on their dimensions, which are results of the tight spatial confinement of the electron and hole wave functions. This size regime in which this spatial confinement becomes dominant is named as the regime of quantum confinement. And the nanocrystals that show this spatial confinement are often referred to as quantum dots.



**Figure 1.8:** When they are excited by ultraviolet light (pictured), colloidal quantum dots fluoresce at different colors depending on the particle size.

Colloidal QDs are nanometer-sized semiconductor particles synthesized and suspended in the solution phase. While the use and application of colloidal metal nano-particles go back thousands of years, it is only since a few decades ago, with the improved nanotechnology, that people can understand, fabricate and engineer these nano-sized crystals at will. Ekimov *et al.* [27-31] Efros *et al.* [32-35] and Brus *et al.* [36-38] were the pioneers in this field. They, for the first time, studied in depth these tiny crystals containing a few hundred to a few thousands of atoms. These tiny semiconductor clusters are still arranged on the regular bulk semiconductor lattice of the crystal, even though the sizes are in the 1 to 10 nm range. Initially, glass-based nanocrystals were used to study the electronic and optical properties of strong quantum confinement, including the electron-photon interactions, structure of electronic states, intra-band relaxation, nonlinear optical phenomena, Auger processes, and the physics of optical gain and lasing. The optical properties of QDs fundamentally arise from the quantum confinement which relate to their size and Bohr radius  $a_B$ . For this analysis, according to the  $a_B$  of the bulk exciton and ratio of the QD radius  $R$ , one can have three different regimes: weak confinement regime for  $R > a_B$ , intermediate confinement regime for  $R \sim a_B$ , and strong confinement regime for  $R < a_B$  [31]. In the third case, which is the strong confinement regime case, without considering the Coulomb interaction between the electron and hole in the QDs,

the size-dependent energy gap  $E_g(\text{QD})$  (the lowest transition states) relates to the bulk semiconductor energy gap  $E_g(\text{bulk})$  can be expressed using equation as  $E_g(\text{QD}) = E_g(\text{bulk}) + \hbar^2\pi^2/(2m^*R^2)$ , where  $1/m^* = 1/m_h + 1/m_e$ . Here the  $m_h$  and  $m_e$  are the effective masses of the holes and electron, respectively [37]. We can have a strong size dependent blue-shifted band gap of a QD compared to the bulk one with the same material, based on this equation. This has been experimentally demonstrated, which has been nicely shown in Figure 1.9.

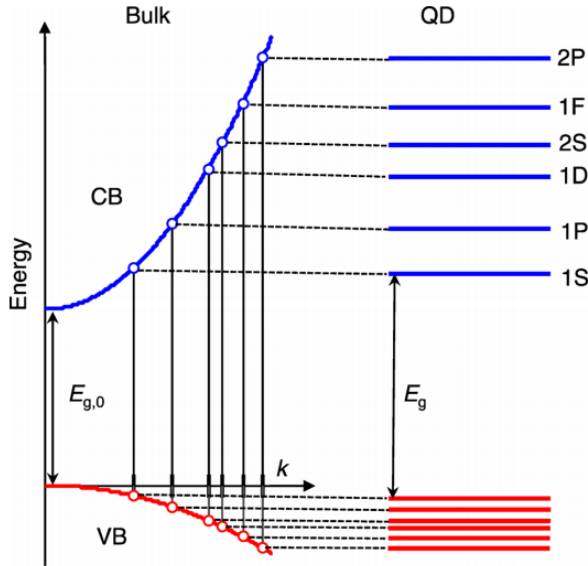


**Figure 1.9:** An idealized model of electronic states in a spherical QD made of the same material (right) and a bulk semiconductor (left). Continuous bands of a bulk semiconductor with a parabolic dispersion of carrier kinetic energies ( $E_k \propto k$ ;  $k$  is the wave vector) in the valence and conduction bands (denoted VB and CB, respectively) has been transformed into discrete atomic-like levels in the case of the atomic-like colloidal QD. Adapted from ref [39].

Eventually, to improve the optical properties of these nanocrystals, researchers have put more efforts in the direction of colloidal samples synthesis that allowed for narrower size distribution, more facile size control and improved surface passivation [40]. The colloidal QDs now we are using, usually comprise a layer of organic molecules which caps the semiconductor core. This organic capping not only prevents uncontrolled growth, agglomeration of the colloidal QDs but also allows nanocrystals to be able to chemically manipulate like large molecules, with solubility and chemical reactivity determined by surface capping groups. Additionally, “electronic”

passivation is provided by the capping molecules on the nanocrystal surfaces. This passivation helps to terminate dangling bonds, which would potentially act as surface traps which can deplete the excitons via rapid non-radiative process.

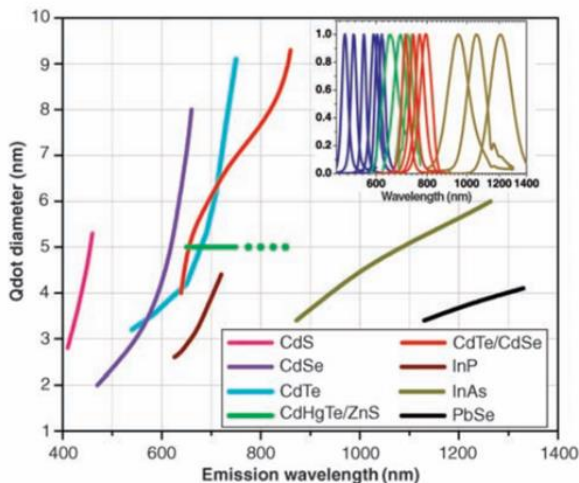


**Figure 1.10:** Emission wavelength and sizes of colloidal QDs of different composition. Colloidal QDs can be synthesized using different types of semiconductor materials (II-VI: CdS, CdSe, CdTe; III-V: InP, InAs; IV-VI: PbSe) with different bulk band gap energies. The curves in the figure represent experimental data from the literature on the dependence of peak emission wavelength on colloidal QDs diameter. The range of emission wavelength is 400 to 1350 nm, with size varying from 2 to 9.5 nm (organic passivation/solubilization layers not included). All spectra typically have full width at half maximum around 30 to 50 nm. Inset: The emission spectra for different materials covering from 400 nm to 1350 nm. Adapted from ref [41].

The colloidal synthesis has been eventually adapted for IV-VI, III-V or even Group IV materials. Core/shell structures with different core and/or shell thickness and alloyed interface can also be used to tune the properties of the QDs. An emission spectrum range from 400 nm to 1350 nm can be achieved by using different compounds and sizes, as shown in Figure 1.10 [41].

With the improvement of the synthesis, a wide range of applications became within reach of colloidal QDs, such as bio-imaging, bio-labelling, photovoltaics, light-emitting diodes, laser sources and single photon sources.

## 1.2 Definition of the research objective

In this thesis, we aim to use the heterogeneous integration principle to explore the possibilities to integrate colloidal QDs as an active material for light generation on the silicon nitride platform, specifically in the visible light range.

Colloidal QDs exhibit optical amplification and single photon emission properties under different optical pumping conditions. With the existence of the multi-exciton<sup>2</sup>, colloidal QDs shows optical amplification property; this can be used as a gain material to realize on-chip laser sources in the SiN platform. With the existence of the single-exciton, colloidal QDs can be a good single photon source, this can be used to realize on-chip single photon source in the SiN platform.

The first objective of this thesis is to investigate the possibility to achieve on-chip lasers based on colloidal QDs as the gain material. A hybrid SiN colloidal QDs integration platform has been developed and demonstrated. The colloidal QDs can be embedded between SiN films without quenching their luminescence, while the SiN waveguide can still maintain low optical loss. The colloidal QDs layer's gain property has been characterized by a waveguide based variable stripe method. DFB lasers based on this hybrid SiN colloidal QDs platform have been designed, fabricated and characterized. The lasers show lasing under femto-second laser pumping and nano-second laser pumping. The relatively low lasing threshold shows the potential to realize on-chip continuous wave pumped colloidal QD laser using the same hybrid waveguide platform.

The second objective of the thesis is to investigate the possibility to achieve an on-chip single photon source based on colloidal QDs. We first designed, fabricated and characterized an ultra-compact SiN grating coupler aiming to maximize the coupling efficiency between the SiN waveguide and a microscope system. Then we embedded a mono layer of nano-size colloidal QDs patches into the SiN waveguide. The emission of the colloidal QDs is coupled out efficiently by the optimized grating coupler. The embedded patches can be further reduced in size towards the single dot level and the developed process shows the potential to realize on-chip single photon sources based on colloidal QDs.

The research was carried out in a close collaboration between the Ghent University Photonics Research Group (PRG) and the Physics and Chemistry of Nanostructures (PCN) group, which have ample expertise in respectively integrated photonic devices and the synthesis and characterization of colloidal QDs.

---

<sup>2</sup> Single excitons gain can be possible with certain mechanism, which will be explained in Chapter 2.1.3

### 1.3 Thesis outline

In this chapter, we presented the background of integrated photonics and semiconductor colloidal QDs. The excellent luminescent properties of colloidal QDs motivated us to combine colloidal QDs with the SiN photonics integration platform.

In Chapter 2, we will introduce the detailed background of the colloidal QDs as novel emitting materials. In the first part of this chapter, we will introduce the detail of the gain properties of colloidal QDs. Then we will also introduce the potential of using colloidal QDs as single photon sources.

In Chapter 3, we will show the information about the development of the hybrid SiN colloidal QDs integration platform. The different SiN layer deposition details will be presented. The waveguide loss with and without the colloidal QDs will be shown. The SiN layer stress for different deposition recipes will be presented. The luminescence of the SiN material itself for different deposition recipe will also be compared.

In Chapter 4, we present the work using colloidal QDs as gain material. The gain coefficient of the embedded colloidal QDs will be first measured using a waveguide-based variable stripe length methods. Later, a DFB based laser is designed, fabricated and characterized. The laser shows a quasi-continuous-wave (CW) pump threshold around  $39 \text{ kW/cm}^2$ . This measured threshold is at the same level as that of III-V semiconductor lasers epitaxially grown on silicon. This opens strong prospects in terms of CW operation and, consequently, application potential. We also present the design, fabrication and characterization of a gain coupled DFB laser based on colloidal QDs. At the end of this chapter, we also show that this hybrid SiN colloidal QDs integration platform can potentially also be used for a new class of solution processed nanomaterials, i.e. nano-platelets.

In Chapter 5, we present our work on the integration of patches of mono layer colloidal QDs in a SiN waveguide aiming to demonstrate on-chip single photon sources. In the first part, the design, fabrication and characterization of an ultra-compact grating coupler optimized for use in a microscopy system is presented. The grating coupler is aiming to maximize the coupling efficiency from the optical mode of the waveguide to a microscopy system with certain numerical aperture. The experiment shows up to 53% coupling efficiency to a NA= 0.65 microscopy system has been demonstrated. Simulations show this efficiency can increase up to 75% for NA = 0.95. In the second part, we embedded patches of monolayer colloidal QDs into the waveguide. The emission can be well coupled to the waveguide and coupled out by the optimized compact grating coupler. In combination with the earlier developed single colloidal QD patterning technique

[42], this shows this hybrid integration platform has the potential to realize single photon sources.

Finally, Chapter 6 summarizes the work presented in this thesis and discusses proposals for further work.

## 1.4 Publications

### Publications in international journals

1. **Y. Zhu**, W. Xie, P. Geiregat, S. Bisschop, T. Aubert, E. Brainis, Z. Hens, D. Van Thourhout, "On-Chip Single Mode Distributed Feedback Colloidal Quantum Dot Laser under Nanosecond Pumping", *ACS Photonics* 4, no. 10 (2017): 2446-2452
2. **Y. Zhu**, J. Wang, W. Xie, B. Tian, Y. Li, E. Brainis, Y. Jiao, D. Van Thourhout, "Ultra-compact Silicon Nitride Grating Coupler for Microscope System", *Optics Express*, 25(26), p.33297-33305 (2017)
3. M. Kolarczik, C. Ulbrich, P. Geiregat, **Y. Zhu**, L.K. Sager, A. Signh, B. Herzog, A.W. Achtstein, X Li, D. Van Thourhout, Z. Hens, N. Owschimikow, U. Woggon, "Sideband Pump-probe Technique Resolves Nonlinear Modulation Response of PbS/CdS Quantum Dots on a Silicon Nitride Waveguide at High Excitation Rates", 3(1), p.016101 (2018)
4. Z. Wang, A. Abbasi, U.D. Dave, A. De Groote, S. Kumari, B. Kunert, C. Merckling, M. Pantouvaki, Y. Shi, B. Tian, K. Van Gasse, J. Verbist, R. Wang, W. Xie, J. Zhang, **Y. Zhu**, J. Bauwelinck, X. Yin, Z. Hens, J. Van Campenhout, B. Kuyken, R. Baets, G. Morthier, D. Van Thourhout, G. Roelkens, "Novel light source integration approaches for silicon photonics", *Laser & Photonics Reviews* 11, no. 4 (2017)
5. W. Xie, **Y. Zhu**, S. Bisschop, T. Aubert, Z. Hens, D. Van Thourhout, P. Geiregat "Colloidal Quantum Dots enabling Coherent Light Sources for Integrated Silicon-Nitride Photonics", *IEEE Journal of Selected Topics in Quantum Electronics* 23, no. 5 (2017): 1-13.
6. W. Xie, T. Stoferle, G. Raino, T. Aubert, S. Bisschop, **Y. Zhu**, R. Mahrt, P. Geiregat, E. Brainis, Z. Hens, D. Van Thourhout, "On-chip Integrated Quantum-dot Silicon Nitride Microdisk Lasers", *Advanced Materials* 29, no. 16 (2017).
7. W. Xie, **Y. Zhu**, T. Aubert, Z. Hens, E. Brainis, D. Van Thourhout, "Fabrication and Characterization of On-chip Silicon Nitride Microdisk

- Integrated with Colloidal Quantum Dots", *Optics Express*, 24(2), p.A114-A122 (2016)
8. W. Xie, R. Gomes, T. Aubert, S. Bisschop, **Y. Zhu**, Z. Hens, E. Brainis, D. Van Thourhout, "Nanoscale and Single-Dot Patterning of Colloidal Quantum Dots", *Nano Lett.*, 15(11), p.7481-7487 (2015)
  9. W. Xie, **Y. Zhu**, T. Aubert, S. Verstuyft, Z.Hens, D. Van Thourhout, "Low-Loss Silicon Nitride Waveguide Hybridly Integrated With Colloidal Quantum Dots", *Optics Express*, 23(9), p.12152-12160 (2015)

### **Publications in international conferences**

1. **Y. Zhu**, W. Xie, P. Geiregat, S. Bisschop T. Aubert, E. Brainis, Z. Hens, D. Van Thourhout, "On-chip Low-threshold Silicon Nitride Distributed Feedback Colloidal Quantum Dot Laser", CLEO 2017, Applications and Technology (pp. JW2A-126). Optical Society of America
2. S. Bisschop, P. Geiregat, **Y. Zhu**, W. Xie, T. Aubert, E. Brainis, D. Van Thourhout, Z. Hens, "Optical Gain with Colloidal Quantum Dots: From material photo-physics to integrated devices", Proceedings of the 21th Annual Symposium of the IEEE Photonics Benelux Chapter, 2016
3. W. Xie, T. Stoferle, G. Raino, T. Aubert, S. Bisschop, **Y. Zhu**, R. Mahrt, E. Brainis, Z. Hens, D. Van Thourhout, "Integrated Silicon Nitride Microdisk Lasers Based on Quantum Dots", CLEO 2016, Science and Innovations (pp. JTh4B-6). Optical Society of America, **Post-deadline Paper**
4. **Y. Zhu**, W. Xie, P. Geiregat, S. Bisschop T. Aubert, E. Brainis, Z. Hens, D. Van Thourhout, "Hybrid Colloidal Quantum Dot Silicon Nitride Waveguide Gain Measurement Based on Variable Stripe Length Method", CLEO 2016, Applications and Technology (pp. ATh1J-5). Optical Society of America
5. M. Klarczyk, B. Herzog, C. Ulbrich, Y. Kaptan, U. Woggon, N. Owschimikow, A. Singh, X. Li, **Y. Zhu**, D. Van Thourhout, P. Geiregat, Z. Hens, "Biexciton-mediated Modulation Response of Colloidal Quantum Dots Deposited on a Silicon Nitride Waveguide at High Laser Excitation Rate", CLEO 2016, Applications and Technology (pp. JTu5A-44). Optical Society of America
6. **Y. Zhu**, Y. Jiao, W. Xie, J. Wang, B. Tian, E. Brainis, D. Van Thourhout, "Ultra-compact Silicon Nitride Grating Coupler for on-chip Single Photon Source", EMRS Spring Meeting 2016

7. **Y. Zhu**, Y. Jiao, J. Wang, W. Xie, B. Tian, D. Van Thourhout, "Ultra-compact Silicon Nitride Grating Coupler for Microscopy System", Proceedings of the 20th Annual Symposium of the IEEE Photonics Benelux Chapter, Belgium 2015
8. W. Xie, **Y. Zhu**, T. Aubert, Z. Hens, E. Brainis, D. Van Thourhout, "On-chip Hybrid Integration of Silicon Nitride Microdisk With Colloidal Quantum Dots", 12th International Conference on Group IV Photonics, Canada 2015
9. S. Bisschop, **Y. Zhu**, W. Xie, A. Guille, Z. Hens, D. Van Thourhout, E. Brainis , "Progress Towards On-chip Single Photon Sources Based on Colloidal Quantum Dots in Silicon Nitride Devices", CLEO 2014, QELS Fundamental Science (pp. JW2A-127). Optical Society of America
10. **Y. Zhu**, W. Xie, S. Verstuyft, T. Aubert, Z. Hens, D. Van Thourhout, "Colloidal Quantum Dot Silicon Nitride Platform", Proceedings of the 2013 Annual Symposium of the IEEE Photonics Society Benelux Chapter, Netherlands 2013

## References

- [1] Lifante, Ginés. *Integrated photonics: fundamentals*. John Wiley & Sons, 2003.
- [2] [https://en.wikipedia.org/wiki/Electromagnetic\\_spectrum#/media/File:EM\\_Spectrum\\_Properties\\_edit.svg](https://en.wikipedia.org/wiki/Electromagnetic_spectrum#/media/File:EM_Spectrum_Properties_edit.svg) Inductiveload, NASA - self-made, information by NASA Based off of File:EM Spectrum3-new.jpg by NASA The butterfly icon is from the P icon set, P biology.svg The humans are from the Pioneer plaque, Human.svg The buildings are the Petronas towers and the Empire State Buildings, both from Skyscrapercompare.svg
- [3] Mainman, Theodore Harold. "Stimulated optical radiation in ruby." *Nature* 189 (1960): 493.
- [4] <http://www.laserfest.org/lasers/how/ruby.cfm>
- [5] Kao, K. C., and George A. Hockham. "Dielectric-fibre surface waveguides for optical frequencies." In *Proceedings of the Institution of Electrical Engineers*, vol. 113, no. 7, pp. 1151-1158. IET Digital Library, 1966.
- [6] <http://community.fs.com/blog/the-advantages-and-disadvantages-of-optical-fibers.html>
- [7] <https://www.nttreview.jp/archive/ntttechnical.php?contents=ntr201706sr1.html>
- [8] Taubenblatt, Marc A. "Optical interconnects for high-performance computing." *Journal of Lightwave Technology* 30, no. 4 (2012): 448-457.
- [9] Jalali, Bahram, and Sasan Fathpour. "Silicon photonics." *Journal of lightwave technology* 24, no. 12 (2006): 4600-4615.
- [10] Dell'Olio, Francesco, and Vittorio MN Passaro. "Optical sensing by optimized silicon slot waveguides." *Optics Express* 15, no. 8 (2007): 4977-4993.
- [11] Levy, Jacob S., Alexander Gondarenko, Mark A. Foster, Amy C. Turner-Foster, Alexander L. Gaeta, and Michal Lipson. "CMOS-compatible multiple-wavelength oscillator for on-chip optical interconnects." *Nature photonics* 4, no. 1 (2010): 37-40.
- [12] Liang, Di, and John E. Bowers. "Recent progress in lasers on silicon." *Nature photonics* 4, no. 8 (2010): 511-517.
- [13] Rahim, Abdul, Eva Ryckeboer, Ananth Z. Subramanian, Stéphane Clemmen, Bart Kuyken, Ashim Dhakal, Ali Raza et al. "Expanding the

- Silicon Photonics Portfolio With Silicon Nitride Photonic Integrated Circuits." *Journal of Lightwave Technology* 35, no. 4 (2017): 639-649.
- [14] Selvaraja, Shankar Kumar, Patrick Jaenen, Wim Bogaerts, Dries Van Thourhout, Pieter Dumon, and Roel Baets. "Fabrication of photonic wire and crystal circuits in silicon-on-insulator using 193-nm optical lithography." *Journal of Lightwave Technology* 27, no. 18 (2009): 4076-4083.
- [15] Bogaerts, Wim, Peter De Heyn, Thomas Van Vaerenbergh, Katrien De Vos, Shankar Kumar Selvaraja, Tom Claes, Pieter Dumon, Peter Bienstman, Dries Van Thourhout, and Roel Baets. "Silicon microring resonators." *Laser & Photonics Reviews* 6, no. 1 (2012): 47-73.
- [16] Tien, P. K. "Light waves in thin films and integrated optics." *Applied optics* 10, no. 11 (1971): 2395-2413.
- [17] Bauters, Jared F., Martijn JR Heck, Demis John, Daoxin Dai, Ming-Chun Tien, Jonathon S. Barton, Arne Leinse, René G. Heideman, Daniel J. Blumenthal, and John E. Bowers. "Ultra-low-loss high-aspect-ratio Si<sub>3</sub>N<sub>4</sub> waveguides." *Optics express* 19, no. 4 (2011): 3163-3174.
- [18] Epping, Jörn P., Marcel Hoekman, Richard Mateman, Arne Leinse, René G. Heideman, Albert van Rees, Peter JM van der Slot, Chris J. Lee, and Klaus-J. Boller. "High confinement, high yield Si<sub>3</sub>N<sub>4</sub> waveguides for nonlinear optical applications." *Optics express* 23, no. 2 (2015): 642-648.
- [19] Shang, Kuanping, Shibnath Pathak, Binbin Guan, Guangyao Liu, and S. J. B. Yoo. "Low-loss compact multilayer silicon nitride platform for 3D photonic integrated circuits." *Optics express* 23, no. 16 (2015): 21334-21342.
- [20] Dhakal, Ashim, Frédéric Peyskens, Stéphane Clemmen, Ali Raza, Pieter Wuytens, Haolan Zhao, Nicolas Le Thomas, and Roel Baets. "Single mode waveguide platform for spontaneous and surface-enhanced on-chip Raman spectroscopy." *Interface focus* 6, no. 4 (2016): 20160015.
- [21] Martens, Daan, and Peter Bienstman. "Comparison between Vernier-cascade and MZI as transducer for biosensing with on-chip spectral filter." *Nanophotonics* (2017).
- [22] Zhao, Haolan, Bart Kuyken, Stéphane Clemmen, François Leo, Ananth Subramanian, Ashim Dhakal, Philippe Helin et al. "Visible-to-near-infrared octave spanning supercontinuum generation in a silicon nitride waveguide." *Optics letters* 40, no. 10 (2015): 2177-2180.

- [23] Keyvaninia, Shahram, Muhammad Muneeb, Stevan Stanković, P. J. Van Veldhoven, Dries Van Thourhout, and Günther Roelkens. "Ultra-thin DVS-BCB adhesive bonding of III-V wafers, dies and multiple dies to a patterned silicon-on-insulator substrate." *Optical Materials Express* 3, no. 1 (2013): 35-46.
- [24] Abbasi, Amin, Bart Moeneclaey, Jochem Verbist, Xin Yin, Johan Bauwelinck, Guang-Hua Duan, Gunther Roelkens, and Geert Morthier. "Direct and electro-absorption modulation of a III-V-on-silicon DFB laser at 56 Gbps." *IEEE Journal of Selected Topics in Quantum Electronics* (2017).
- [25] Wang, Zhechao, Bin Tian, Marianna Pantouvaki, Weiming Guo, Philippe Absil, Joris Van Campenhout, Clement Merckling, and Dries Van Thourhout. "Room temperature InP DFB laser array directly grown on (001) silicon." *Nat. Photon* 9 (2015): 837-842.
- [26] Wan, Yating, Justin Norman, Qiang Li, M. J. Kennedy, Di Liang, Chong Zhang, Duanni Huang et al. "1.3  $\mu\text{m}$  submilliamp threshold quantum dot micro-lasers on Si." *Optica* 4, no. 8 (2017): 940-944.
- [27] Ekimov, A. I., and Alexei A. Onushchenko. "Quantum size effect in three-dimensional microscopic semiconductor crystals." *Jetp Lett* 34, no. 6 (1981): 345-349.
- [28] Ekimov, A. I., and A. A. Onushchenko. "Quantum size effect in the optical-spectra of semiconductor micro-crystals." *Soviet Physics Semiconductors-Ussr* 16, no. 7 (1982): 775-778.
- [29] Ekimov, A. I., Al L. Efros, and Alexei A. Onushchenko. "Quantum size effect in semiconductor microcrystals." *Solid State Communications* 56, no. 11 (1985): 921-924.
- [30] Ekimov, A. I. "Optical properties of semiconductor quantum dots in glass matrix." *Physica Scripta* 1991, no. T39 (1991): 217.
- [31] Ekimov, A. I., F. Hache, M. C. Schanne-Klein, D. Ricard, Chr Flytzanis, I. A. Kudryavtsev, T. V. Yazeva, A. V. Rodina, and Al L. Efros. "Absorption and intensity-dependent photoluminescence measurements on CdSe quantum dots: assignment of the first electronic transitions." *JOSA B* 10, no. 1 (1993): 100-107.
- [32] Efros, Al L., and Al L. Efros. "Interband absorption of light in a semiconductor sphere." *Soviet Physics Semiconductors-Ussr* 16, no. 7 (1982): 772-775.

- [33] Efros, Al L., V. A. Kharchenko, and M. Rosen. "Breaking the phonon bottleneck in nanometer quantum dots: Role of Auger-like processes." *Solid State Communications* 93, no. 4 (1995): 281-284.
- [34] Efros, Al L., M. Rosen, Masaru Kuno, Manoj Nirmal, David J. Norris, and M. Bawendi. "Band-edge exciton in quantum dots of semiconductors with a degenerate valence band: Dark and bright exciton states." *Physical Review B* 54, no. 7 (1996): 4843.
- [35] Efros, Al L., and M. Rosen. "The electronic structure of semiconductor nanocrystals." *Annual Review of Materials Science* 30, no. 1 (2000): 475-521.
- [36] Brus, L. E. "A simple model for the ionization potential, electron affinity, and aqueous redox potentials of small semiconductor crystallites." *The Journal of chemical physics* 79, no. 11 (1983): 5566-5571.
- [37] Rossetti, R., S. Nakahara, and Louis E. Brus. "Quantum size effects in the redox potentials, resonance Raman spectra, and electronic spectra of CdS crystallites in aqueous solution." *The Journal of Chemical Physics* 79, no. 2 (1983): 1086-1088.
- [38] Brus, Louis E. "Electron-electron and electron-hole interactions in small semiconductor crystallites: The size dependence of the lowest excited electronic state." *The Journal of chemical physics* 80, no. 9 (1984): 4403-4409.
- [39] Klimov, Victor I., ed. *Nanocrystal quantum dots*. CRC Press, 2010.
- [40] Pietryga, Jeffrey M., Young-Shin Park, Jaehoon Lim, Andrew F. Fidler, Wan Ki Bae, Sergio Brovelli, and Victor I. Klimov. "Spectroscopic and device aspects of nanocrystal quantum dots." *Chem. Rev* 116, no. 18 (2016): 10513-10622.
- [41] Michalet, X., F. F. Pinaud, L. A. Bentolila, J. M. Tsay, S. J. J. L. Doose, J. J. Li, G. Sundaresan, A. M. Wu, S. S. Gambhir, and S. Weiss. "Quantum dots for live cells, in vivo imaging, and diagnostics." *science* 307, no. 5709 (2005): 538-544.
- [42] Xie, Weiqiang, Raquel Gomes, Tangi Aubert, Suzanne Bisschop, Yunpeng Zhu, Zeger Hens, Edouard Brainis, and Dries Van Thourhout. "Nanoscale and Single-Dot Patterning of Colloidal Quantum Dots." *Nano letters* 15, no. 11 (2015): 7481-7487.



# 2

## Colloidal quantum dots as novel light emitting material

### 2.1 Colloidal quantum dot as gain material

Lasers made from bulk semiconductor materials were first demonstrated around the 1960s [1-2]. They have now found a very wide range of use that includes fiber optic communications, barcode readers, laser pointers, CD/DVD/Blu-ray Disc reading and recording, laser printing, etc. With the development of the laser diode (Figure 2.1), lasing performance has been improved with the introduction of so-called quantum well lasers [3].

In these 2D-gain materials, which are different from traditional bulk semiconductors, the charge carriers (electrons and holes) are confined in a 2D plane (as shown in Figure 2.2). A step-like density of the electronic state is provided by this 2D planar confinement, which is nonzero at the band-edge. This step-like density leads to a higher concentration of carriers that contribute to the band-edge emission, resulting in lower threshold levels.

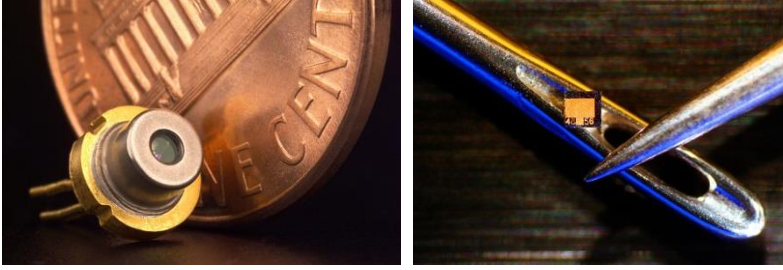


**Figure 2.1:** Left: a packaged laser diode shown with a USD penny for scale. Right: the laser diode chip is removed from the above package and placed on the eye of a needle for scale [4].

The 2D planar confinement also improves the temperature stability and results in a narrower emission line.

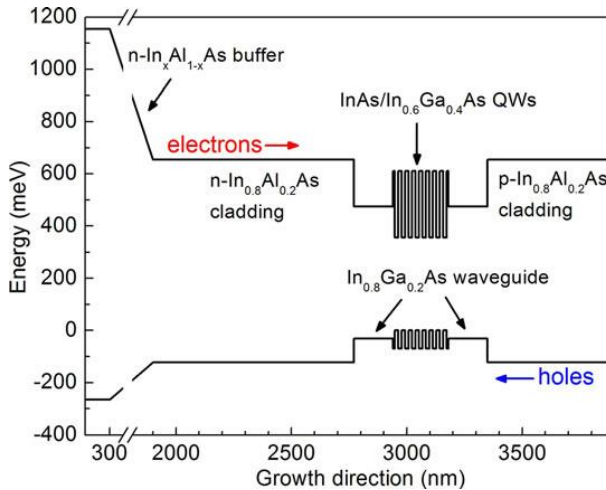


**Figure 2.2:** The energy-band structure of InP-based metamorphic type-I QW laser. The injection directions of electrons and holes are indicated. Adapted from [5].

In the case of QDs with around 10 nanometers in diameter, there is confinement in all three dimensions for the charge carriers. As a result, the electrons exhibit a discrete atomic-like energy spectrum, which comes from the quantum confinement. With the help of quantum confinement, the spacing between these discrete atomic-like states in small QDs is much larger than the available thermal energy. Thus the thermal depopulation of the lowest electronic states is inhibited. This effect can help to achieve a temperature insensitive optical gain, which is at an excitation level just above one electron-hole (e-h) pair per dot on average in the simple model of 2-fold degenerate band-edge

states. This advantage was expected to result in lasing performance superior to that of bulk semiconductors [6].

### 2.1.1 Colloidal quantum dot optical gain

An optically pumped colloidal QDs lasing device was first reported in 1991 with relatively large (around 10 nm) CdSe QDs. With this remarkable result, researchers realized lasing using epitaxial QDs under the optical and electrical pump in 1994 [7]. Further improvements have shown record-low lasing threshold (in terms of driving current) based on the epitaxial QDs [8-10]. A comparison of calculated maximum gain for bulk, 2D (film), 1D (wire) and 0D (box) gain materials is shown in Figure 2.3, from ref [6]. This result shows the potential of QDs based lasers to surpass quantum well and bulk lasers regarding the threshold current.

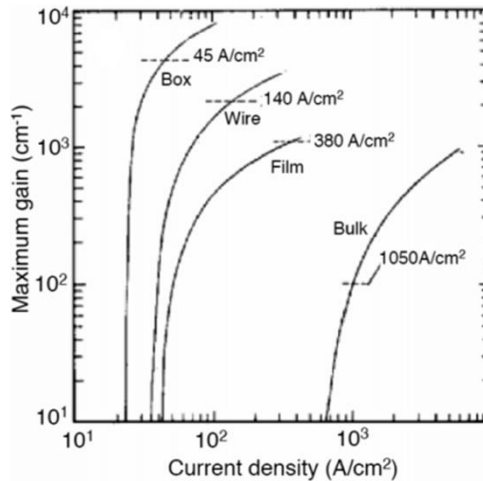


**Figure 2.3:** Calculated maximum gain as a function of injection current density for the GaAs/Ga<sub>0.8</sub>Al<sub>0.2</sub>As quantum box (i.e., QD), quantum wire, quantum film (i.e., quantum well), and bulk crystal (conventional double heterostructure). Dashed lines mark the lasing threshold for each material. Adapted from ref [6].

These benefits provided by quantum confinement give strong motivation to use colloidal QDs as the gain media for the lasing applications. In this quantum confinement regime, the electronic levels spacing can exceed hundreds of meV, as mentioned in the last section, which is considerably larger than the room temperature thermal energy (~24 meV). This unique feature can potentially guarantee superior temperature stability. Another additional feature coming with the quantum confinement is the prospect of wide range tunability regarding the

emission spectrum. In principle, the emission can be tuned in the order of 1 eV, achieving using a single material system through controlling the size of the colloidal QDs [11].

Nevertheless, after more than ten years of research, except for some reports of the existence of the optical gain [12-13], colloidal QDs failed to demonstrate lasing. Originally this failure was attributed to high non-radiative carrier losses due to trapping states at the colloidal QDs' surface, which comes from the large surface-to-volume ratio for these sub 10 nm particles. Another potential explanation considered was the greatly reduced electron-photon interactions efficiency in these small nano-particles [14-15]. The probability of phonon-assisted processes, which is required to fulfil the energy conservation for the electron-hole pairs to recombine, is dramatically reduced in these small nano-particles, compared with the case of quasi-continuous spectra of bulk materials. This phenomenon was believed to lead to a lower rate of carrier cooling by the help of phonon emission (known as the "phonon bottleneck"), which further leads to reduced PL efficiencies.

However, the effects related to carrier surface trapping and the "phonon bottleneck" turned out to be much less serious compared to the initially largely unforeseen problems of non-radiative Auger recombination [16].

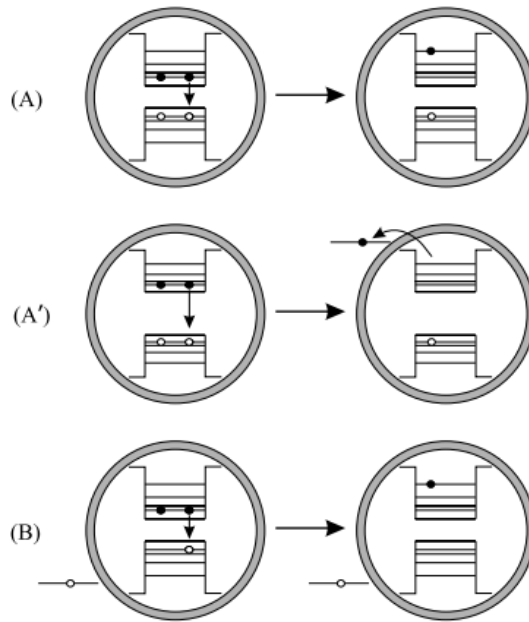


**Figure 2.4:** Scheme of Auger effects. (A) Auger relaxation effect of a biexciton into a neutral QD. The remaining excited carrier is in a higher state but still confined in the same neutral QD. (A') Auto-ionization effect of a neutral QD by Auger process. The electron is excited out of the QD. (B) Auger relaxation effect of a biexciton in an ionized QD. Adapted from ref [17].

As shown in Figure 2.4 [17], a rapid relaxation attributed to an Auger-type mechanism [18] was later found to be dominant in colloidal QDs. This relaxation is extremely fast compared with the radiative lifetime and happens on a picosecond to sub-picosecond time scale [19-21]. During this Auger relaxation, a hole can get the excess electron energy and fast relaxes through the valence band dense spectrum. Alternatively, the excess electron energy can ionize the QDs. All these fast Auger processes lead to the quenching of biexcitons or other multiexcitons, which are essential for achieving optical gain in most colloidal QDs.

### 2.1.2 Single exciton gain

As analyzed in the last section, the fast non-radiative Auger recombination quenching the biexcitons and multiexcitons is the main obstacle to realize lasing application using colloidal QDs. However, a practical approach to avoid the involvement of Auger recombination is achieving optical gain without the

existence of the biexcitons or multiexcitons at all, i.e., achieving optical gain using single excitons. This idea was triggered by the “giant” exciton-exciton repulsion from the type II hetero nanocrystals, in which the heterojunction of the core/shell structure band alignment has a staggering gap. This idea was first introduced and discussed in 2004 in reference [22]. In this paper, the authors described and analyzed the concept to realize single excitons optical gain with optimized core and shell dimensions to reach a type II band alignment. They also experimentally observed exciton-exciton repulsion, which can be seen from the ASE spectrum. Three years later, more detailed results for type-II CdTe/CdSe QDs with exciton-exciton repulsion energy up to  $\sim 30$  meV were reported [23]. ASE originating from single excitons was successfully demonstrated experimentally using specially designed type-II CdS/ZnSe QDs in 2007 [24].

The basic concept of single exciton optical gain is illustrated in Figure 2.5, with the existence of large exciton-exciton repulsion. The absorption and stimulated emission in the colloidal QD can be different with the absence (a) and the presence (b) of the exciton-exciton interaction. Without the presence of the exciton-exciton interaction, the single exciton cannot result in optical gain but only in optical transparency (Figure 2.5(a)), since the stimulated emission from the electron in the conduction band is exactly balanced by the absorption associated with the electron in the valence-band. With the existence of the exciton-exciton interaction, this balance can be broken. The presence of the first exciton can create an effective electric field, which leads to a Stark shift of the second exciton transition bandgap [24]. This exciton-exciton interaction, mainly coming from the effect of Coulomb interactions between excitons, can be negative or positive, which is depending on the sign of the exciton-exciton interaction energy ( $\Delta_{xx}$ ). This leads to a slight difference in terms of the transition bandgap between the single exciton and biexciton, and this modified transition bandgap can be expressed as:

$$E_{g,xx} = E_{g,x} + \Delta_{xx} \quad (2.1)$$

If the exciton-exciton has repulsion interaction,  $\Delta_{xx} > 0$  (Figure 2.5(b)), this shifts the absorbing transition upwards in energy, which can be beneficial for a lasing application. If the  $\Delta_{xx}$  is larger than the emission line width, the single optical gain can be achieved, without the involvement of biexcitons and multiexcitons. For standard core only and type-I thin-shell colloidal QDs, exciton-exciton attraction is the case ( $\Delta_{xx} < 0$ ), hence single exciton gain cannot be observed. For type-II heterostructure colloidal QDs, the electrons and holes are separated between the core and shell. With the existence of a biexciton, the electrons and holes are separated because of the band alignment. They have to share the same part of the colloidal QDs structure, and the repulsive interaction



Eq. 2.2 indicates that the optical gain can be achieved when  $P_x = 4/5$ , which also illustrates the threshold average QD occupancy:  $\langle N_g \rangle = P_x = 4/5$ . Since  $\langle N_g \rangle$  is less than 1, the lasing action can be obtained with only the existence of single excitons. From Eq. 2.2, we can also get the single exciton saturation gain is realized when  $P_x = 1$  and it is given by:

$$G_{0,x} = \frac{c \gamma}{n 2} n_{QD} \quad (2.3)$$

This equation indicates that  $G_{0,x}$  is about four times lower than the saturated biexciton gain (see section 2.1.2). However, single-exciton-gain has the advantage in term of a longer lifetime despite being smaller in magnitude. Its relaxation is controlled by fairly slow single-exciton recombination without the existence of the fast Auger lifetime. In reference [24], from experimental data, the lifetime of the single exciton gain was found to be considerably longer than the biexciton lifetime ( $\tau_x = 1.7 \text{ ns}$  versus  $\tau_{xx} = 210 \text{ ps}$ ). This single-exciton gain mechanism can help us to realize CW pump lasing because the threshold pump intensity scales as the inverse of the gain lifetime. It might be possible to reduce the CW lasing threshold by a factor of ca. 100–1000 (defined by the ratio of single exciton lifetime  $\tau_x$  and biexciton lifetime  $\tau_{xx}$ , see section 2.1.4), if we use the strategy for standard CdSe QDs. Nevertheless, in practice, it has been proven to be challenging to reach gain from type II colloidal QDs. The simplified model only considers a small broadening of the optical transition, which is usually not the case due to the size dispersion from the synthesis of the QDs. Furthermore, the type II band structure tends to push the holes to the shell and defects at the shell surface will quench the optical gain. Therefore, thus far, most work toward lasing in this thesis has focused on increasing the biexciton lifetime of type I CQDs to obtain biexciton gain, as discussed in the next section.

### 2.1.3 Biexciton gain

As already discussed in the previous section, biexciton gain is hampered by fast non-radiative Auger recombination [16]. To better analyze this problem, we will approximate the lowest-energy “emitting” transition in the QDs by a simple 2-fold, spin-degenerate, two-level system, as introduced in reference [24]. In the ground state of this system, two electrons stay in the valence band level with opposite spin direction (Figure 2.6 left). In the case one electron is pumped to the conduction band level; the single exciton state does not produce optical gain but optical transparency (Figure 2.6, middle). Biexcitons or higher order multiexcitons are needed to realize an optical gain in this circumstance, as illustrated in Figure 2.6 right. However, multiexcitons in colloidal QDs are subject to highly efficient Auger recombination, which depletes the optical gain quickly.

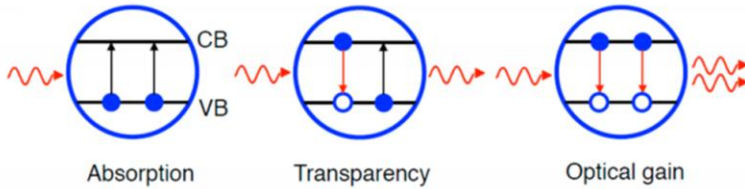


**Figure 2.6:** Simplified scheme for three different interaction regimes of a semiconductor colloidal QD with a photon resonant with the band-edge transition. It has a 2-fold spin-degenerate conduction-band (CB) and valence-band (VB) levels. Adapted from [24]

With the existence of fast Auger recombination, two factors were crucial for the first demonstrations of biexciton optical gain. One is using densely packed QD films, which have much larger gain coefficients. This was first realized in ref [27]. The high gain coefficients from the densely packed film help to out compete the Auger process loss. Another useful method, which is still widely used now to help to demonstrate and analyze optical amplification from colloidal QDs in the lab, is the use of femtosecond high power optical pulses to excite the colloidal QDs samples. The carrier losses due to Auger recombination can be minimized with this technique at the pump stage. Soon after the proof of principle, research groups were able to demonstrate lasing from colloidal QDs using different optical cavity designs [28-31]. In the remainder of this section, a more in-depth analysis of principles of colloidal QDs biexciton lasing with the presence of fast Auger recombination is provided (adapted from ref [32]).

To analyze optical gain and the lasing threshold for a given configuration, the simplified model from Figure 2.6 is updated to show the different degeneracies of the ground ( $|0\rangle$ ), single exciton ( $|X\rangle$ ), and biexciton ( $|XX\rangle$ ) states derived from the difference in their spin configurations, as illustrated in reference [32]. Figure 2.7(a) shows the modified model, where these three states are placed along a vertical “energy” axis. In the ground state  $|0\rangle$  in Figure 2.7(a), both valence-band spin sublevels are occupied with electrons; leads to a nondegenerate state. The biexciton state  $|XX\rangle$  is also nondegenerate as it contains two occupied conduct band spin sublevels. The single exciton state  $|X\rangle$ , on the other hand, is four fold degenerate due to the four different spin configurations, as illustrated in Figure 2.7(a). From the optical selection rules, we can derive only two of these configurations are optically active. In the model from reference [32], it is assumed that all of these configurations are in mutual thermal equilibrium, which means only half of the single excitons are optically active. With the above assumptions, we can express the per-dot rate of stimulated emission due to the transition from the single exciton to the ground state as:

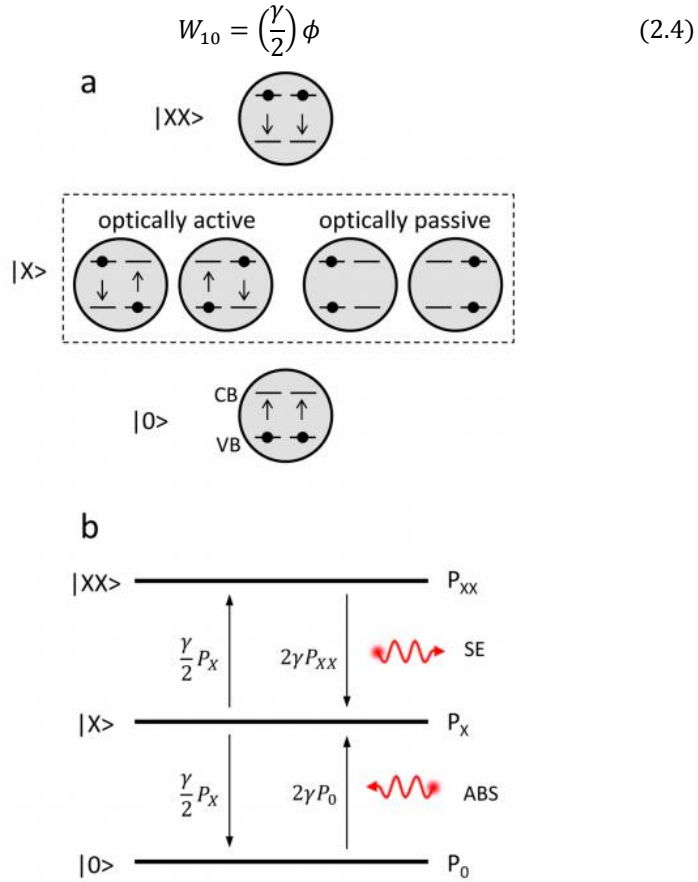


**Figure 2.7:** (a) The quasi-three-state model of optical gain in QDs, which comprises a nondegenerate ground state ( $|0\rangle$ , bottom), a four-fold degenerate single-exciton state, ( $|X\rangle$ , middle) and a nondegenerate biexciton state ( $|XX\rangle$ , top). (b) A quasi-three-level transition scheme with photon absorption (up arrows) and stimulated emission (down arrows). The rates of different transitions are indicated in the figure (per unit photon density);  $\gamma$  is the transition probability per single spin-allowed transition (shown by black arrows in panel a). Adapted from ref [32].

In Figure 2.7b, where  $\phi$  represents the density of photons accumulated in the optical cavity mode, and  $\gamma$  is a parameter proportional to the oscillator strength of the individual transition (shown by black arrows in Figure 2.7a), equivalent to the well-known Einstein coefficient of stimulated emission. The transition from the  $|X\rangle$  to the  $|XX\rangle$  state via absorption of a photon can be expressed as:

$$W_{12} = \left(\frac{\gamma}{2}\right)\phi \quad (2.5)$$

This equation implies that the single excitons provide zero net contribution for optical gain as we discussed in the previous section. Thus, the only source that can contribute to the optical gain in this system is stimulated emission by biexcitons ( $|XX\rangle - |X\rangle$  transition), which competes with photon losses from absorption due to the  $|0\rangle - |X\rangle$  transition (Figure 2.7b). For these two transitions, the per-dot rates are equal and can be expressed as follow:

$$W_{21} = W_{01} = 2\gamma\phi \quad (2.6)$$

From the above analysis, we can conclude the ratio for the emission rates by biexcitons and single excitons is 4 to 1 (Eq. 2.5 and Eq. 2.6), which is consistent with the quadratic scaling of radiative rates with exciton multiplicity typically observed for QDs of various compositions [33-35]. To characterize the behaviour of an excited QD with biexciton, we can restrict the probabilities  $P_0$  (the ground),  $P_x$  (single-exciton) and  $P_{xx}$  (biexciton) states by the condition:  $P_0 + P_x + P_{xx} = 1$ . In this case, the net rate of photon generation per unit volume equation can be expressed as:

$$r_{se} = n_{QD}(W_{21} - W_{01}) = 2\gamma n_{QD}(P_{xx} - P_0) \quad (2.7)$$

where  $n_{QD}$  is the concentration of the QDs in the sample. This leads to another equation for the gain coefficient:

$$G = \frac{c}{n} r_{se} = 2 \frac{c}{n} \gamma n_{QD} \rho = G_0 \rho \quad (2.8)$$

where  $c$  is the speed of light in vacuum,  $n$  is the index of the colloidal QD sample,  $\rho$  is the per QD population inversion, which can be expressed as:

$$\rho = P_{xx} - P_0 \quad (2.9)$$

$G_0$  is the saturated gain obtained for  $\rho = 1$ , and can be expressed as:

$$G_0 = 2 \frac{c}{n} \gamma n_{QD} \quad (2.10)$$

which corresponds to the complete population inversion when all QDs are in the biexciton states.

Using the concept introduced above, we can write down coupled colloidal QD-light-field kinetic equations as follow:

$$\frac{dP_0}{dt} = -2\gamma\phi P_0 + \frac{\gamma}{2}\phi P_x + \frac{P_x}{\tau_x} \quad (2.11)$$

$$\frac{dP_x}{dt} = -2\frac{\gamma}{2}\phi P_x + 2\gamma\phi P_0 + 2\gamma\phi P_{xx} - \frac{P_x}{\tau_x} + \frac{P_{xx}}{\tau_{xx}} \quad (2.12)$$

$$\frac{dP_{xx}}{dt} = -2\gamma\phi P_{xx} + \frac{\gamma}{2}\phi P_x - \frac{P_{xx}}{\tau_{xx}} \quad (2.13)$$

$$\frac{d\phi}{dt} = -2\gamma\phi n_{QD}(P_{xx} - P_0) - \frac{\phi}{\tau_c} \quad (2.14)$$

The time constants  $\tau_x$ ,  $\tau_{xx}$  and  $\tau_c$  are the single-exciton, biexciton, and the cavity photon lifetimes, respectively. The Eq. 2.14 only accounts the photons generated via stimulated emission and accumulate into the optical cavity mode. In principle, using a separate rate equation to account for photons produced by spontaneous emission is possible. However, we can disregard these photons since they do not accumulate in the optical cavity and they do not affect the carrier dynamics, which is a common approach when builds kinetic equations.

The average QD occupancy  $\langle N^* \rangle$  is limited to 2 in this three-state model. The average occupancy can be expressed as  $\langle N^* \rangle = P_x + 2P_{xx} = 1 + \rho$ . Here, we consider the situation of a Poisson distribution for the carrier populations across the colloidal QD ensemble, which is typically realized using short pulses to have the above band gap excitation of the sample [36]. In this case, the probability of having  $N$  excitons in a QD can be expressed as:

$$p_N = \langle N \rangle^N (N!)^{-1} e^{-\langle N \rangle} \quad (2.15)$$

where  $\langle N \rangle = \sum_{i=1}^{\infty} i p_i$  represents the average QD excitation occupancy [32]. In 2 fold degenerate emitting states QDs, the multiexciton contribution to the band edge optical gain is independent of its order and we can consider the same as a biexciton. As a result, the true average QD occupancy can be expressed as:

$$\langle N^* \rangle = 2 - e^{-\langle N \rangle} (2 + \langle N \rangle) \quad (2.16)$$

Here, by using Poisson probabilities in the expression for the optical gain onset ( $P_{xx} - P_0 = 0$ ,  $\langle N^* \rangle = 1$ ), we can obtain the true average occupancy for the gain threshold. This onset value can be found by solving the equation:

$$\langle N_g \rangle + 2 = e^{\langle N_g \rangle} \quad (2.17)$$

Where we can have  $\langle N_g \rangle \approx 1.15$ .

### 2.1.4 Biexciton lasing threshold analysis

From the analysis of the last section, we estimated that for pulsed pumping, the gain onset (threshold) is defined by the condition  $\langle N_g \rangle \sim 1.15$ . The corresponding gain onset threshold for the per pulse photon fluence ( $j_g$ ) can be simply estimated by  $\langle N_g \rangle = j_g \sigma \approx 1.15$  ( $\sigma$  is the QD's absorption cross section), which yields  $j_g \approx 1.15/\sigma$ .  $\sigma$  is at the order  $10^{-15} \text{ cm}^2$  for common CdSe colloidal QDs. We can estimate  $j_g$  is at the order of  $10^{15}$  photons per  $\text{cm}^2$ ,

which corresponds to a per pulse energy fluence  $w_g$ , of the order of 0.1-1 mJ/cm<sup>2</sup>, depending on the different excitation wavelength.

However, experimental studies show that the pump power densities are at the order of a few to a few hundreds of mJ/cm<sup>2</sup> for the ASE onset and the lasing regime for the standard colloidal QDs [24], which is much larger than the one derived from the above theoretical analysis. This is usually tributed to the existence of the fast Auger recombination from the QDs. To achieve ASE and lasing, the optical gain has to reach a higher value not only sufficient to compensate the optical losses in the cavity but also has to be sufficiently large enough to outcompete the Auger recombination.

For further use in chapter 4, we analyze the lasing threshold in case of CW excitation. To analyze the steady state situation, we add in Eq. 2.11-2.13 with the steady-state carrier generation term  $J\sigma$  (here  $J$  is the CW pumping intensity expressed in term of the photon flux). All the time derivatives have been set to zero [d(...)/dt = 0]. In the sub-threshold regime, we can assume there is no photon in the lasing cavity mode, hence  $\phi = 0$ . Under the conditions mentioned above, the kinetic Eq. 2.11-2.13 from the last section can be rewritten into:

$$\frac{P_x}{\tau_x} - J\sigma P_0 = 0 \quad (2.18)$$

$$J\sigma P_0 - \frac{P_x}{\tau_x} + \frac{P_{xx}}{\tau_{xx}} - J\sigma P_x = 0 \quad (2.19)$$

$$J\sigma P_x - \frac{P_{xx}}{\tau_{xx}} = 0 \quad (2.20)$$

To link  $P_0$ ,  $P_x$ ,  $P_{xx}$  we add also:

$$P_0 + P_x + P_{xx} = 1 \quad (2.21)$$

Then we can derive:

$$P_x = \frac{J\sigma\tau_x\tau_{xx}}{1 + J\sigma\tau_x + (J\sigma)^2\tau_x\tau_{xx}} \quad (2.22)$$

$$P_{xx} = \frac{(J\sigma)^2\tau_x\tau_{xx}}{1 + J\sigma\tau_x + (J\sigma)^2\tau_x\tau_{xx}} \quad (2.23)$$

Since we have:

$$\langle N^* \rangle = 0 \cdot P_0 + 1 \cdot P_x + 2 \cdot P_{xx} \quad (2.24)$$

By using Eq. 2.22 and Eq. 2.23, we can rewrite Eq. 2.24 and find the CW excitation relation:

$$\langle N^* \rangle = \frac{J\sigma\tau_x + 2(J\sigma)^2\tau_x\tau_{xx}}{1 + J\sigma\tau_x + (J\sigma)^2\tau_x\tau_{xx}} \quad (2.25)$$

Using this expression, we can link the QD occupancy  $\langle N^* \rangle$  with the CW pumping flux. To further investigate the influence of Auger recombination (or Auger lifetime) to the CW pumping lasing threshold, we will make some reasonable assumptions and plot the lasing threshold pumping flux  $J_{las}$  as a function of the biexciton lifetime  $\tau_{xx}$  (Fig. 2.8).

We thereby assume the single exciton lifetime is purely radiative, leading to  $\tau_x = \tau_{r,x}$ . The biexciton decay is the combination result with both radiative recombination ( $\tau_{r,xx}$ ) and the nonradiative Auger process ( $\tau_{A,xx}$ ). The overall biexciton lifetime can be expressed using equation [32]:

$$\tau_{xx} = \frac{\tau_{r,xx}\tau_{A,xx}}{\tau_{r,xx} + \tau_{A,xx}} \quad (2.26)$$

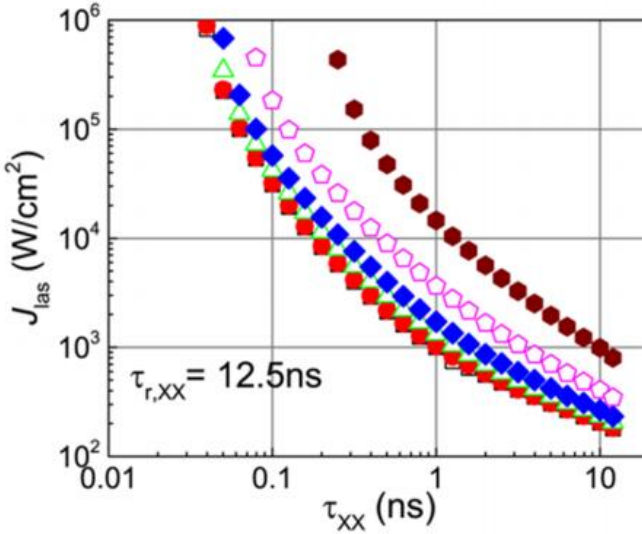


**Figure 2.8:** The plot of the CW lasing threshold  $J_{las}$  as a function of  $\tau_{xx}$ . The different colors indicate different cavity photon lifetime:  $\tau_c = 1$  ns (black squares), 0.1 ns (red circles), 0.01 ns (green triangles), 0.005 ns (blue diamonds), 0.002 ns (magenta pentagons), and 0.001 ns (brown hexagons). The pump wavelength is 400 nm. Adapted from ref [32].

Here, we assume that the radiative rate exhibits a quadratic scaling with exciton multiplicity, which yields  $\tau_{r,xx} = \tau_x/4 = \tau_{r,x}/4$  [32]. In the plot, we assume the absorption cross section  $\sigma$  of the colloidal QDs to be  $10^{-15}$  cm<sup>2</sup>. The single exciton lifetime  $\tau_x = \tau_{r,x} = 50$  ns, the biexciton radiative lifetime to be  $\tau_{r,xx} = 12.5$  ns [32]. By using the assumed numbers above, with Eq. 2.25, we can have plot the CW lasing threshold  $J_{las}$  as a function of  $\tau_{xx}$  with different cavity photon lifetime, which is adapted from ref [32].

From the plot, we can observe a rapid increase in the threshold intensity with a decreasing biexciton lifetime. The incensement of  $J_{las}$  is not that much in the large value region of the biexciton lifetime (1-10 ns). But as the biexciton lifetime becomes smaller, in the small value region (<1 ns), where the Auger recombination process kicks in and dominates, the  $J_{las}$  becomes progressively steeper. For example, in the case of an ideal optical cavity with low optical cavity loss ( $\tau_c = 1$  ns, black squares in the plot), the change of  $\tau_{xx}$  from 1 ns to 50 ps results in a 3 orders of magnitude increase of  $J_{las}$  from around  $10^3$  W/cm<sup>2</sup> to  $10^6$  W/cm<sup>2</sup>. It is obvious that to achieve a CW lasing with a  $\tau_{xx} = 50$  ps biexciton lifetime is practically not possible due to the very high pumping intensity of  $10^6$  W/cm<sup>2</sup>. On the other hand, a suppressed Auger process, which leads to a longer biexciton lifetime, might make CW lasing from a colloidal QDs device possible.

Because Auger lifetime scales in direct proportion to the QDs volume, the use of larger QDs is expected to lower the lasing threshold. Experimental results indicate that using large volume QDs can indeed help to suppress the Auger process, as shown for example for thick-shell “giant” CdS/CdSe QDs or large-size nonspherical nanostructures such as nanorods [37, 38], tetrapods [39], or nanoplatelets [40]. Another way to suppress the Auger process is to use alloyed interface core-shell QDs. These types of QDs have grading and smoothing of the confinement potential, which reduces the intraband transition involved in Auger recombination [32].

Microsecond-sustained lasing from colloidal QDs was first reported in [41]. In this paper, the authors employed inorganic-halide-capped QDs exhibit high modal gain. With the help of this inorganic halide and a thermally conductive MgF<sub>2</sub> substrate, they have managed to reduce the heating problem and have demonstrated lasing with pump pulse duration of 0.4  $\mu$ s and peak power of  $\sim 50$  kW/cm<sup>2</sup> @ 355 nm. More recent work from the same group has demonstrated a CW pumped laser using colloidal QDs [42]. In this work, they have used biaxially strained colloidal QDs. These QDs have further suppressed Auger recombination, which can be better for low threshold lasing as derived above. Combined with better thermal management, they have demonstrated a photonics crystal distributed feedback (PhC-DFB) type laser CW lasing with a threshold  $\sim 8$  kW/cm<sup>2</sup> @ 441 nm.

In our work, we used so-called *flash*- CdSe/CdS QDs, which are synthesized using a seeded growth approach that yields thick shell CdSe/CdS QDs in a fast and simple process [43]. Such QDs feature an alloyed CdSe/CdS interface, which helps to reduce strain and slow down non-radiative Auger recombination of multi-excitons. This Auger process suppression will be helpful for the lasing applications as shown in chapter 4.

## 2.2 Colloidal quantum dots as single photon emitters

The progress of the last decades in miniaturization of electronic components allowed reducing the size of, e.g. central processing units (CPUs) while increasing at the same time its computational power. However, quantum mechanics tells us that there is a limitation to further decreasing the size of the transistors, the tiny “cell” from which the CPU is built up. Therefore, a different kind of hardware strategy has become more interesting: a machine that exploits quantum theory more directly, to simulate nature, as suggested by Prof. R.P. Feynman. This is the purpose of quantum computation and quantum communication, aiming to use the principle of quantum mechanics to manipulate and exchange information between parties. The main advantage of quantum computation is the introduction of the superposition principle, which allows the introduction of the concept of a qubit.

A single photon source is a key component to realize qubits for quantum computation and quantum communication. Here, the second-order intensity correlation function is generally used to determine the quality of a single photon source [44]:

$$g^{(2)}(\tau) = \frac{\langle I(t)I(t + \tau) \rangle}{\langle I(t) \rangle^2} \quad (2.27)$$

Here the  $I(t)$  represents the light intensity at time  $t$ , where  $\langle \cdot \rangle$  represents the time average. From an experimental point of view, we can also use the number of counts  $n(t)$  registered to a photon counting detector to represent the beam intensity, since  $n(t)$  is proportional to the intensity of the impinging beam  $I(t)$ . Hence, Eq. 2.27 can be rewritten as [44]:

$$g^{(2)}(\tau) = \frac{\langle n(t)n(t + \tau) \rangle}{\langle n(t) \rangle^2} \quad (2.28)$$

We can consider  $g^{(2)}(\tau)$  as a quantitative answer to the following question: If one has already detected a photon at time  $t$ , what is the probability to detect another photon at time  $t + \tau$ ? Or more generally, if one has detected  $n$  photons at time  $t$ , what is the probability to detect another  $n$  photons at time  $t + \tau$  [45]?

For coherent light, e.g. the beam from a laser source, the number of photon in the laser beam per time duration is proportional to the intensity of the laser beam. The intensity of a laser output beam is usually a constant. The number of counts at times  $t$  and  $t + \tau$  should be the same, hence  $g^{(2)}(\tau) = 1$  for any  $\tau$  [45].

A very important value is  $g^{(2)}(0)$ . This function answers this question: how often one can detect two photons at times very close to each other? Or what is the possibility to detect 2 photons at one time. This  $g^{(2)}(0)$  value gives the probability of multiphoton emission events. For coherent light, like a laser, as we analyzed above,  $g^{(2)}(0) = 1$ . For classical sources, like chaotic light, the

beam has intensity fluctuations and therefore a tendency to detect multiphoton events [45]. This leads to a result of  $g^{(2)}(0) > 1$ . It can be shown that for classical light sources always have  $g^{(2)}(0) \geq g^{(2)}(\tau) \geq 1$  [45]. That means the antibunched light is not possible for this kind of light sources.

But for quantum emitters, like single photon sources, antibunched light can be generated. The single photon source should emit individual photons at intervals [46]. A solitary quantum emitter is usually used to generate the single photon. Theoretically, there are lots of options, e.g. a trapped atom or ion, a nitrogen-vacancy center or a QD [46]. The deterministic emission from the single photon source is usually triggered by periodic electronic or optical excitation to obtain outputs [46]. A highly efficient polarized emission from the single photon source which can be coupled to a well-defined spatial optical mode is also desired for ideal emitters [46].

For an ideal single photon source,  $g^{(2)}(0) = 0$ , which is greatly reduced in comparison to classical light sources and coherent light sources. For practical quantum computation and quantum communication use, indistinguishable single photons are preferred. The indistinguishableness means that there is no dephasing between the emitted photons. This can be determined by evaluating the quantity  $2\tau_s/\tau_c$  [46]. Here  $\tau_c$  is the coherence time, which can be measured via the coherence length  $l_c$ .  $\tau_s$  is the source emitter's lifetime. No dephasing of the emitted photons for ideal single photon sources, hence results in  $2\tau_s/\tau_c = 1$ , meaning that the emitted photons from the source are fully indistinguishable. This can be quantified further through the two photon quantum interference measurement [46].

To check the quality of the single photon emission, an anti-bunching measurement is performed, using a so-called Hanbury Brown-Twiss set-up. The schematic diagram of the setup is shown in Figure 2.9(a) [47]. The incoming signals are split into two beams with a 50/50 beam splitter. There are two sensitive single-photon detectors to capture these two beams. The outputs of the detectors are connected to a Time-Correlated Single Photon Counting (TCSPC) unit. The TCSPC unit will repeatedly measure the signals from the two detector and show the time correlated data. The anti-bunched measurement can be performed with pulsed or CW excitation. Under the pulsed excitation, the typical time-correlated result from an anti-bunched source shows the individual pulses spaced by the excitation pulse period. The data will have a reduced or missing pulse at the correlation time difference of zero corresponding with different  $g^{(2)}(0)$  values of the single photon source. Under CW excitation, the typical time-correlated result from an anti-bunched source shows a flat line at none zero region. There should be a notable "intensity dip" at the time difference of zero. Figure 2.9(b) shows the correlation amplitude measurement of a single photon source with CW (blue) and pulsed (red) excitation [47]. To

time tag the absolute arrival time of all the detected photons is another way to characterize the anti-bunching signal, which needs complicated correlation algorithm to realize that. This approach is not commonly used in the applications [47].

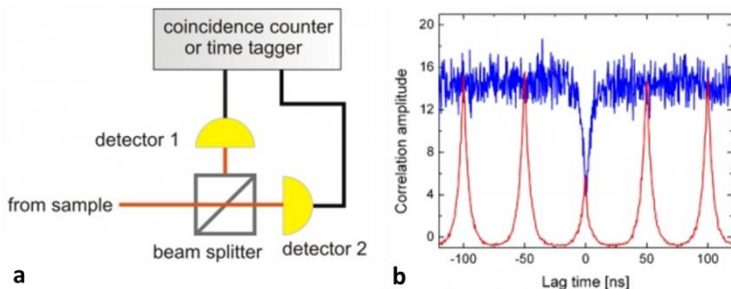


**Figure 2.9:** Hanbury Brown-Twiss interferometer set-up. (a) The schematic of the setup. (b) The correlation amplitude measurement results of a single photon source by using the Hanbury Brown-Twiss interferometer set-up. The blue curve is the result of CW excitation; the red curve is the result of pulsed excitation. Adapted from ref [47]

Colloidal QDs and other nanocrystals [48] as quantum emitters provide potential as a single photon emitter. As already extensively introduced above, colloidal QDs synthesis makes it possible to not only tune the emission wavelength by controlling their size but also offers extensive control over the QD size, shape, compound and even allows to realize complex heterostructures. The experimental room temperature photon anti-bunching results with single CdSe/ZnS core-shell QDs was first reported for [49-50]. This experimental result can be attributed to the highly efficient, non-radiative Auger recombination of multi-excitons as we discussed in Chapter 2.1.1. Figure 2.9 shows the result from reference [49] and from that we can clearly see an anti-bunched signal with CW excitation from a CdSe/ZnS single quantum dot. This result is quite different from the result obtained for a CdSe/ZnS cluster. This enabled the emission of a single photon to be triggered optically by a high-intensity excitation optical pulse [51, 52]. However, the early research also has shown that colloidal QDs have blinking issues which leads to an unpredictable variation of bright and dark periods [49-51]. But the recent improvement of the synthesis of colloidal QDs can suppress the blinking issue and further improve the colloidal QDs' potentials to act as a single photon source.

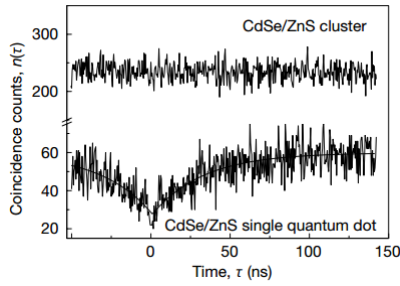


**Figure 2.10:** Measured distribution  $n(\tau)$  of photon pair separation times  $\tau$  for a CdSe/ZnS cluster and a single quantum dot. The line represents a fit to an exponential law. Adapted from ref [50].

However, for all the previous proof of principle research work, the characterization of the single photon sources based on colloidal QDs is usually done by spin coating a diluted solution onto a glass substrate [49-50]. The QDs are randomly located on the glass substrate. Also, most of the emission from the single QDs couple to free space and can only be collected with a microscopy system.

In my thesis, I will investigate the possibility to realize on-chip single photon sources based on colloidal QDs. A SiN waveguide platform is optimized. We will show the colloidal QDs can be embedded into the SiN layer stacks without quenching their photoluminescence. We also show the photon emission from these embedded colloidal QDs can be well coupled in a waveguide. With the help of the waveguide platform, more complicated functionalities can be potentially supported to confine, guide, modulate and detect these single photons. Thus, more complicated quantum information processing might be possible.

## References

- [1] Hall, Robert N., Gunther E. Fenner, J. D. Kingsley, T. J. Soltys, and R. O. Carlson. "Coherent light emission from GaAs junctions." *Physical Review Letters* 9, no. 9 (1962): 366.
- [2] Nathan, Marshall I., William P. Dumke, Gerald Burns, Frederick H. Dill Jr, and Gordon Lasher. "Stimulated emission of radiation from GaAs p-n junctions." *Applied Physics Letters* 1, no. 3 (1962): 62-64.
- [3] Arakawa, Y., and Hiroyuki Sakaki. "Multidimensional quantum well laser and temperature dependence of its threshold current." *Applied Physics Letters* 40, no. 11 (1982): 939-941.
- [4] [https://en.wikipedia.org/wiki/Laser\\_diode](https://en.wikipedia.org/wiki/Laser_diode)
- [5] Gu, Y., Y. G. Zhang, Y. J. Ma, L. Zhou, X. Y. Chen, S. P. Xi, and B. Du. "InP-based type-I quantum well lasers up to 2.9  $\mu$  m at 230 K in pulsed mode on a metamorphic buffer." *Applied Physics Letters* 106, no. 12 (2015): 121102.
- [6] Asada, Mashiro, Yasuyuki Miyamoto, and Yasuharu Suematsu. "Gain and the threshold of three-dimensional quantum-box lasers." *IEEE Journal of quantum electronics* 22, no. 9 (1986): 1915-1921.
- [7] Vandyshev, Yu V., V. S. Dneprovskii, V. I. Klimov, and D. K. Okorokov. "Lasing on a transition between quantum-well levels in a quantum dot." *Jetp Lett* 54, no. 8 (1991): 442.
- [8] Ledentsov, N. N., V. M. Ustinov, A. Yu Egorov, A. E. Zhukov, M. V. Maksimov, I. G. Tabatadze, and P. S. Kop'ev. "Optical properties of heterostructures with InGaAs-GaAs quantum clusters." *Semiconductors* 28, no. 8 (1994): 832-834.
- [9] Kirstaedter, N., N. N. Ledentsov, M. Grundmann, D. Bimberg, V. M. Ustinov, S. S. Ruvimov, M. V. Maximov et al. "Low threshold, large T/sub o/injection laser emission from (InGa) As quantum dots." *Electronics Letters* 30, no. 17 (1994): 1416-1417.
- [10] Grundmann, Marius. "The present status of quantum dot lasers." *Physica E: Low-dimensional Systems and Nanostructures* 5, no. 3 (1999): 167-184.
- [11] Michalet, X., F. F. Pinaud, L. A. Bentolila, J. M. Tsay, S. J. J. L. Doose, J. J. Li, G. Sundaresan, A. M. Wu, S. S. Gambhir, and S. Weiss. "Quantum dots for live cells, in vivo imaging, and diagnostics." *science* 307, no. 5709 (2005): 538-544.

- [12] Butty, J., Y. Z. Hu, N. Peyghambarian, Y. H. Kao, and J. D. Mackenzie. "Quasicontinuous gain in sol - gel derived CdS quantum dots." *Applied physics letters* 67, no. 18 (1995): 2672-2674.
- [13] Gindele, F., R. Westphäling, U. Woggon, L. Spanhel, and V. Ptatschek. "Optical gain and high quantum efficiency of matrix-free, closely packed CdSe quantum dots." *Applied physics letters* 71, no. 15 (1997): 2181-2183.
- [14] Benisty, H., C. M. Sotomayor-Torres, and C. Weisbuch. "Intrinsic mechanism for the poor luminescence properties of quantum-box systems." *Physical Review B* 44, no. 19 (1991): 10945.
- [15] Inoshita, Takeshi, and Hiroyuki Sakaki. "Electron relaxation in a quantum dot: Significance of multiphonon processes." *Physical Review B* 46, no. 11 (1992): 7260.
- [16] Klimov, Victor I., Alexander A. Mikhailovsky, D. W. McBranch, Catherine A. Leatherdale, and Mounqi G. Bawendi. "Quantization of multiparticle Auger rates in semiconductor quantum dots." *Science* 287, no. 5455 (2000): 1011-1013.
- [17] Brokmann, X., G. Messin, P. Desbiolles, E. Giacobino, M. Dahan, and J. P. Hermier. "Colloidal CdSe/ZnS quantum dots as single-photon sources." *New Journal of Physics* 6, no. 1 (2004): 99.
- [18] Efros, Al L., V. A. Kharchenko, and M. Rosen. "Breaking the phonon bottleneck in nanometer quantum dots: Role of Auger-like processes." *Solid State Communications* 93, no. 4 (1995): 281-284
- [19] Hendry, Euan, Mattijs Koeberg, Fengfeng Wang, H. Zhang, C. de Mello Donega, D. Vanmaekelbergh, and Mischa Bonn. "Direct observation of electron-to-hole energy transfer in CdSe quantum dots." *Physical review letters* 96, no. 5 (2006): 057408.
- [20] Guyot-Sionnest, Philippe, Moonsub Shim, Chris Matranga, and Margaret Hines. "Intraband relaxation in CdSe quantum dots." *Physical Review B* 60, no. 4 (1999): R2181.
- [21] Klimov, V. I., A. A. Mikhailovsky, D. W. McBranch, C. A. Leatherdale, and M. G. Bawendi. "Mechanisms for intraband energy relaxation in semiconductor quantum dots: The role of electron-hole interactions." *Physical Review B* 61, no. 20 (2000): R13349.
- [22] Ivanov, Sergei A., Jagjit Nanda, Andrei Piryatinski, Marc Achermann, Laurent P. Balet, Ilia V. Bezel, Polina O. Anikeeva, Sergei Tretiak, and Victor I. Klimov. "Light amplification using inverted core/shell

- nanocrystals: towards lasing in the single-exciton regime." *The Journal of Physical Chemistry B* 108, no. 30 (2004): 10625-10630.
- [23] Oron, Dan, Miri Kazes, and Uri Banin. "Multiexcitons in type-II colloidal semiconductor quantum dots." *Physical Review B* 75, no. 3 (2007): 035330.
- [24] Klimov, Victor I., Sergei A. Ivanov, Jagjit Nanda, Marc Achermann, Ilya Bezel, John A. McGuire, and Andrei Piryatinski. "Single-exciton optical gain in semiconductor nanocrystals." *Nature* 447, no. 7143 (2007): 441.
- [25] Piryatinski, Andrei, Sergei A. Ivanov, Sergei Tretiak, and Victor I. Klimov. "Effect of quantum and dielectric confinement on the exciton– exciton interaction energy in type II core/shell semiconductor nanocrystals." *Nano letters* 7, no. 1 (2007): 108-115.
- [26] Nanda, Jagjit, Sergei A. Ivanov, Marc Achermann, Ilya Bezel, Andrei Piryatinski, and Victor I. Klimov. "Light Amplification in the Single-Exciton Regime Using Exciton– Exciton Repulsion in Type-II Nanocrystal Quantum Dots." *The Journal of Physical Chemistry C* 111, no. 42 (2007): 15382-15390.
- [27] Klimov, V. I., A. A. Mikhailovsky, Su Xu, A. Malko, J. A. Hollingsworth, C. A. Leatherdale, H-J. Eisler, and M. G. Bawendi. "Optical gain and stimulated emission in nanocrystal quantum dots." *Science* 290, no. 5490 (2000): 314-317.
- [28] Klimov, Victor I., and Mounqi G. Bawendi. "Ultrafast carrier dynamics, optical amplification, and lasing in nanocrystal quantum dots." *Mrs Bulletin* 26, no. 12 (2001): 998-1004.
- [29] Eisler, Hans-Jürgen, Vikram C. Sundar, Mounqi G. Bawendi, Michael Walsh, Henry I. Smith, and Victor Klimov. "Color-selective semiconductor nanocrystal laser." *Applied physics letters* 80, no. 24 (2002): 4614-4616.
- [30] Kazes, Miri, David Y. Lewis, Yuval Ebenstein, Taleb Mokari, and Uri Banin. "Lasing from semiconductor quantum rods in a cylindrical microcavity." *Advanced Materials* 14, no. 4 (2002): 317-321.
- [31] Malko, A. V., A. A. Mikhailovsky, M. A. Petruska, J. A. Hollingsworth, H. Htoon, M. G. Bawendi, and V. I. Klimov. "From amplified spontaneous emission to microring lasing using nanocrystal quantum dot solids." *Applied physics letters* 81, no. 7 (2002): 1303-1305.
- [32] Park, Young-Shin, Wan Ki Bae, Thomas Baker, Jaehoon Lim, and Victor I. Klimov. "Effect of Auger recombination on lasing in heterostructured quantum dots with engineered core/shell interfaces." *Nano letters* 15, no. 11 (2015): 7319-7328.

- [33] Lee, Jinwook, Vikram C. Sundar, Jason R. Heine, Mounji G. Bawendi, and Klavs F. Jensen. "Full color emission from II–VI semiconductor quantum dot–polymer composites." *Advanced Materials* 12, no. 15 (2000): 1102-1105.
- [34] McGuire, John A., Jin Joo, Jeffrey M. Pietryga, Richard D. Schaller, and Victor I. Klimov. "New aspects of carrier multiplication in semiconductor nanocrystals." *Accounts of chemical research* 41, no. 12 (2008): 1810-1819.
- [35] Htoon, Han, Anton V. Malko, D. Bussian, Javier Vela, Yongfen Chen, Jennifer A. Hollingsworth, and Victor I. Klimov. "Highly emissive multiexcitons in steady-state photoluminescence of individual "giant" CdSe/CdS core/shell nanocrystals." *Nano letters* 10, no. 7 (2010): 2401-2407.
- [36] Klimov, Victor I. "Optical nonlinearities and ultrafast carrier dynamics in semiconductor nanocrystals." (2000): *J. Phys. Chem. B* 2000, 104, 6112-6123.
- [37] Htoon, Han, Jennifer A. Hollingsworth, A. V. Malko, R. Dickerson, and Victor I. Klimov. "Zero-to one-dimensional transition and Auger recombination in semiconductor quantum rods." In *Quantum Electronics and Laser Science Conference*, p. QTuA4. Optical Society of America, 2003.
- [38] Htoon, H., J. A. Hollingsworth, A. V. Malko, R. Dickerson, and V. I. Klimov. "Light amplification in semiconductor nanocrystals: Quantum rods versus quantum dots." *Applied physics letters* 82, no. 26 (2003): 4776-4778.
- [39] Liao, Yile, Guichuan Xing, Nimai Mishra, Tze Chien Sum, and Yinthai Chan. "Low Threshold, Amplified Spontaneous Emission from Core - Seeded Semiconductor Nanotetrapods Incorporated into a Sol–Gel Matrix." *Advanced Materials* 24, no. 23 (2012).
- [40] She, Chunxing, Igor Fedin, Dmitriy S. Dolzhenkov, Arnaud Demortière, Richard D. Schaller, Matthew Pelton, and Dmitri V. Talapin. "Low-threshold stimulated emission using colloidal quantum wells." *Nano letters* 14, no. 5 (2014): 2772-2777.
- [41] Adachi, Michael M., Fengjia Fan, Daniel P. Sellan, Sjoerd Hoogland, Oleksandr Voznyy, Arjan J. Houtepen, Kevin D. Parrish, Pongsakorn Kanjanaboos, Jonathan A. Malen, and Edward H. Sargent. "Microsecond-sustained lasing from colloidal quantum dot solids." *Nature communications* 6 (2015): 8694.

- [42] Fan, Fengjia, Oleksandr Voznyy, Randy P. Sabatini, Kristopher T. Bicanic, Michael M. Adachi, James R. McBride, Kemar R. Reid et al. "Continuous-wave lasing in colloidal quantum dot solids enabled by facet-selective epitaxy." *Nature* (2017).
- [43] Cirillo, Marco, Tangi Aubert, Raquel Gomes, Rik Van Deun, Philippe Emplit, Amelie Biermann, Holger Lange, Christian Thomsen, Edouard Brainis, and Zeger Hens. "'Flash' Synthesis of CdSe/CdS Core-Shell Quantum Dots." *Chemistry of materials* 26, no. 2 (2014): 1154-1160.
- [44] Fox, Mark. *Quantum optics: an introduction*. Vol. 15. OUP Oxford, 2006.
- [45] <https://physics.stackexchange.com/questions/139833/what-does-g2-signify-in-quantum-optics-and-how-to-calculate-it>
- [46] Chunnillal, Christopher J., Ivo Pietro Degiovanni, Stefan Kück, Ingmar Müller, and Alastair G. Sinclair. "Metrology of single-photon sources and detectors: a review." *Optical Engineering* 53, no. 8 (2014): 081910-081910.
- [47] <https://www.picoquant.com/applications/category/metrology/antibunching>
- [48] Becker, Michael A., Roman Vaxenburg, Georgian Nedelcu, Peter C. Sercel, Andrew Shabaev, Michael J. Mehl, John G. Michopoulos et al. "Bright triplet excitons in caesium lead halide perovskites." *Nature* 553, no. 7687 (2018): 189.
- [49] Michler, P., A. Imamoglu, M. D. Mason, and P. J. Carlson. "Quantum correlation among photons from a single quantum dot at room temperature." *Nature* 406, no. 6799 (2000): 968.
- [50] Lounis, B., H. A. Bechtel, D. Gerion, P. Alivisatos, and W. E. Moerner. "Photon antibunching in single CdSe/ZnS quantum dot fluorescence." *Chemical Physics Letters* 329, no. 5 (2000): 399-404.
- [51] Brokmann, Xavier, E. Giacobino, Maxime Dahan, and Jean-Pierre Hermier. "Highly efficient triggered emission of single photons by colloidal CdSe/ZnS nanocrystals." *Applied Physics Letters* 85, no. 5 (2004): 712-714.
- [52] Brokmann, X., G. Messin, P. Desbiolles, E. Giacobino, M. Dahan, and J. P. Hermier. "Colloidal CdSe/ZnS quantum dots as single-photon sources." *New Journal of Physics* 6, no. 1 (2004): 99.

# 3

## **Silicon nitride platform optimization for colloidal quantum dots integration**

SiN is a commonly used material in CMOS foundries for masking, passivation and strain engineering. The crystalline SiN is a dielectric material with a large band gap around 5 eV [1], hence has a large transparency window from visible to the infrared (0.4  $\mu\text{m}$  to 4  $\mu\text{m}$ ). It has an optical index intermediate between that of silicon and silicon oxide ( $\sim 2.0$ ) [2], resulting in a much more compact footprint of the integrated circuits compared with the silicon oxide waveguide platform and less waveguide loss compared with the silicon waveguide platform. As it has been already widely used in the CMOS technology, SiN potentially allows for large-scale integration and hence a cost-efficient photonics integration platform [3].

The SOI technology that is widely used for the silicon photonics integration platform uses wafers containing a thin layer of crystalline silicon, which is separated from the silicon substrate by a buried oxide. However, the SiN layers used in the SiN photonics integration platform are not crystalline SiN but generally deposited using two types of technologies. One is called low-pressure chemical vapor deposition (LPCVD) [5]; the other one is called plasma enhanced chemical vapor deposition (PECVD) [6]. Both technologies can

provide amorphous SiN layers on top of substrates. By tuning the ratio of the deposition gas, the index of the layer can be tuned over the range 1.8-2.2. While,  $n > 2.0$  indicates a silicon-rich film,  $n < 2.0$  usually indicates an abundance of nitride [4-6]. LPCVD, allows depositing nearly stoichiometric nitride ( $\text{Si}_3\text{N}_4$ ) with very high purity, which leads to very low optical material loss. However, the LPCVD SiN deposition needs a high temperature ( $\sim 700\text{-}900\text{ }^\circ\text{C}$ ) and a low pressure chamber which leads to a slow deposition rate at the order of  $\text{\AA}/\text{sec}$  [5]. LPCVD SiN films typically also have high tensile stress, which leads to a limitation of the maximum film thickness around 400 nm before the deposited SiN layer cracks. Both properties limit the applications of LPCVD SiN layers. PECVD SiN, on the other hand, provides flexibility compared with LPCVD SiN. PECVD deposition can be performed at quite a low temperature (below  $500\text{ }^\circ\text{C}$  even at room temperature). The much higher deposition rate and less severe stress in the layer makes it possible to obtain large film thickness (up to  $1\text{ }\mu\text{m}$ ) in a single run [4].

Since the SiN layers are generally prepared with chemical vapor based deposition, the layer usually contains hydrogen bonds (Si-H; N-H), which lead to considerable absorption in the infrared. The high loss around 1520 nm has been experimentally demonstrated, and the results have been shown in reference [6-7]. The SiN prepared by PECVD at relatively low temperatures has much severer optical loss around 1550 nm. This loss is the result of the much higher concentration of the hydrogen in the SiN layer, which is over one order of magnitude than the LPCVD SiN. This limits the applications for PECVD SiN in the telecom wavelength range. The hydrogen content can be minimized by optimizing the deposition conditions [6-11]. The annealing process with a high temperature (above  $1000\text{ }^\circ\text{C}$ ) can further reduce the material loss around 1550 nm, which has been demonstrated from [12-13].

The early work exploiting SiN as a material for optical waveguide focused on using it as in the visible wavelength range. The work demonstrated losses around 0.1 dB/cm for LPCVD SiN [14, 15] and 1.14 dB/cm for PECVD SiN [16] with slab waveguides geometry at 632.8 nm on a Si wafer with buffered  $\text{SiO}_2$  in between. SiN waveguide platform has advantages compares with traditional  $\text{SiO}_2$  PICs and Si waveguide platform hence received growing attention in the recent years. It has been demonstrated in the telecom wavelength range, low loss SiN waveguide platforms with a multi-layer SiN core [17] or buried in a thick oxide cladding [18], with optical loss around 0.1 dB/cm at 1550 nm. A world record optical waveguide loss with low-confinement waveguides based on SiN material has been reported with TriPleX<sup>TM</sup> technology [19]. The state-of-the-art waveguide losses of  $\sim 0.003\text{ dB/cm}$  @ 1300nm and  $\sim 0.008\text{ dB/cm}$  @ 1540 nm were reported using this technology [19, 20]. Passive photonics components based on the SiN platform have been developed. SiN Arrayed

Waveguide Gratings (AWGs) with very low insertion loss of  $\sim 0.2\text{-}0.5$  dB are reported [21]. High optical Q micro-resonators achieved using SiN platform have also been demonstrated [22]. Applications like on-chip Raman spectroscopy [23] and biosensors [24] based on the SiN integration platform have been studied and demonstrated within the NIR and visible wavelength ranges. A variety of fundamental studies and applications like nonlinear optics [25-28], optomechanics [29-30] based on SiN photonics have also been undertaken.

As mentioned in Chapter 1, like silicon, SiN is also not an efficient material for light generation. Our goal in this thesis is to use the heterogeneous integration idea to combine the excellent emission properties from the colloidal QDs with the advantages of the SiN integration platform, to realize on-chip light sources.

In this chapter, we discuss our work on the optimization of a PECVD based SiN waveguide platform, to better suit the integration purpose.<sup>3</sup>

### 3.1 SiN deposition

The SiN films in this study are deposited using an Advanced Vacuum Vision 310 PECVD tool from UGent cleanroom equipped with two different RF frequency source. One is a high frequency (H-F) source at 13.56 MHz, and the other one is low frequency (L-F) source at 100 kHz. Thus the PECVD system can be operated in three different RF frequency bias mode: high frequency (H-F), low frequency (L-F), and mixed frequency (M-F). Another deposition condition that can be tuned is the temperature of the chamber plate. The temperature can be tuned from room temperature to 270 °C. Moreover, the gas mixture of SiH<sub>4</sub>, NH<sub>3</sub>, and N<sub>2</sub> is used to generate reactive plasma in the chamber, and the gas

	Frequency	Bias Power	Pressure (mT)	N <sub>2</sub> (sccm)	NH <sub>3</sub> (sccm)	SiH <sub>4</sub> (sccm)
<b>H-F</b>	13.56 MHz	30 W	650	1960	40	40
<b>L-F</b>	100 kHz	50 W	650	1960	35	40
<b>M-F</b>	6:1.5(H:L)	30W/50W	650			

**Table 3.1** The detailed recipe for gas ratio, RF bias frequency and power for Advanced Vacuum Vision 310 PECVD SiN deposition. The mixed frequency receipt used a mixed high frequency bias and low frequency bias with a 6:1.5 time ratio.

<sup>3</sup> This work was carried out in close collaboration with Weiqiang Xie from PRG, UGent. Weiqiang Xie fabricated the sample. Yunpeng Zhu measured the sample.

ratio can be tuned and has been optimized to deposit SiN films with refractive indices close to 2.0. Details of the gas ratio, RF bias frequency and power have been listed in Table 3.1.

With the above RF power and chamber pressure, a moderate deposition rate around 7–10 nm/min can be obtained. The complex refractive indices of different SiN films have been measured using ellipsometry.<sup>4</sup> In Figure 3.1(a), it is clear that the high-temperature SiN (H-SiN) has a higher index than the low-temperature SiN (L-SiN). High frequency plasma leads to electrically more active plasma because the electron temperature is more elevated. This leads to a more reactive process which can induce a denser layer. For instance, the index @ 900 nm of L-F SiN changes from 1.931 to 1.862 with decreasing the temperature from 270 °C to 120 °C. The reduction in the material index can be explained by the high hydrogen concentration associated with insufficient reaction during film formation and the porous which comes from the low chamber temperature. The RF frequency bias has little effect on the SiN layer index, while it has a dramatic effect on the extinction coefficient. This difference can be seen from Figure 3.1(b). The extinction coefficient  $k$  @ 900 nm of 120 °C SiN changes from 0.000743 (H-F) to 0.000002 (L-F) with different RF bias frequency. Here we use Cauchy models to fit the data, the absorption from the hydrogen bond in the infrared spectrum cannot be seen from the extinction coefficient measurement. The most general form of Cauchy's equation can be written as  $n(\lambda) = A + \frac{B}{\lambda^2} + \frac{C}{\lambda^4} + \dots$ , where  $n$  is the refractive index,  $\lambda$  is the

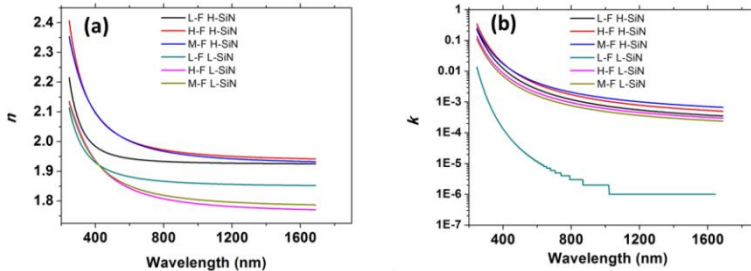


**Figure 3.1:** (a) The ellipsometry measurement results for refractive indices  $n$  of SiN films deposited using different conditions. H-F, L-F and M-F stand for high frequency, low frequency and mixed frequency RF bias. H-SiN stands for high temperature (270 °C) chamber; L-SiN stands for low temperature (120 °C) chamber. (b) The extinction coefficients  $k$  of SiN deposited under different conditions.

<sup>4</sup> We used ellipsometry equipment from J.A. Woollam Company. More details can be found from the company website.

wavelength.  $A$ ,  $B$ ,  $C$ , etc., are coefficients that can be determined for a material by fitting the equation to measured refractive indices at known wavelengths. In the coming section, we will show the waveguide loss measurement results based on different SiN films to find the best SiN deposition recipe for photonics integration.

## 3.2 SiN waveguide loss

Since a low optical loss waveguide platform, especially in the visible range is desired for hybrid colloidal QDs integration, we would like to first experimentally demonstrate a passive low SiN waveguide platform. From the previous ellipsometry measurement, we can conclude that the SiN layer deposited with low RF frequency bias has a lower optical loss.

### 3.2.1 Design and fabrication

We studied fully etched strip waveguides sitting on top of a silicon wafer with a silicon oxide layer in between. The etched strip waveguide will be defined using standard contact lithography and then etched with an optimized etching recipe [31]. The test SiN waveguide samples contain waveguides with width varying from  $0.8\ \mu\text{m}$  to  $2.0\ \mu\text{m}$ . For each width, the sample for the measurement contains a straight reference waveguide and spiral waveguides with variable lengths (1, 2, 4 and 8 cm) for cut-back measurements. The bending radius of the spiral waveguide is fixed at  $100\ \mu\text{m}$ , which shows negligible bending loss according to numerical simulations. Besides the spiral part, at both sides of the waveguides, the widths are tapered to  $3.0\ \mu\text{m}$  to help to get an easier facet cleaving and guarantee a constant coupling in and out between the waveguide and the fiber. The process flow includes substrate preparation and waveguide definition and is shown in Figure 3.2

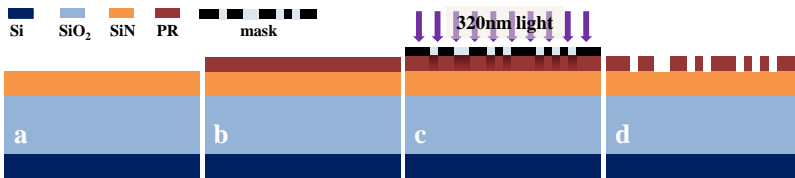


**Figure 3.2:** The lithography process flow for SiN waveguide loss measurement. (a) Prepare substrate, (b) apply resist, (c) exposure, (d) after development. Adapted from ref [31]

As shown in Figure 3.2, the fabrication starts with using a Si (100) wafer with a  $3\ \mu\text{m}$  thermal silicon oxide layer on top. SiN layers with different deposition

condition will be deposited on top of the Si wafer using the recipes mentioned in the last section. Since the ellipsometry results have shown the L-F SiN has a low optical material loss, here we only compare the L-F SiN deposited at high and at low temperatures (H-SiN and L-SiN). After the SiN layers are deposited, the 4-inch wafer was cleaved into 2.5 cm by 2.5 cm chips along the (110) crystal orientation for further process. Using the optimized lithography process, we pattern the chip with AZ701 resist. The waveguides directions have been set parallel to the edge of the cleaved chip for better facet cleaving. Later, the chips will be etched using the optimized RIE recipe (CF<sub>4</sub>/H<sub>2</sub>:40 sccm/3 sccm) [31], and the waveguide patterning will be transferred to the SiN layers and form the strip waveguides. Following acetone and oxygen plasma cleaning which can remove the residual photon resist, the chips are then ready for the measurement.

### 3.2.2 Waveguide loss characterization

The waveguide propagation losses are measured with a cut-back method by measuring the transmission of spiral waveguides with variable lengths. The losses can simply be extracted by fitting the length dependent insertion loss measurement.

A horizontal coupling setup is used for the measurement, as shown in Figure 3.3. Lensed fibers are used to couple light in and out. The fibers are mounted in 2 piezo stages that can be accurately controlled manually by the operator along the XYZ axes, guaranteeing precision alignment of the fiber tip with respect to the waveguide facet. By minimizing the in and out insertion loss, we can obtain an optimized light coupling.

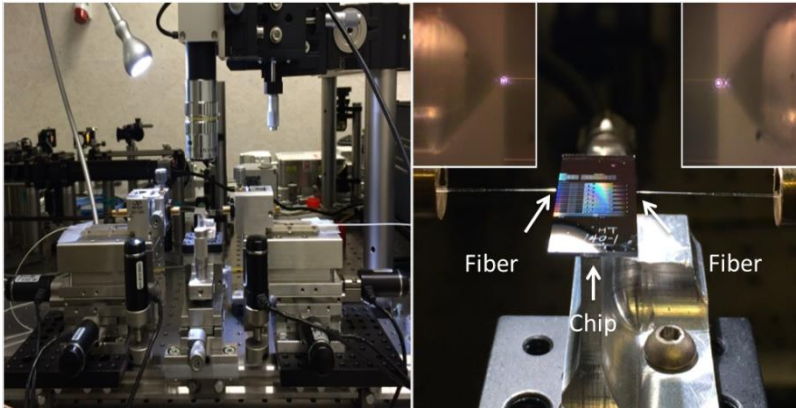


**Figure 3.3:** Picture of the horizontal alignment fiber setup. Left picture is the overview of the whole setup. Right picture is the waveguide chip with already well aligned lensed fibers. The insets are zoomed pictures with a microscope.

Samples with thickness  $\sim 200$  nm are prepared to measure the waveguide loss at  $\lambda=900$  nm, using a near-infrared tunable laser. A polarizer is used to ensure the TE mode is coupled from the input fiber. Single-mode lensed fibers designed for 1550 nm is used for the light couple in and out. The per facet coupling loss (fiber to waveguide) is  $\sim 2.5$ -3 dB at 900 nm.

Waveguide samples with H-SiN and L-SiN are compared. The measurement results have been shown in Figure 3.4. The measurement shows that both for H-SiN and L-SiN the losses rapidly decrease with the increase of the waveguide width from 0.8  $\mu\text{m}$  to 1.2  $\mu\text{m}$ . A more gradual decrease in terms of the waveguide loss can be seen when the waveguide width increases from 1.2  $\mu\text{m}$  to 1.5  $\mu\text{m}$ . With an increased waveguide width (to around 2.0  $\mu\text{m}$ ), the measured waveguide losses are gradually converging to values around 0.94 dB/cm and 1.88 dB/cm, respectively, for H-SiN and L-SiN. The inset of Figure 3.4 shows the transmission of the 2.0  $\mu\text{m}$  wide waveguides for different lengths and the corresponding waveguide loss linear fits. From the measurement, we can also see that L-SiN waveguides are lossier than H-SiN due to the lower optical material quality, which might come from the high hydrogen concentration associated with insufficient reaction during film deposition at the low deposition

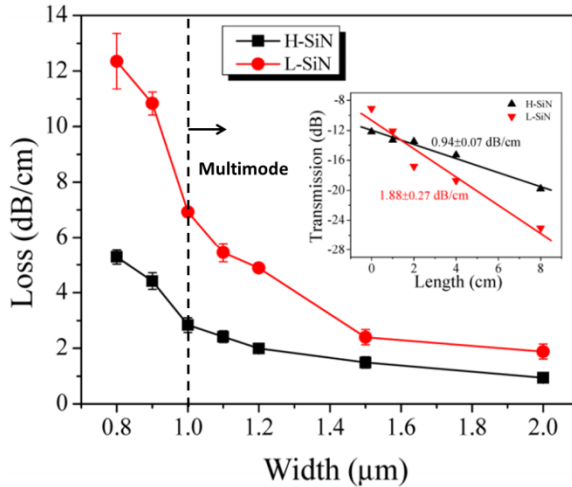


**Figure 3.4:** The measured waveguide losses of H-SiN (270  $^{\circ}\text{C}$ ) and L-SiN (120  $^{\circ}\text{C}$ ) SiN layers deposited with low RF frequency bias. The thickness of all SiN waveguides is  $\sim 200$  nm and the waveguide width are varied from 0.8  $\mu\text{m}$  to 2.0  $\mu\text{m}$ . The inset picture shows the linear fits for H-SiN waveguide and L-SiN with 2.0  $\mu\text{m}$  width. The result has been normalized to the reference waveguides. Waveguide support multimode for width larger than 1  $\mu\text{m}$ . Adapted from ref [31]

temperature. Moreover, the L-SiN layer tends to be more porous than the H-SiN layer, which leads to a lower index and a more lossy film. But still, a 2 dB/cm waveguide loss is already low enough to suit most photonics applications.

### 3.3 Waveguide loss with embedded monolayer QDs

Colloidal QDs have already been used as active materials in various types of photonics waveguide platforms, such as polymer waveguides, silicon oxide waveguides and silicon waveguides. In most cases, the colloidal QDs are either diluted in a polymer matrix [32] or spin coated on the surface of the waveguide or microcavities [33-34]. The polymer platform has known drawbacks, such as a low index contrast and limited long-term stability, giving limits for the colloidal QDs integration applications. For the latter case, colloidal QDs do not have a dielectric encapsulation that acts as a barrier against oxygen and moisture. The exposure to the surroundings in the long term will quench the luminescence properties of the colloidal QDs which also limits the potential of surface coating for colloidal QDs. Moreover, for the surface coating, the coupling between the emission from the QDs and optical mode of the photonics devices is weak, which also limits the applications. Therefore, we aim to demonstrate and optimize a reliable photonics platform with fully integrated QDs.

In the ideal case, a photonics platform for colloidal QDs integration does not only provide encapsulation of the colloidal QDs, protecting them from oxidization and moisture but also provides a better coupling between the emission from the QDs and optical mode of the photonics devices.

Therefore, in this section, relying upon the previously developed low loss passive SiN waveguide platform based on a relatively low temperature (120–270 °C) PECVD process, we develop low-loss hybrid QD-SiN waveguides. They are fabricated using a one-step dry etching process further optimized specifically for the QD-SiN system. We will experimentally show that colloidal QDs can be embedded in between two SiN layers without quenching their luminescence, while in the meantime; the hybrid SiN waveguide still has low optical waveguide loss.

#### 3.3.1 Fabrication process

The fabrication includes waveguide stack preparation and waveguide patterning, as shown in the process flow in Figure 3.5(a). Firstly we start with preparing a SiN/QD/SiN sandwich stack substrate on a silicon wafer with a 3 $\mu$ m thermal SiO<sub>2</sub> layer. The stack is prepared with a ~100 nm L-F H-SiN layer on top of the SiO<sub>2</sub> first, as described in Chapter 3.2. Next, a close-packed monolayer of colloidal QDs was deposited onto the ~100 nm SiN layer by a Langmuir–

Blodgett (LB) method <sup>5</sup>. The LB technique is a way to obtain one or more monolayers of organic material. It is usually deposited from the surface of a liquid onto a solid by immersing (or emerging) the solid substrate into (or from) the liquid. A monolayer is adsorbed homogeneously with each immersion or emersion step. Thus films with monolayers can be formed. CdSe/CdS core/shell colloidal QDs, optimized for visible emission, are used. These dots have an average diameter  $\sim 7.2$  nm and a  $\sim 625$  nm central emission peak. The quality of the colloidal QDs film was examined by scanning electron microscope (SEM) which is presented in Figure 3.5 (b). The photoluminescence (PL) of the deposited colloidal QDs under a UV lamp has also been shown in Figure 3.5 (c). Both results show the uniformity of the deposited monolayer of colloidal QDs. After the deposition of the monolayer colloidal QDs, a second layer of SiN was subsequently deposited for embedding the LB QDs layer with a thickness also  $\sim 100$  nm, using the same PECVD process, to encapsulate the monolayer colloidal QDs layer. For this SiN layer, the chamber temperature has been set to  $120$  °C to minimize the impact on the optical emission quality of the colloidal QDs during the deposition [13]. We still aim to retain sufficient material quality for the SiN to allow for low loss photonic devices. The refractive index on the other hand (measured at  $900$  nm) changes from  $1.931$  to  $1.862$  with the temperature decreasing from  $270$  °C to  $120$  °C, indicating a reduction in the material density. Then, the same photoresist mask previously designed for waveguide loss measurement was used to pattern QD-SiN layers using optimized contact optical lithography. Finally, the waveguide pattern was transferred from the photo resist into the QD-SiN layers by using reactive ion etching (RIE) to form strip waveguides. To compare the influence of the embedded monolayer CQDs on the waveguide loss, we also fabricated the waveguide just using an H-SiN/L-SiN layer stack. Here, the SiN/QD/SiN stack is etched using a single etching step with an optimized RIE etching recipe [31].

---

<sup>5</sup> We also use spin coating for the thicker layers



widths as seen in Figure 3.6. This difference should only come from the embedded colloidal QDs in between of the H-SiN and L-SiN layers.

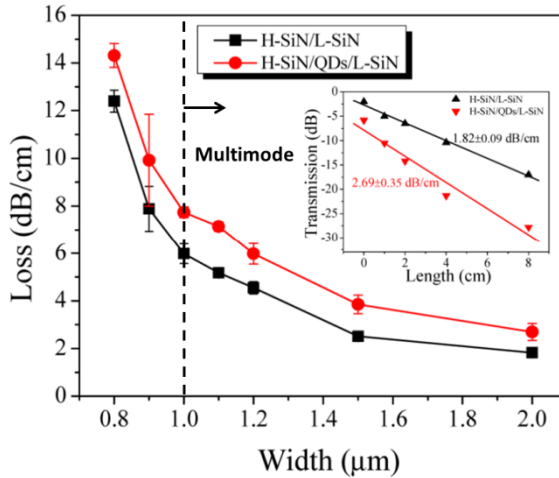


**Figure 3.6:** Waveguide losses with different widths of H-SiN/L-SiN and H-SiN/QD/L-SiN stacked layers. The inset shows the detailed linear fitting of the normalized transmissions of 2 μm wide waveguides at different lengths. Adapted from ref [31].

The colloidal QDs layer does not only introduce roughness at the interfaces between the SiN layer and QDs layer but also introduces sidewall roughness during the RIE process.

### 3.3.3 Embedded QDs luminescence

Since the embedded colloidal QDs were subjected to a PECVD deposition which involves plasma environment and a chamber temperature higher than the room temperature, their optical emission property might degrade. Here, we also perform a PL measurement for the patterned colloidal QDs layers on an H-SiN layer before and after the embedding process, to verify the influence. The result is shown in Figure 3.7. In both cases, the excitation with a 447 nm laser diode was illuminated on the top of the sample surface. The emission was collected from the cleaved facet of a waveguide using a lensed fiber. From the measurement result, a red shift and an increased intensity at a longer wavelength can be observed. This phenomenon can be attributed to wavelength-dependent reabsorption and probably also the process introduced defects lead to the change of the emission profile. However, the main features of the PL spectrum from the

embedded colloidal QDs are well preserved, which shows the potential of the hybrid integration of colloidal QDs.

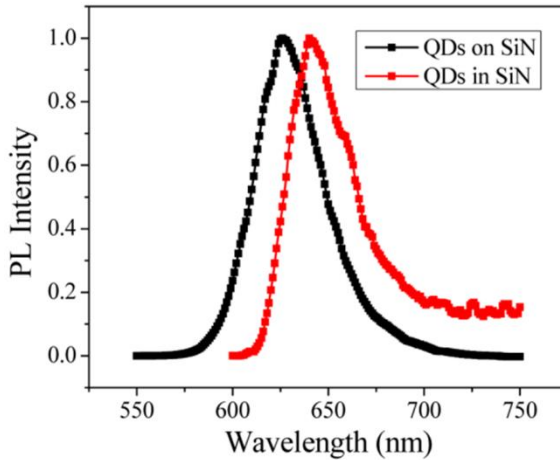


**Figure 3.7:** The collected PL spectra from hybrid SiN waveguides with colloidal QDs on top/embedded. A red shift and an increased intensity can be observed at the longer wavelength, which can be explained by the wavelength-dependent reabsorption and probably also the change of emission profile from the defects. Adapted from ref [31]

In conclusion, we have developed a hybrid QD-SiN integration platform. A lower than 1 dB/cm SiN waveguide loss has been demonstrated. With an embedded monolayer of colloidal QDs in between two SiN layers, the waveguide loss is slightly larger but is lower than 2.7dB/cm. This waveguide loss level is suitable for most photonics applications. The embedded colloidal QDs preserve their luminescence properties. Since the entire fabrication of QD-SiN waveguide wires is CMOS compatible, the present platform can take advantages of existing SiN CMOS technology and enable realizing on-chip low-loss SiN devices integrated with active QDs, in particular, for the integration with on-chip lasers and single photons sources.

### 3.4 SiN layer stress characterization

As mentioned at the beginning of this chapter, SiN layers deposited by LPCVD and PECVD exhibit stress. Compared with LPCVD SiN, PECVD SiN layers exhibit less severe stress. However, in some circumstances, this internal stress from the deposition will still introduce problems for the waveguide platform envisaged as will be explained below.

In general, three types of layer stress are distinguished: tensile, compressive and shear stress. These three types of stress are illustrated in Figure 3.8. Tensile stress is the type of stress in which the two sections of material on either side of a stress plane tend to pull apart or elongate as illustrated in Figure 3.8(a). Compressive stress is the reverse of tensile stress. Adjacent parts of the material tend to press against each other through a typical stress plane as illustrated in Figure 3.8(b). Shear stress exists when two parts of a material tend to slide across each other in any typical plane of shear upon application of force parallel to that plane as illustrated in Figure 3.8(c) [35].

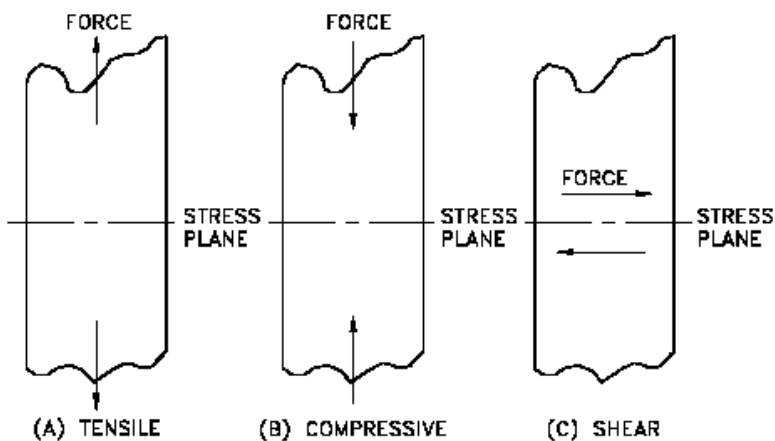


**Figure 3.8:** Types of applied stress. (a) Tensile stress; (b) Compressive stress; (c) Shear stress. Adapted from ref[35]

We usually only consider tensile and compressive stress in SiN films. High tensile stress tends to crack the SiN layers and limits the thickness of SiN obtained via LPCVD systems. On the other hand, compressive stress tends to bend and collapse free hanging membranes and causes failures in the release of MEMS structures. The stress mismatch between different layers will cause the layers to crack or separate from each other leading to failures in forming a multi-layer stacks (e.g. when depositing a SiN layer on a colloidal QDs film). Given its importance for our waveguide platform, we will measure the stress of SiN layers obtained by our PECVD system using different RF frequency bias.

Figure 3.9 shows the general principle of the stress measurement. We start from a flat substrate (usually a silicon wafer). Then the layer/layers we would like to measure will be deposited onto the flat substrate and the stress from the layer/layers will cause the substrate to bend. Assuming the material parameters defining the flat substrate are known, by measuring the bending of the substrate, the stress from an n-layered stack deposited on this substrate can be calculated using the Stoney equation below:

$$\sigma_{total} = \frac{E_s d_s^2}{6(1 - \nu_s) \sum_{i=1}^n d_i} \left( \frac{1}{R_{total}} - \frac{1}{R_{substrate}} \right) \quad 3.1$$

where  $\sigma_{total}$  is the stress from the layer/layers,  $E_s$  is the Young's modulus of the substrate,  $d_s$  is the substrate thickness,  $\nu_s$  is the Poisson ratio of the substrate,  $d_i$  is the thickness of the deposited layer/layers and  $R$  is the measured radius of the curvature. The application of this equation involves the following assumptions [36]. However, for our measurement, this equation can be used to determine the layer stress.

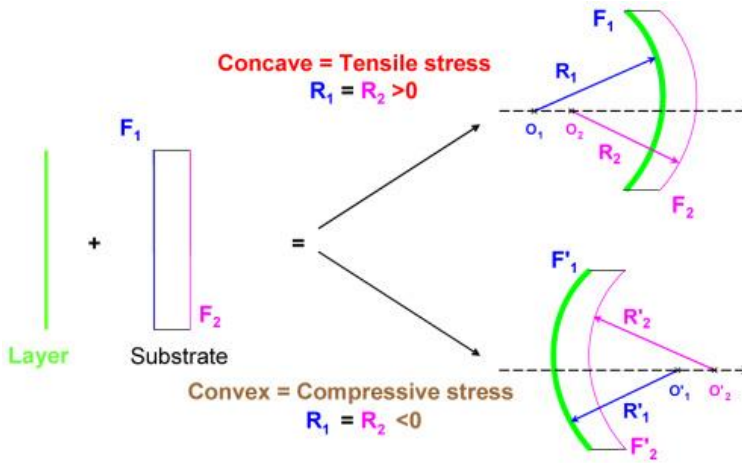


**Figure 3.9:** The general principle of the stress measurement. Adapted from ref [37].

Bare silicon chips with size 2 cm by 2 cm are prepared. The curvatures of the chips are measured using Dektak surface profiler before the SiN layer deposition. The Dektak surface profiler scans the surface of the whole sample and records the height data. Then, ~100 nm thick SiN layers were deposited on top of these silicon chips with different deposition conditions. The deposition temperature is 270 °C. The curvature of the chips is again measured. From the difference in the curvature before and after deposition, the stress of the SiN layers is calculated and the results are shown in Table 3.2.

SiN Type	Stress Type	Average Stress (MPa)
H-F SiN	Tensile	774
M-F SiN	Tensile	400
L-F SiN	Compressive	1046

**Table 3.2:** Stress type and average stress of different type of SiN layer

The results show SiN layers deposited with different RF bias have different stress in term of strength and type, which is common for SiN layers [38]. L-F SiN has compressive stress with average stress of 1046 MPa. On the contrary, H-F SiN has tensile stress with average stress of 774 MPa; M-F SiN has slightly lower tensile stress with average stress of 400 MPa. These measurement results are used in section 4.2.1 and section 5.1.2 to help choose SiN layers with suitable layer stress.

### 3.5 SiN fluorescence measurement

SiN obtained with PECVD and LPCVD is amorphous, hence the layers usually have defects, and these defects can act as fluorescence centers when the SiN layer is illuminated with light. This fluorescence phenomenon is typically negligible for normal waveguiding applications. But for some applications like Raman spectroscopy and on-chip single photon sources, this fluorescence can introduce background noise, which might hide the real signal.

Therefore, here we would like to characterize the intensity of the fluorescence signal of SiN layers deposited under different conditions using our PECVD system. This characterization will help to choose the optimal deposition condition for low background fluorescence applications.

We used a photon counting system to characterize the SiN material fluorescence as shown in Figure 3.10. The excitation beam of the setup is produced by a PicoQuant LDH-DC-440M laser diode. The excitation beam was focused on the sample using an Olympus objective lens (100x 0.75NA). The beam was then shaped using a digital micro-mirror device (Texas Instrument, 0.55" XGA 2x LVDS DMD) to allow custom excitation patterns. SiN samples with different deposition conditions will be illuminated by the laser beam and the fluorescence will be collected by the objective and send to a photon counter. We will use the counts per nm to compare the fluorescence intensity from the different SiN samples:

$$\text{Counts per nm} = \frac{\text{Total Counts} - \text{Background Counts}}{\text{thickness of SiN}} \quad 3.2$$

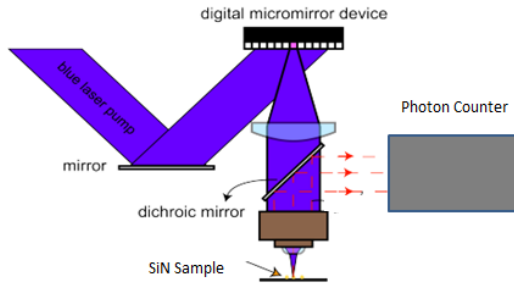


**Figure 3.10:** Photon counting system for material fluorescence measurement. Adapted from [39].

For the experiment,  $\sim 200$  nm of different types of SiN layers have been deposited directly on a clean Si sample, to avoid fluorescence from the substrate. All samples have been measured by ellipsometry to obtain the sample thickness accurately. Next, the samples were illuminated under the same initial conditions (fixed pattern on the DMD and  $300 \text{ W/cm}^2$  laser pump power intensity). The photon counts number was obtained with 3 second exposure time with the photon counter. The fluorescence from these SiN layers was then collected by the photon counter. To eliminate the background noise<sup>6</sup>, the background counts are recorded with a bare silicon wafer as a reference.

Figure 3.11 shows the measurement results. First of all, the SiN deposited with mixed and high frequency bias has higher fluorescence compared with the SiN deposited with low frequency bias. The measurement also shows SiN layers deposited with high chamber temperature tend to have higher fluorescence than the SiN layers deposited with low chamber temperature. The SiN deposited with low frequency and low chamber temperature has the lowest fluorescence, close to the background noise limit. For our PECVD system, this type of SiN is most suitable for low fluorescence applications.

<sup>6</sup> The background noise comes from the dark current of the photon counter. The background counts level is around 262000

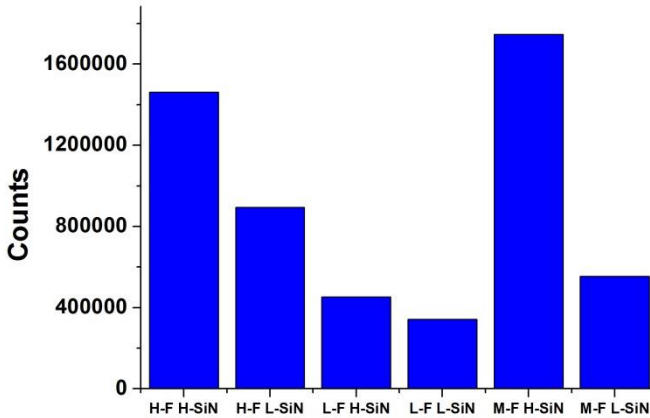


**Figure 3.11:** Photoluminescence measurements from different SiN layers.

### 3.6 Conclusion

In this chapter, we have shown the information about the development of the hybrid SiN colloidal QDs integration platform. We first demonstrated a passive SiN waveguide platform with an optical loss at 0.94 dB/cm @ 900 nm with a waveguide dimension 2  $\mu\text{m}$  by 200 nm. With a monolayer of embedded colloidal QDs in between, the waveguide can still maintain a waveguide loss around 2.69 dB/cm @ 900 nm. This hybrid SiN colloidal QDs platform has been optimized for the heterogeneous integration. The SiN layer stress for different deposition recipes has been presented. L-F SiN has compressive stress with the average stress of 1046 MPa. H-F SiN has tensile stress with the average stress of 774 MPa; M-F SiN has slightly lower tensile stress with the average stress of 400 MPa. The luminescence of the SiN material itself for different deposition recipe has also been compared. For low fluorescence background applications, it is better to use L-F L-SiN as the waveguide material.

## References

- [1] Bauer, J. "Optical properties, band gap, and surface roughness of Si<sub>3</sub>N<sub>4</sub>." *physica status solidi (a)* 39, no. 2 (1977): 411-418.
- [2] Philipp, Herbert R. "Optical properties of silicon nitride." *Journal of the Electrochemical Society* 120, no. 2 (1973): 295-300.
- [3] Rahim, Abdul, Eva Ryckeboer, Ananth Z. Subramanian, Stéphane Clemmen, Bart Kuyken, Ashim Dhakal, Ali Raza et al. "Expanding the Silicon Photonics Portfolio With Silicon Nitride Photonic Integrated Circuits." *Journal of Lightwave Technology* 35, no. 4 (2017): 639-649.
- [4] Morosanu, C-E. "The preparation, characterization and applications of silicon nitride thin films." *Thin Solid Films* 65, no. 2 (1980): 171-208.
- [5] Habraken, F. H. P. M. *LPCVD silicon nitride and oxynitride films: material and applications in integrated circuit technology*. Springer-Verlag New York, Inc., 1991.
- [6] Lanford, W. A., and M. J. Rand. "The hydrogen content of plasma - deposited silicon nitride." *Journal of Applied Physics* 49, no. 4 (1978): 2473-2477.
- [7] Kapoor, Vikram J., Robert S. Bailey, and Herman J. Stein. "Hydrogen - related memory traps in thin silicon nitride films." *Journal of Vacuum Science & Technology A: Vacuum, Surfaces, and Films* 1, no. 2 (1983): 600-603.
- [8] Habraken, F. H. P. M. "Characterization of LPCVD and PECVD silicon oxynitride films." *Applied Surface Science* 30, no. 1-4 (1987): 186-196.
- [9] Denisse, C. M. M., K. Z. Troost, F. H. P. M. Habraken, W. F. Van der Weg, and M. Hendriks. "Annealing of plasma silicon oxynitride films." *Journal of applied physics* 60, no. 7 (1986): 2543-2547.
- [10] Habraken, F. H. P. M., and A. E. T. Kuiper. "Silicon nitride and oxynitride films." *Materials Science and Engineering: R: Reports* 12, no. 3 (1994): 123-175.
- [11] Yota, J., J. Hander, and A. A. Saleh. "A comparative study on inductively-coupled plasma high-density plasma, plasma-enhanced, and low pressure chemical vapor deposition silicon nitride films." *Journal of Vacuum Science & Technology A: Vacuum, Surfaces, and Films* 18, no. 2 (2000): 372-376.

- [12] Henry, Charles H., R. F. Kazarinov, H. J. Lee, K. J. Orlowsky, and L. E. Katz. "Low loss Si<sub>3</sub>N<sub>4</sub>-SiO<sub>2</sub> optical waveguides on Si." *Applied optics* 26, no. 13 (1987): 2621-2624.
- [13] Bruno, Franco, Massimo del Giudice, Roberto Recca, and Francesco Testa. "Plasma-enhanced chemical vapor deposition of low-loss SiON optical waveguides at 1.5- $\mu$ m wavelength." *Applied optics* 30, no. 31 (1991): 4560-4564.
- [14] Stutius, W., and W. Streifer. "Silicon nitride films on silicon for optical waveguides." *Applied Optics* 16, no. 12 (1977): 3218-3222.
- [15] Dutta SU, Jackson H, Boyd J, Davis R, Hickernell F. "CO<sub>2</sub> laser annealing of Si<sub>3</sub>N<sub>4</sub>, Nb<sub>2</sub>O<sub>5</sub>, and Ta<sub>2</sub>O<sub>5</sub> thin-film optical waveguides to achieve scattering loss reduction." *IEEE Journal of Quantum Electronics*. 1982 Apr;18(4):800-6.
- [16] Sriram, S., W. D. Partlow, and C. S. Liu. "Low-loss optical waveguides using plasma-deposited silicon nitride." *Applied optics* 22, no. 23 (1983): 3664-3665.
- [17] Melchiorri, M., N. Daldosso, F. Sbrana, L. Pavesi, G. Pucker, C. Kompocholis, P. Bellutti, and A. Lui. "Propagation losses of silicon nitride waveguides in the near-infrared range." *Applied Physics Letters* 86, no. 12 (2005): 121111.
- [18] Shaw, Michael J., Junpeng Guo, Gregory A. Vawter, Scott Habermehl, and Charles T. Sullivan. "Fabrication techniques for low-loss silicon nitride waveguides." In *Proc. SPIE*, vol. 5720, pp. 109-118. 2005.
- [19] Morichetti, Francesco, Andrea Melloni, Mario Martinelli, René G. Heideman, Arne Leinse, Douwe H. Geuzebroek, and Albert Borreman. "Box-shaped dielectric waveguides: A new concept in integrated optics?." *Journal of Lightwave Technology* 25, no. 9 (2007): 2579-2589.
- [20] Bauters, Jared F., Martijn JR Heck, Demis D. John, Jonathon S. Barton, Christiaan M. Bruinink, Arne Leinse, René G. Heideman, Daniel J. Blumenthal, and John E. Bowers. "Planar waveguides with less than 0.1 dB/m propagation loss fabricated with wafer bonding." *Optics Express* 19, no. 24 (2011): 24090-24101.
- [21] Dai, Daoxin, Zhi Wang, Jared F. Bauters, M-C. Tien, Martijn JR Heck, Daniel J. Blumenthal, and John E. Bowers. "Low-loss Si<sub>3</sub>N<sub>4</sub> arrayed-waveguide grating (de) multiplexer using nano-core optical waveguides." *Optics express* 19, no. 15 (2011): 14130-14136.

- [22] Hosseini, Ehsan Shah, Siva Yegnanarayanan, Amir Hossein Atabaki, Mohammad Soltani, and Ali Adibi. "High quality planar silicon nitride microdisk resonators for integrated photonics in the visiblewavelength range." *Optics express* 17, no. 17 (2009): 14543-14551.
- [23] Dhakal, Ashim, Pieter C. Wuytens, Frédéric Peyskens, Karolien Jans, Nicolas Le Thomas, and Roel Baets. "Nanophotonic waveguide enhanced Raman spectroscopy of biological submonolayers." *ACS Photonics* 3, no. 11 (2016): 2141-2149.
- [24] Martens, Daan, and Peter Bienstman. "Comparison between Vernier-cascade and MZI as transducer for biosensing with on-chip spectral filter." *Nanophotonics* (2017).
- [25] Ikeda, Kazuhiro, Robert E. Saperstein, Nikola Alic, and Yeshaiahu Fainman. "Thermal and Kerr nonlinear properties of plasma-deposited silicon nitride/silicon dioxide waveguides." *Optics express* 16, no. 17 (2008): 12987-12994.
- [26] Levy, Jacob S., Alexander Gondarenko, Mark A. Foster, Amy C. Turner-Foster, Alexander L. Gaeta, and Michal Lipson. "CMOS-compatible multiple-wavelength oscillator for on-chip optical interconnects." *Nature photonics* 4, no. 1 (2010): 37-40.
- [27] Kippenberg, Tobias J., Ronald Holzwarth, and S. A. Diddams. "Microresonator-based optical frequency combs." *Science* 332, no. 6029 (2011): 555-559.
- [28] Moss, David J., Roberto Morandotti, Alexander L. Gaeta, and Michal Lipson. "New CMOS-compatible platforms based on silicon nitride and Hydex for nonlinear optics." *Nature Photonics* 7, no. 8 (2013): 597-607.
- [29] Eichenfield, Matt, Ryan Camacho, Jasper Chan, Kerry J. Vahala, and Oskar Painter. "A picogram and nanometer scale photonic crystal optomechanical cavity." *arXiv preprint arXiv:0812.2953* (2008).
- [30] Wiederhecker, Gustavo S., Long Chen, Alexander Gondarenko, and Michal Lipson. "Controlling photonic structures using optical forces." *Nature* 462(7273), 633-U103 (2009).
- [31] Xie, Weiqiang, Yunpeng Zhu, Tangi Aubert, Steven Verstuyft, Zeger Hens, and Dries Van Thourhout. "Low-loss silicon nitride waveguide hybridly integrated with colloidal quantum dots." *Optics express* 23, no. 9 (2015): 12152-12160.
- [32] Guilhabert, B., Caroline Foucher, Anne-Marie Haughey, E. Mutlugun, Y. Gao, Johannes Herrnsdorf, H. D. Sun, H. V. Demir, M. D. Dawson, and

- Nicolas Laurand. "Nanosecond colloidal quantum dot lasers for sensing." *Optics express* 22, no. 6 (2014): 7308-7319.
- [33] Dang, Cuong, Joonhee Lee, Craig Breen, Jonathan S. Steckel, Seth Coe-Sullivan, and Arto Nurmikko. "Red, green and blue lasing enabled by single-exciton gain in colloidal quantum dot films." *Nature nanotechnology* 7, no. 5 (2012): 335-339.
- [34] Min, Bumki, Sungjee Kim, Koichi Okamoto, Lan Yang, Axel Scherer, Harry Atwater, and Kerry Vahala. "Ultralow threshold on-chip microcavity nanocrystal quantum dot lasers." *Applied physics letters* 89, no. 19 (2006): 191124.
- [35] <http://www.tpub.com/doematerialsci/materialscience15.htm>
- [36] Feng, X., Y. Huang, and A. J. Rosakis. "On the Stoney formula for a thin film/substrate system with nonuniform substrate thickness." *Journal of Applied Mechanics* 74, no. 6 (2007): 1276-1281.
- [37] Piombini, Hervé, François Compoin, Chrystel Ambard, Didier Picart, Philippe Belleville, Gille Damamme, and Fabrice Brémand. "Stress measurement of elastic sol-gel layer by photoelasticity-comparison with Stoney." *Optical Materials Express* 6, no. 2 (2016): 469-485.
- [38] Claassen WA, Valkenburg WG, Willemsen MF, vd Wijgert WM., "Influence of deposition temperature, gas pressure, gas phase composition, and RF frequency on composition and mechanical stress of plasma silicon nitride layers." *Journal of the Electrochemical Society* 132, no. 4 (1985): 893-898.
- [39] De Geyter, Bram, Katarzyna Komorowska, Edouard Brainis, Philippe Emplit, Pieter Geiregat, Antti Hassinen, Zeger Hens, and Dries Van Thourhout. "From fabrication to mode mapping in silicon nitride microdisks with embedded colloidal quantum dots." *Applied physics letters* 101, no. 16 (2012): 161101.



# 4

## Colloidal quantum dots as gain material for the SiN platform

In the previous chapter, we have developed a hybrid silicon nitride (SiN) photonics platform optimized for colloidal quantum dots (QDs) heterogeneous integration. Based on this hybrid waveguide platform, low optical loss SiN waveguides with an embedded QDs layer has been achieved. The embedded QDs preserve their luminescence, which already is a remarkable step towards realizing light generation for the SiN waveguide platform. In this chapter, we further investigate whether we can obtain coherent light from these embedded QDs.

As mentioned in Chapter 2, over the past 15 years, colloidal QDs have shown that depending on their shape, size and composition, they can exhibit net optical gain at visible wavelength [1]. Various laser devices based on colloidal QDs have been demonstrated. Some early demonstrations were using accidental ad hoc resonators [2]. Later, some reports have shown laser designs with vertical cavities where QDs are put between reflectors [3]. Some other designs involved coated surface gratings [4-5] and silica microspheres [6]. While these studies are

relevant in terms of characterization and understanding the fundamental material parameters of the colloidal QDs, they are less relevant in terms of long term application potential. The research has then gradually moved to combine the colloidal QDs with an integrated waveguide platform. A lot of work has been done to embed the colloidal QDs in polymers [7-8]. Distributed feedback (DFB) based polymer lasers have been reported with a remarkable low lasing threshold. But the polymer platform has several drawbacks including a low index contrast and a limited long-term stability. In other work, compact colloidal QD layers were coated over prefabricated quartz gratings [5]. However, this approach lacks a proper encapsulation of the colloidal QD layers. The colloidal QD layers are exposed to the surroundings, which not only bring issues to the post-processing, but these coated colloidal QD layers also lack a protection barrier against oxygen and moisture. Moreover, coupling light of such devices to other on-chip integrated structures cannot be easily achieved, which also limits its application potential. In addition, these surface coated colloidal QDs can easily get released from the substrate into the air with air flow or physical collision. These nanoparticles pose risks to human health and the environment under certain conditions. Hence encapsulation is a must to reduce these risks.

In this chapter, we will experimentally demonstrate on-chip lasers with colloidal QDs as gain material, using the previously optimized hybrid colloidal QD SiN platform. We will first characterize the colloidal QD material gain and gain lifetime in the solution phase, by using a Transient Absorption Spectroscopy (TAS) system. We will also measure the modal gain of hybrid QD SiN waveguides with an improved waveguide based variable stripe length method. Single mode DFB lasers have been designed, fabricated and characterized, showing a lasing threshold of  $270 \mu\text{J}/\text{cm}^2$  under 7 ns pulse 532 nm laser pump. The equivalent CW threshold is about  $39 \text{ kW}/\text{cm}^2$ , which is at the same level as that of III-V semiconductor lasers epitaxially grown on silicon [9]. Also, a gain-coupled DFB laser has been demonstrated, showing the flexibility of colloidal QDs as solution synthesized materials, which can act as paint-on optical gain materials. In the last part of this chapter, we also combined our SiN platform with colloidal nanoplatelets (NPLs). These NPLs still show amplified spontaneous emissions as in the solution phase after being embedded into the SiN layers. This showcases our SiN platform's versatility and the potential for embedding also other types of solution processed materials.

## 4.1 Characterization of colloidal QDs material gain

In Chapter 2, we have analyzed the importance of the biexciton lifetime for achieving a low CW lasing threshold, as shown in Eq. 2.24. The biexciton lifetime is a combination of both radiative recombination and the nonradiative

Auger process, as expressed in Eq. 2.25. To sum up, for low lasing threshold applications, colloidal QDs with longer biexciton lifetime/decay rate will have a better performance in terms of a low lasing threshold.

To date, CdSe/CdS colloidal QDs are the most promising colloidal QDs for lasing applications, as they have shown high optical gain coefficients, long gain lifetime and exceptional stability [1]. As we have already demonstrated from Chapter 3.3.3, they still exhibit photoluminescence after embedding them into SiN layers and going through a PECVD process. In this work, we use so-called *flash* CdSe/CdS colloidal QDs. They are synthesized by Tangi Aubert from the PCN group using a seeded growth approach that yields thick shell CdSe/CdS colloidal QDs in a fast and simple process [10-11]. The synthesis starts with wurtzite CdSe seed QDs with a diameter of 4 nm. CdS shells are latter been grown on the surface of the seed QDs. The average total diameter of 11.5 nm hence corresponds to an average shell thickness of 3.75 nm. Such colloidal QDs feature an alloyed CdSe/CdS interface. This interface can not only reduce strain introduced by the mismatch from the two materials but also slow down nonradiative Auger recombination of bi-/multi-excitons [10]. The latter is important to suppress the Auger recombination and have a longer biexciton lifetime [12]. Figure 4.1 shows the transmission electron microscope (TEM) picture of the corresponding colloidal QDs and the inset is the solution luminescence under illumination by a UV lamp.

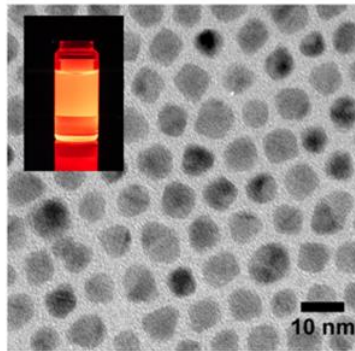


**Figure 4.1:** The TEM picture of flash CdSe/CdS colloidal QDs, the inset is the solution luminescence under UV lamp. Adapted from ref [10].

Figure 4.2 presents the measured photoluminescence spectrum of the QDs, which is centered around 635 nm. The photoluminescence spectrum has a linewidth around 29 nm and comes with a photoluminescence quantum yield of around 80%. In the time-resolved fluorescence experiment, we have a multi-exponential decay. We measure on an ensemble of QDs, which means that different QDs can exhibit different lifetimes. In addition, delayed emission can

extend the fluorescence decay as well. That is why we define an average lifetime. From the measurement, we extracted it as:

$$\tau_{avg} = \frac{\int_0^{\infty} tI(t)dt}{\int_0^{\infty} I(t)dt} \quad (4.1)$$

By using the above equation, an average lifetime around 58.5 ns has been calculated from the measurement.

However, the decay is also reasonably well approximated by a single-exponential decay. We can use this model to extract the single exciton lifetime from this measurement, which is more relevant for the laser threshold analysis. A 26.8 ns single exciton lifetime can be fitted and extracted.

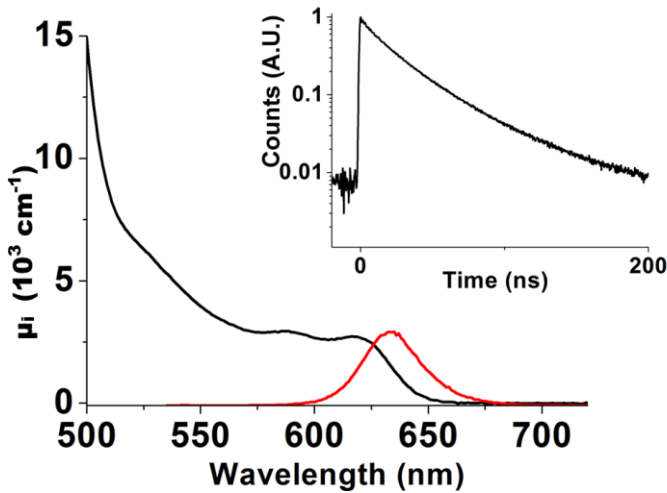


**Figure 4.2:** Absorption (expressed as intrinsic absorption coefficient ( $\mu_i$ ) and emission (red) spectrum after excitation at 400 nm. The QDs have a luminescence quantum yield of 80%. Inset: photoluminescence (PL) decay showing an average decay time of 58.5 ns, a single exciton lifetime of 26.8 ns.

We assessed the potential of these QDs for optical gain by measuring the temporal non-linear optical properties of a QD dispersion using an ultrafast TAS system. TAS is a pump-probe technique, and the layout of the setup has been shown in Figure 4.3.<sup>7</sup> In this measurement, we usually prepare a diluted

<sup>7</sup> The TAS measurement of the *flash* colloidal QDs was carried out by Suzanne Bisschop from the PCN group UGent. The data analysis was done by Yunpeng Zhu

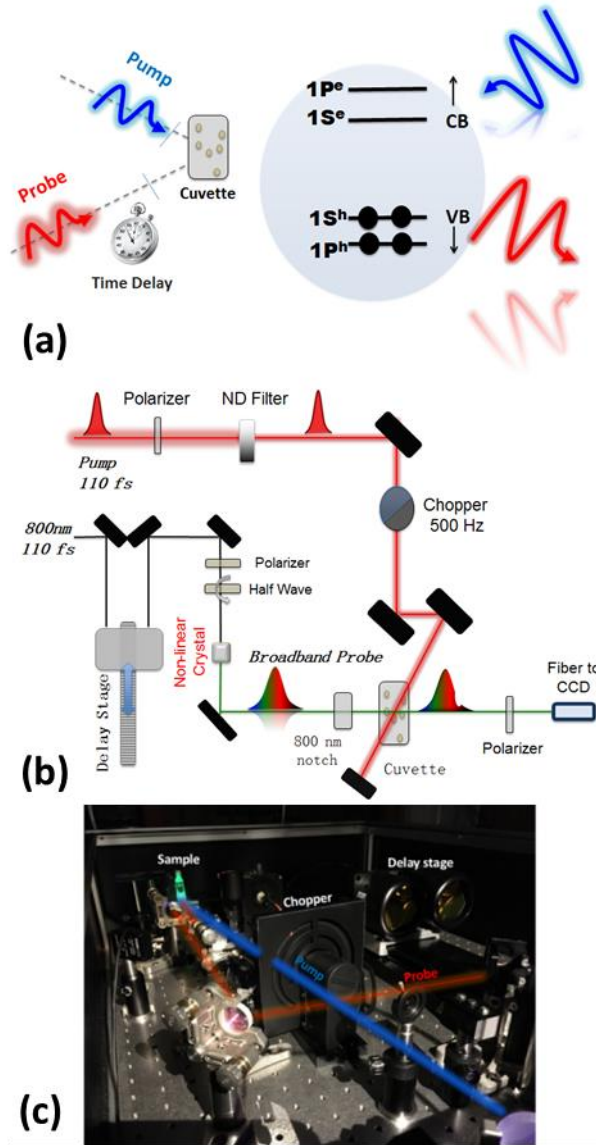


**Figure 4.3:** Transient Absorption Spectroscopy (TAS) system. (a) The principle of the TAS system. A pump-probe method is used to determine the absorption change of the sample. (b) The schematic of the TAS system. (c) The picture of the TAS system.

colloidal QDs sample with a certain concentration in a cuvette, as shown in Figure 4.3(a). Then we use the TAS system to measure the change of transmission between a pumped and an unpumped sample of a short pulse

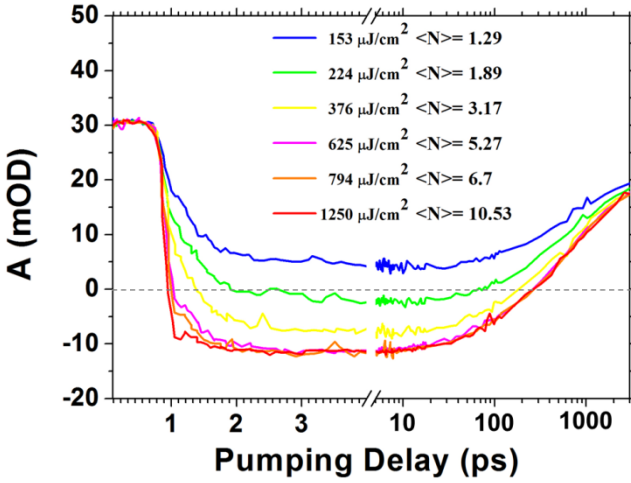
probe beam as a function of both pump-probe time delay and probe wavelength. The sample is pumped with ultrashort laser pulses (in this case, 110 fs with a 1k Hz repetition rate) after which the change in absorbance  $\Delta A$  is measured by a time-delayed probe pulse generated by non-linear crystal to obtain a broadband probe beam (also 110 fs) as function of wavelength (or energy). Combining  $\Delta A$  with the linear absorption spectrum, we can obtain the absorbance  $A$  of the sample at a certain time delay and probe wavelength. If  $A$  turns negative, the dispersion exhibits optical gain, and both the gain threshold and the spectral gain window can be experimentally determined. In addition, the TAS measurement provides the time evolution of the non-linear absorbance, such that the rate of the processes that quench the optical gain and hence the gain or inversion lifetime can be assessed. Moreover, since the concentration of the diluted sample has been preset, we can also calculate the material gain of the colloidal QDs.

Figure 4.4 shows the transient absorbance at 630 nm of the flash colloidal QDs dispersed in toluene, after pumping with a 520 nm beam. The pump intensity is expressed in terms of the average number of excitations or the exciton density  $\langle N \rangle$  calculated per QD, using the photon fluence and the QD absorption cross section. The photon fluence is defined as the photon number incident per area. The absorption cross section  $\sigma$  of a QD can be derived from molar absorption coefficient  $\varepsilon$ , as the latter is correlated with the concentration of absorbers (in  $\text{mol m}^{-3}$ ), while the former is correlated with the number of absorbers per unit volume (in  $\text{m}^{-3}$ ).  $\sigma$  has units of area and can be expressed in:

$$\sigma = \frac{\ln 10}{N_A} \varepsilon = V_{QD} \mu_i \quad (4.2)$$

Hence we can use Eq. 4.2 to calculate  $\sigma$  by multiplying the intrinsic absorption coefficient  $\mu_i$  with the QD volume [13]. The coefficient  $\mu_i$  is measured at 350 nm, and can be rescaled to a value at 532 nm using the absorbance spectrum. For the QDs we are using in the thesis, the calculated absorption cross section is  $2.75 \times 10^{-15} \text{ cm}^2$  @ 532 nm pump wavelength.

From the measurement in Figure 4.4, we can observe that the gain has a rapid buildup, taking less than 1 ps, even when the pump intensity is just above the gain threshold. The gain can last up to 270 ps for the highest pump fluence we used. More importantly, from the TAS measurement in Figure 4.4(a), we estimate that the process caused the decay of the non-linear absorbance at the lowest fluence used has a rate constant of  $\sim 2 \text{ ns}^{-1}$  (equivalent to a  $\sim 500$  ps bi-



**Figure 4.4:** The time dependent dynamics of  $A$  at a fixed probe wavelength of 630 nm after 520 nm excitation. We can see the optical gain builds up very fast ( $< 2$  ps) and can last up to 270 ps. Importantly, from the TA traces, we estimate that the process that causes the decay of the non-linear absorbance at the lowest fluences used has a rate constant of  $\sim 2$  ns $^{-1}$  (500 ps bi-exciton lifetime).

exciton lifetime) a considerable improvement compared to CdSe/CdS QDs without the alloyed interface ( $\sim 350$  ps) [12]. As we concluded in chapter 2, this improved biexciton lifetime is very favourable for lasing applications exploiting a gain process dominated by Auger recombination of the biexciton.

As mentioned previously, since the concentration of the colloidal QD solution is preset before the TAS measurement, the nonlinear absorbance allows us to calculate the actual material gain in a quantitative way, using the equation below:

$$g_m(\lambda, t) = -A(\lambda, t) \frac{\mu_{i,0}(\lambda_{ref})}{A_0(\lambda_{ref})} \quad (4.3)$$

We can obtain the final value by normalizing the non-linear absorbance using the intrinsic absorption coefficient at the reference wavelength  $\lambda_{ref}$ , taken here as 350 nm. Figure 4.5 plots the thus calculated material gain spectrum at a 2.5 ps time delay for different pump fluences. It can be seen from the results that the gain is first attained at the long wavelength side ( $> 640$  nm) of the absorption feature, when increase the exciton density beyond 1.2 excitons per QD. This observation is in line with the theoretical predictions of ref [14]. If we further increase the pump fluence, the gain increases and its spectrum broaden. Eventually, the gain window extends from 550 nm to 680 nm. The material gain levels off at maximum values of around 1200 cm $^{-1}$  at 615 nm. The two

predominant peaks in Figure 4.5 come from two different transitions. When the QDs are pumped with higher fluence, there are high order multi-excitons, which corresponding to the second peak around 575 nm.

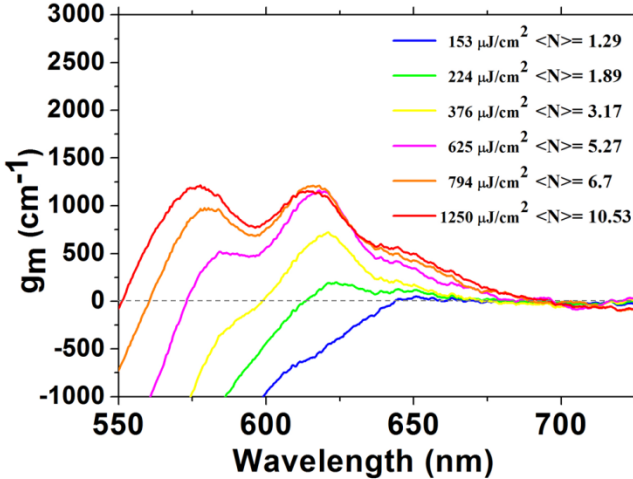


**Figure 4.5:** Material gain at 2.5 ps with 520 nm pump at different pump intensity, the total bandwidth can be as large as 130 nm reaching ca.  $1200 \text{ cm}^{-1}$  at 615 nm.

The TAS measurements demonstrate these QDs exhibit optical gain in solution. The single exciton and bi-exciton lifetimes can be extracted from the measurement, which can help us to analyze the laser's threshold based on these types of colloidal QDs. The material gain can also be calculated from this measurement, which is also helpful for us to design the laser cavity.

## 4.2 Waveguide modal gain measurement

The TAS measurements from the previous section provide the detailed material gain coefficient of the colloidal QDs. But for the real application, the colloidal QDs usually are spin coated to form a compact layer rather than being dispersed in solution. Therefore, we should also verify the modal gain coefficient of such a compact layer if we want to design devices exploiting such compact layers.

The optical gain coefficient of semiconductor material is usually measured by the variable stripe length (VSL) technique, as shown in Figure 4.6. This method has been firstly introduced during the 1970s. The big advantage of this widely used experimental method is that no special sample preparation is needed and samples on top of opaque substrates are equally suited for gain measurements. In addition, the basic model describing the technique is extremely simple: the

one-dimensional amplifier model [15]. However, the technique also has some limitations. Diffraction of the pump beam can lead to false gain values. More importantly, most of the significant ASE arises from the emitting elements near  $z = L$ , which experience the largest single pass gain. It is always assumed that  $\Omega(z) \cong \Omega = S/L^2$ , where  $S$  is the collection area and  $L$  is the pump beam length. However, the  $z$ -dependence of  $\Omega(z)$  strongly affects the collection efficiency of the ASE signals. The condition  $\Omega(z) \cong \Omega$  corresponds to the assumption of constant collection efficiency, a hypothesis which is satisfied for optical amplifiers based on optical fibers or ridge waveguides. But this is not fulfilled for planar waveguides, which is the case where this method is used most, where the modes spread in the slab waveguide plane introducing  $z$  dependence in the otherwise constant collection efficiency. In addition, inhomogeneous coupling can also arise as a result of an inappropriate choice of the numerical aperture of the collection optics used in the experiments. These inherent problems can make the results of the VSL measurement highly misleading.

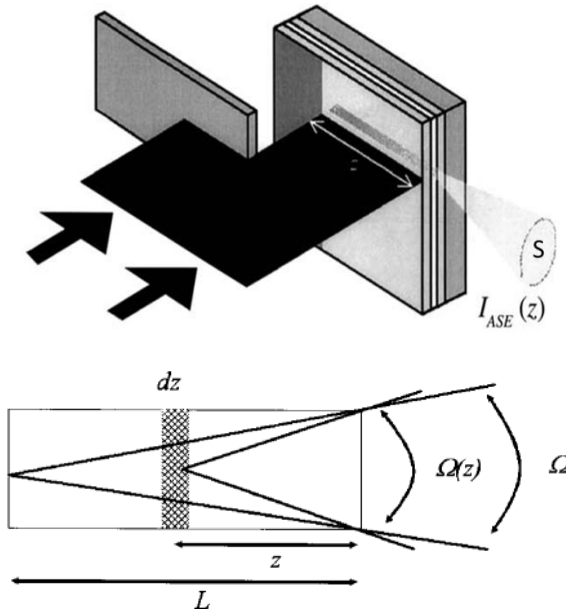


**Figure 4.6:** Sketch of the variable stripe length configuration. The amplified spontaneous emission intensity  $I_{ASE}(z)$  is collected from the edge of the sample as a function of the excitation length  $z$ . The optical pump beam is usually focused on a thin stripe with a cylindrical lens. Adapted from ref [15].

Given these limitations, we aimed to improve the traditional VSL measurements by developing a waveguide based VSL measurement that solves these inherent problems. By replacing the planar slab waveguide with a ridge

waveguide, there is no need to consider the  $z$  dependent collection angle. Only the optical mode in the ridge waveguide can get amplified and later collected at the edge. The ridge waveguide surface area defines the pump area, which helps to limit the pump light diffraction problem. Moreover, the pump beam lengths are accurately defined by using ridge waveguides with variable length, which reduces the inaccuracy from the adjustable slit [16].

In the coming sections, we will present the sample fabrication, the measurement technique itself and the results of these improved waveguides based VSL modal gain measurement.

### 4.2.1 Fabrication processes

We fabricate ridge waveguides containing *flash* CdSe/CdS core/shell colloidal QDs with variable lengths. The samples are fabricated as shown in Figure 4.7.

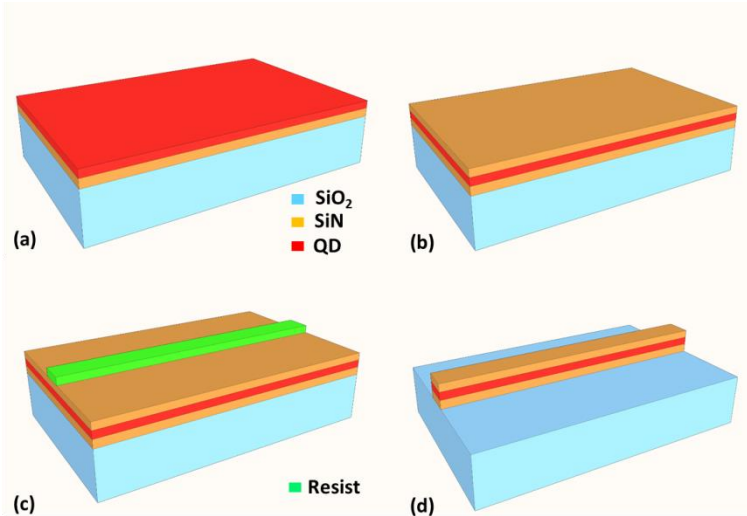


**Figure 4.7:** The fabrication flow of waveguides with variable stripe length. (a) a  $\sim 100$  nm thick L-F H-SiN is deposited on top of a silicon wafer with a  $3 \mu\text{m}$  thermal oxide. Then the *flash* CdSe/CdS core/shell colloidal QDs are spin-coated on top of this SiN. (b) a  $\sim 100$  nm thick M-F H-SiN is deposited onto the colloidal QD layer. (c) Lithography is used to define the waveguides with variable stripe length. (d) Reactive ion etching (RIE) is used to define the waveguides. Note the sample is cleaved before etching. Oxygen plasma cleaning is then used to remove the residual resist.

Starting from a silicon wafer with a  $3 \mu\text{m}$  thermal oxide on top, first, a  $\sim 100$  nm thick SiN layer is deposited (L-F H-SiN layer is used for low optical loss, see chapter 3). Then the *flash* CdSe/CdS core/shell colloidal QDs are spin-

coated on top of this SiN to form a densely packed layer with a thickness of around 50 nm, as shown in Figure 4.7(a). Later another layer of  $\sim 100$  nm thick SiN layer is deposited onto the colloidal QDs layer to encapsulate and form the full sandwich layer stack, as shown in Figure 4.7(b). Here we choose the mixed frequency SiN. This mixed frequency SiN layer is used to help match the stress between the SiN and the colloidal QDs layer to avoid cracks. This is illustrated in Figure 4.8 where we present the morphological results of SiN/QD/SiN layer stacks after the top  $\sim 100$  nm SiN deposition using L-F and M-F. It has been observed experimentally that the L-F H-SiN layer deposited on the QD surface regularly induces wrinkles with a scale of tens of microns on the entire surface of the QD film as shown in Figure 4.8(a), due to the high compressive stress in this SiN film and the stress mismatch between the QDs layer and the top SiN layer. The wrinkled surface can be cracked and peel off easily by nitrogen blowing or wetting and is useless for further processes. On the other hand, the mixed frequency deposition results in a compact stack and a neat surface as seen in Figure 4.8(b), due to tensile stress in this M-F SiN layer. Moreover, this layer stack exhibits robustness mechanically and can survive further processes such as lithography, dry etching, and wet cleaning even under ultrasonic. It is also notable that there is no observable difference between H-F and M-F SiN deposited in our PECVD system. Contact lithography is used to define the waveguide as shown in Figure 4.7(c). Finally, reactive ion etching (RIE) is used to define the waveguides, as shown in Figure 4.7(d). Note that the samples are cleaved before the RIE etching to guarantee a uniform waveguide facet, which ensures a uniform coupling between the waveguide and the collection fiber.

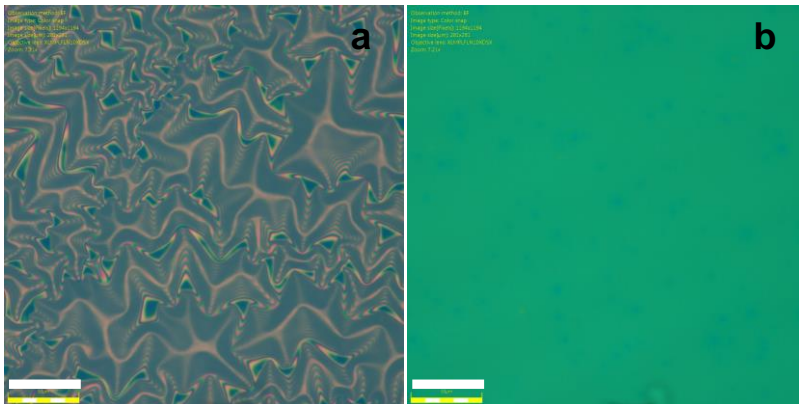


**Figure 4.8:** Optical microscope images of the surface morphologies of SiN/QD/SiN layer stack after deposition of top SiN at different PECVD frequency mode. (a) Low-frequency and (b) mixed-frequency modes. The scale bar is 50  $\mu\text{m}$ .

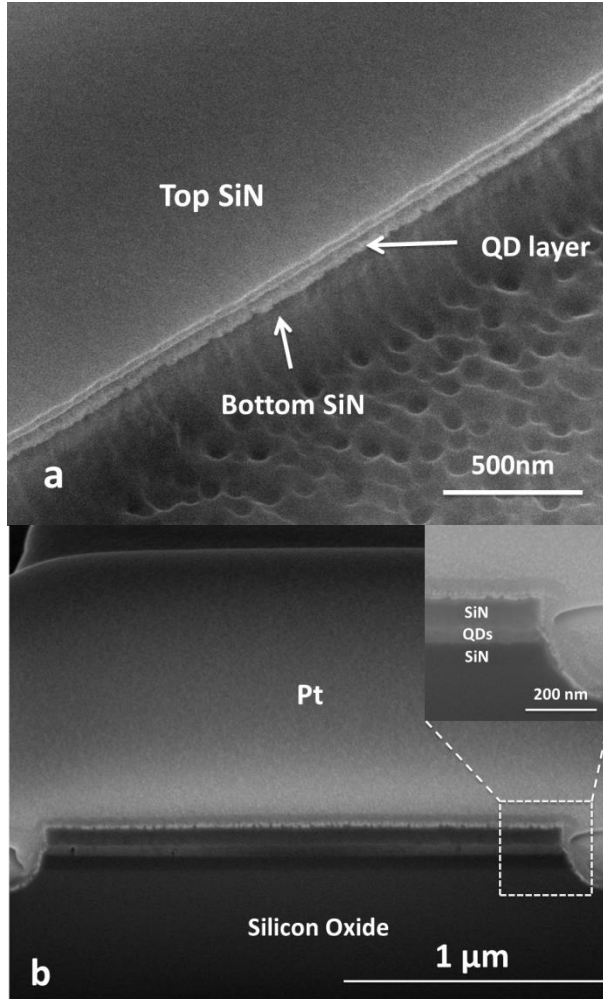


**Figure 4.9:** SEM picture of the fabricated sample. (a) The titled SEM picture showing the top SiN layer and waveguide side wall. (b) The cross section of the waveguide.

Oxygen plasma cleaning is performed after the RIE etching, to remove the residual photo resist on top of the waveguide and the samples are ready for the final measurement.

To check the quality of the SiN/QD/SiN layer stack and the etch profile, we made a scanning electron microscope (SEM) image and a cross section of fabricated samples, as shown in Figure 4.9. Figure 4.9(a) shows a tilted SEM image for the waveguide sidewall. We can clearly see the sandwich structure of the waveguide. The waveguide side wall is quite smooth and the waveguide is a little bit over etched. However, small steps at the interfaces of the different

layers can be seen. Figure 4.9(b) shows a cross section of the fabricated sample. The sample was prepared using focus ion beam milling under the protection of a Platinum (Pt) layer, deposited by electron and ion beams. It is obvious that a uniform layer of colloidal QDs with a thickness  $\sim 50$  nm is perfectly embedded between the two layers of SiN.

Figure 4.10 shows a microscope picture of the fabricated sample. The adjacent waveguides have a length difference  $10 \mu\text{m}$ . We can also note from the image that the waveguides have uniform facets, which can guarantee a constant coupling between the waveguide and the collection fiber.

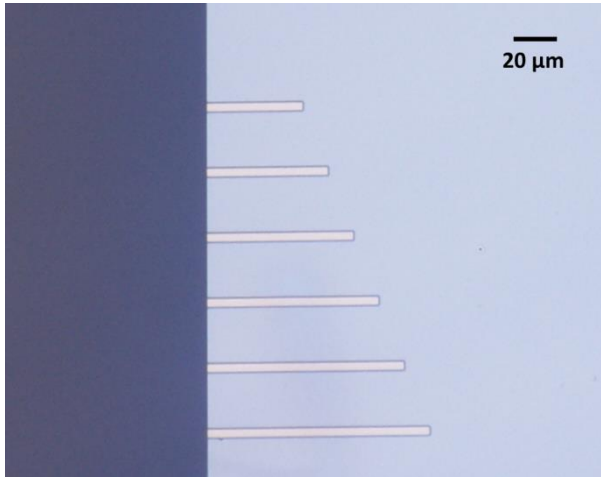


**Figure 4.10:** Microscope image of the fabricated sample. The adjacent waveguide has a length difference  $10 \mu\text{m}$ . Uniform facets can be seen from the picture.

## 4.2.2 Waveguide modal gain measurement

The characterization of the waveguide modal gain is performed with a femtosecond laser system. A Spitfire ACE laser can provide 110 fs pulsed at 1k Hz repetition rate with up to 4 mJ per pulse at 800 nm. A Beta Barium Borate (BBO) crystal is used to up convert some of the 800 nm light to 400 nm, which is then used to pump the waveguide with embedded QDs. A cylindrical lens focuses the pump laser beam into a line shape of around 8 mm by  $40 \mu\text{m}$  to pump the waveguide. The beam is adjusted to overlap with the waveguide and the light emitted from the waveguide facet is collected by a multimode fiber (NA=0.2), which guarantee a spectrally broadband collection. Figure 4.11 is the scheme of the measurement setup. Note that a neutral density filter is used to tune the pump fluence. The beam is passed through a 50/50 beam splitter and one detector at one side is used to monitor the pump fluence/intensity. The beam

has been adjusted so that it pumps perpendicular to the surface of the sample. The emission collected by the multimode fiber can be either sent to the power meter to record the intensity or to the spectrometer. Note that the transmission beam from one port after focusing is measured to determine the actual power delivered to the sample surface.

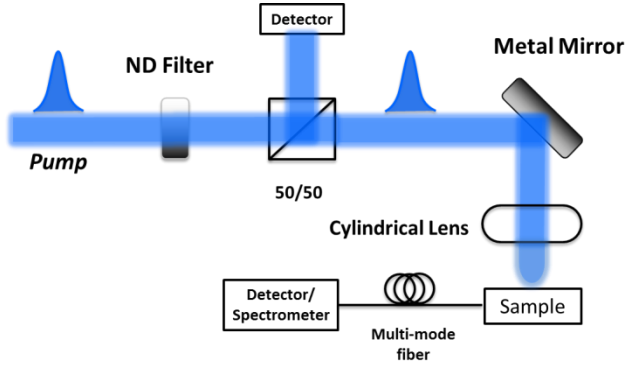


**Figure 4.11:** Measurement setup. The pump laser beam is tuned using a neutral density (ND) filter. A 50/50 beam splitter is used to split the beam and one beam is sent to a detector to monitor the beam fluence. A cylindrical lens is used to focus the beam into a rectangular shape to pump the waveguide. The emission from the waveguide is collected by a multimode fiber (NA=0.2) and send to detector to record the intensity or spectrometer to record the spectrum.

To determine the power density of the pump beam, we used a beam profiler (BC106N from Thorlabs) to check the beam power distribution after focusing by the cylindrical lens. The laser output is a Gaussian-like beam, so after the cylindrical lens, for the x-axis and y-axis, the power distribution should still be Gaussian. So the intensity distribution can be written as:

$$I(x, y) = A_x A_y e^{-\frac{x^2}{2\omega_x^2}} e^{-\frac{y^2}{2\omega_y^2}} \quad (4.4)$$

$\omega_x$  and  $\omega_y$  are the waists of the beam in the x-axis and y-axis respectively, which can be measured using the beam profiler. Figure 4.12 shows the beam intensity distribution as measured and the fitted results.

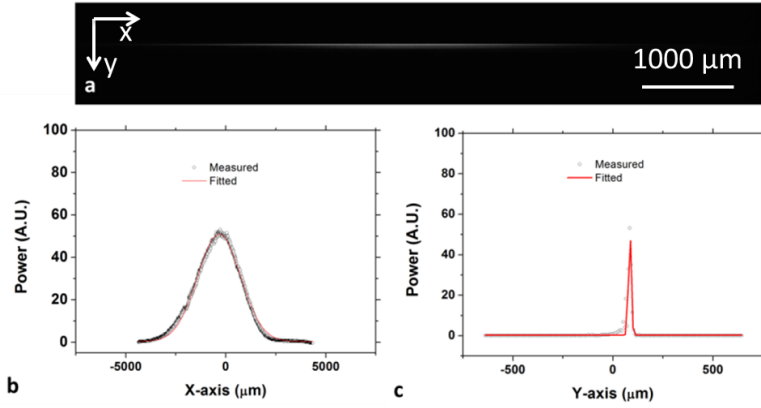


**Figure 4.12:** The power distribution of the pump beam after the focusing cylindrical lens. (a) The focused beam shape recorded by the CCD. (b) The field distribution along the X-axis. (c) The field distribution along the Y-axis.

Since  $P_{total}$  can be calculated as:

$$\begin{aligned}
 P_{total} &= \int_{-\infty}^{+\infty} I(x, y) dx dy \\
 &= \int_{-\infty}^{+\infty} A_x A_y e^{-\frac{x^2}{2\omega_x^2}} e^{-\frac{y^2}{2\omega_y^2}} dx dy = 2\omega_x \omega_y A_x A_y \pi
 \end{aligned} \quad (4.5)$$

the maximum power density in the center of the focused beam can then be written as:

$$P_{max} = A_x A_y = \frac{P_{total}}{2\omega_x \omega_y} \quad (4.6)$$

From the measurement shown in Figure 4.12, we can determine  $\omega_x$  and  $\omega_y$ , which are 1523  $\mu\text{m}$  and 10  $\mu\text{m}$ , respectively. By this beam power distribution measurement, we can link the power measured from the detector with the maximum power intensity in the center of the well-focused beam.

We will first perform a power dependence measurement with a 4  $\mu\text{m}$  wide, 600  $\mu\text{m}$  long waveguide. The measurement is performed with increasing pump fluence, whereby the emission intensity collected from the waveguide is recorded. The result is shown in Figure 4.13.

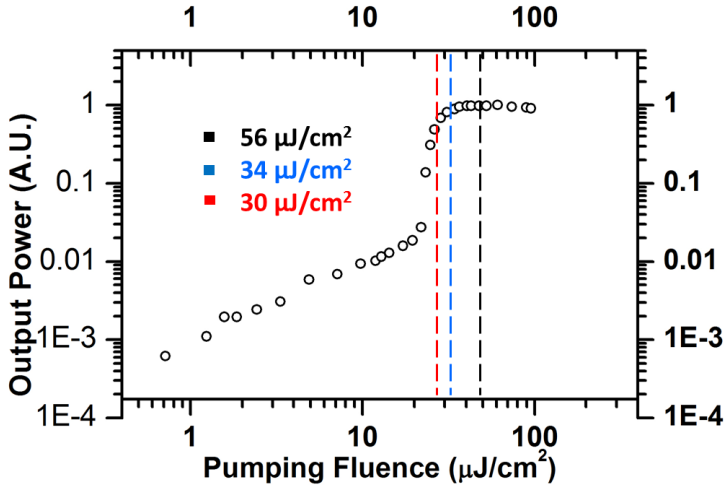


**Figure 4.13:** Power dependence measurement. The measurement is performed with a 4  $\mu\text{m}$  wide, 600  $\mu\text{m}$  long waveguide. The pump fluence for ASE onset is around 12  $\mu\text{J}/\text{cm}^2$ . The black, blue and red line indicates the pump fluence we will use for the VSL measurement (56  $\mu\text{J}/\text{cm}^2$ , 34  $\mu\text{J}/\text{cm}^2$  and 30  $\mu\text{J}/\text{cm}^2$ ).

From the measurement, a linear increase of the output power can be observed with increasing pump fluence, below the ASE onset pump fluence 12  $\mu\text{J}/\text{cm}^2$  @ 400 nm. As soon as the pump fluence reaches the ASE onset pump fluence, a super linear increase of the output can be noted, which indicates the spontaneous emission gets amplified in the waveguide and the embedded colloidal QDs show an optical gain. And with further increased pump fluence, the waveguide output saturates. The reason is that the ASE intensity itself depletes the excitons, reducing the gain as the signal intensity builds up along the amplification axis. In Figure 4.13, we also indicate the three different pump intensities chosen to do the VSL measurement.

Figure 4.14 shows the output spectrum collected from this 4  $\mu\text{m}$  wide 600  $\mu\text{m}$  long waveguide with a pump fluence of 54  $\mu\text{J}/\text{cm}^2$  @ 400 nm. The spectrum is approximately centered at 632 nm and exhibits a full width at half maximum (FWHM) of 6.5 nm. This is clearly narrowed down compared to the low fluence spontaneous emission spectrum (Figure 4.2), also indicative of ASE. We also note that the ASE peak develops at the high energy side of the spontaneous PL peak. The short wavelength gain in Figure 4.5 comes from the higher order multi-excitons in the QDs. We cannot observe these gain bands probably because the PECVD process damages the QDs a little bit, thus we can not have these high order multi-exciton gains.

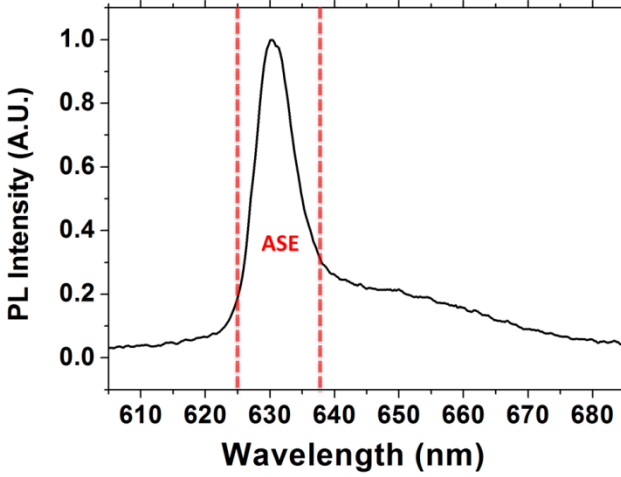


**Figure 4.14:** The emission spectrum of a 4  $\mu\text{m}$  wide 600  $\mu\text{m}$  long waveguide with pump fluence 54  $\mu\text{J}/\text{cm}^2$  @ 400 nm.

Figure 4.15 shows the measured output power versus the waveguide length with 3 different pump fluences. The figure shows a pronounced super-linear rise in emission intensity for waveguides longer than  $\sim 280$   $\mu\text{m}$  and the emission saturates for waveguides exceeding  $\sim 400$   $\mu\text{m}$ .

For traditional VSL measurement, there is a negligible reflection from the backside of the waveguide, hence, we can simply use the equation:

$$I = A_0 \frac{e^{gL} - 1}{g} \quad (4.7)$$

where the  $g$  is the modal gain, which can easily be fitted from the exponential increasing region. However, for our waveguide based VLS measurement, there is still some small reflection coming from the back facet and this reflection will get amplified and collected. So we should modified equation 4.7 by introducing  $R$ , which is the reflection of the back facet of the waveguide. With this  $R$ , the equation can be re-written into:

$$I = A_0 \left[ \frac{e^{gL} - 1}{g} + \frac{R}{g} e^{2gL} (1 - e^{-gL}) \right] \quad (4.8)$$

Here, for  $R$  varying from 0 to 5% (for a perfect facet reflection), we could fit the measured result with a modal gain of around 279-169  $\text{cm}^{-1}$  @ 30  $\mu\text{J}/\text{cm}^2$ , 340-206  $\text{cm}^{-1}$  @ 34  $\mu\text{J}/\text{cm}^2$  and 350-212  $\text{cm}^{-1}$  @ 56  $\mu\text{J}/\text{cm}^2$  respectively. For this waveguide structure, the confinement factor is  $\Gamma=0.31$  for the fundamental TE mode profile, which has been shown in Figure 4.15. The confinement factors are

0.313, 0.314, 0.316, 0.318, 0.321 and 0.325 for the TE<sub>1</sub>, TE<sub>2</sub>, TE<sub>3</sub>, TE<sub>4</sub>, TE<sub>5</sub> and TE<sub>6</sub> higher order modes respectively. We can translate our modal gain coefficient to a compact layer gain coefficient, which is around 900-545 cm<sup>-1</sup> @ 30 μJ/cm<sup>2</sup>, 1097-665 cm<sup>-1</sup> @ 34 μJ/cm<sup>2</sup> and 1129-684 cm<sup>-1</sup> @ 56 μJ/cm<sup>2</sup>. Considering also a filling factor 0.5, which takes into account the organic ligands at the surface of the colloidal QDs, for 5% reflection, the pure material gain coefficient is derived to be around 1090 cm<sup>-1</sup> @ 30 μJ/cm<sup>2</sup>, 1330cm<sup>-1</sup> @ 34 μJ/cm<sup>2</sup> and 1368 cm<sup>-1</sup> @ 56 μJ/cm<sup>2</sup>, which agree quite well with the material gain obtained from the TAS measurement.

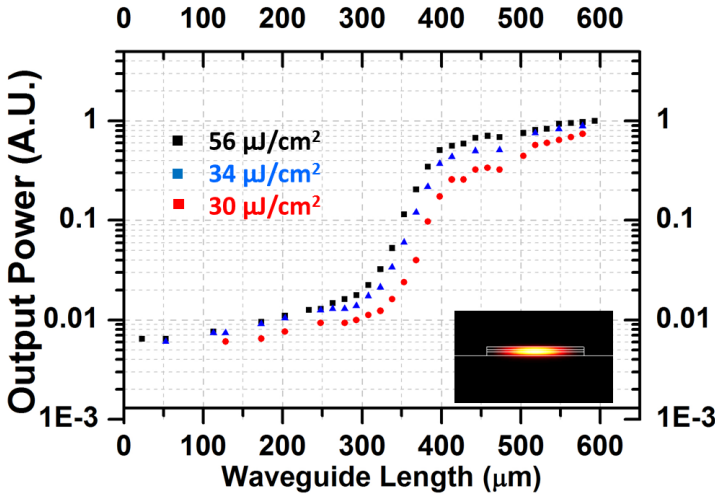


**Figure 4.15:** Measured output power versus the waveguide length with 3 different pumping fluences. The inset is the mode profile of the fundamental TE mode of the waveguide structure.

### 4.3 DFB laser design, fabrication and characterization

From the last section, we have demonstrated the hybrid colloidal QDs SiN waveguide can still show ASE with femtosecond pulse laser pump. That is a great step, as it shows our heterogeneous integration platform for colloidal QDs can not only preserve the photoluminescence properties but also preserve the light amplification properties. Hence, it is now straightforward to build micro optical cavities based on these waveguides to achieve on-chip lasers. A DFB type microcavity is an attractive choice, since it can provide single mode lasing with relatively low lasing threshold. In this section, we present the design, fabrication and characterization of a DFB type on-chip colloidal QD laser.

### 4.3.1 Laser cavity design

The DFB lasers were fabricated starting from a 75 nm/50 nm/ 90 nm SiN/QD/SiN sandwich layer, details will be given below. First order gratings will be defined with a  $\lambda/4$  phase shift section inserted in the middle to form the laser cavity. To optimize the grating parameters (etch depth, period), 3D finite-difference time-domain (FDTD) simulations were carried out, from which we could determine the grating Bragg wavelength and stopband. The index of the SiN layer and the QD layer were measured using ellipsometry and found to be  $n_{\text{SiN}}=2.0$  and  $n_{\text{QD}}=1.9$ . For the preliminary scan, the grating etching depth is fixed to 35 nm and a 50% duty cycle was assumed. The waveguide width was set at 2  $\mu\text{m}$ .

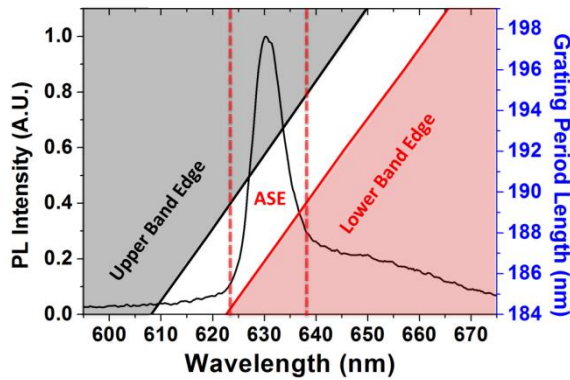


**Figure 4.16:** The simulated stop band of the grating has been shown in the picture as the region between the grey and red areas. The ASE spectrum has been inserted as a comparison for the grating periods choosing.

Figure 4.16 shows the calculated grating band gap versus period. The gray and the red regions denote the upper and lower stopband areas respectively. The simulated photonic band gap is around 14 nm. The spectrum of the ASE from a waveguide with an identical SiN/QD/SiN stack is also inserted to compare. Clearly, we should carefully choose the grating period to ensure that the photonic band gap overlaps with the measured colloidal QDs ASE spectrum. Based on this argument, a grating period of 188nm was chosen.

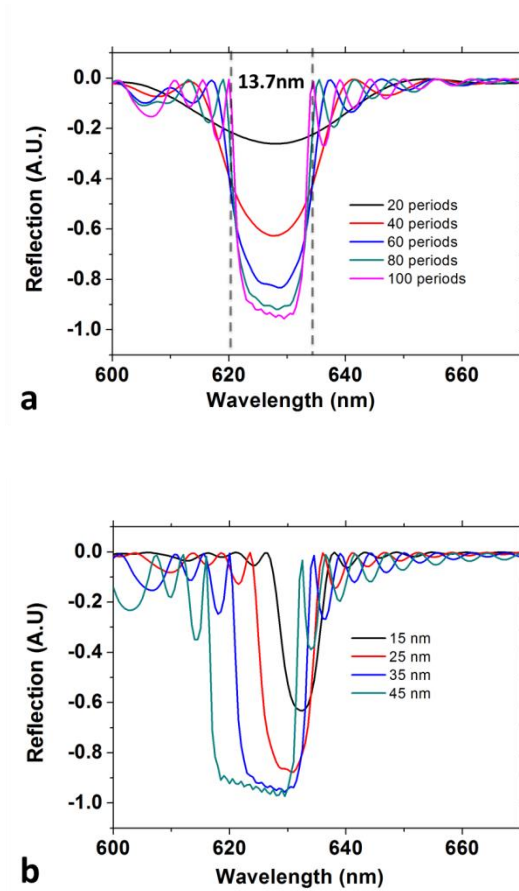


**Figure 4.17:** DFB optical cavity design. (a) The reflection spectrum with different number of periods. The grating period is 188 nm and the etching depth is 35 nm. The stopband is around 13.7 nm with 100 periods of grating. (b) The reflection spectrum with different etching depth. The period is 188 nm and the number of periods is 100. With increased etching depth, the grating is becoming stronger, with higher reflection and wider stopband.

The optimization of the DFB cavity is done by further scanning the device parameters. The reflection spectra with different number of periods have been simulated and the results are shown in Figure 4.17(a). The period is fixed to 188 nm and etching depth is fixed to 35 nm. The simulated results indicate that with this grating period and etching depth, 100 periods can already provide around 95 % reflection. The stopband is 13.7 nm wide. Figure 4.17(b) shows the reflection with different etching depth. The period has been fixed to 188 nm with 100 periods. The simulation shows that with increased etching depth, the

reflection becomes stronger and the stopband becomes wider, as expected from standard grating theory.

### 4.3.2 Fabrication process

Figure 4.18 shows the fabrication flow of the DFB laser. The layer stack with 75 nm/50 nm/ 90 nm SiN/QD/SiN sandwich layer is prepared on top of a silicon wafer with a 3  $\mu\text{m}$  thermal oxide layer grown on top. Like the waveguide samples prepared for the VSL measurement, the bottom SiN layer is deposited with the L-F H-SiN recipe, and the top SiN layer is deposited with M-F H-SiN recipe. Next, electron-beam (Ebeam) lithography with AR-P 6200.09 resist, is used to define the DFB grating, as shown by Figure 4.18(b). Through  $\text{CF}_4/\text{H}_2$  RIE, the grating pattern is transferred to the top SiN layer, which is illustrated by Figure 4.18(c), after which the residual resist is stripped using oxygen plasma. Finally, the waveguide ridge is defined using standard contact lithography and a second RIE process like Figure 4.18 (d).

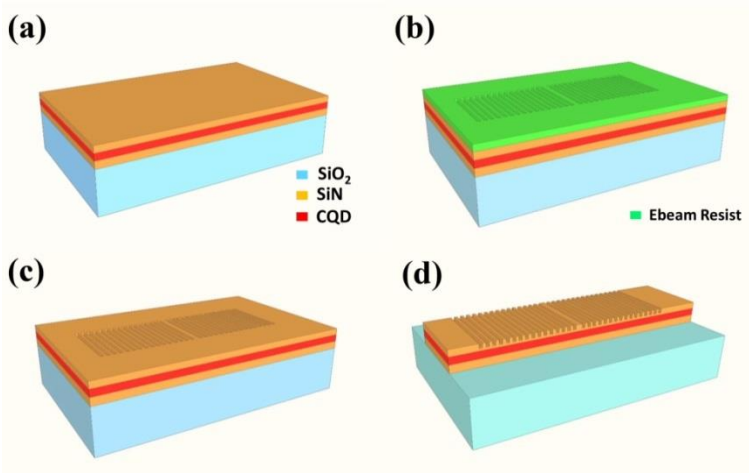


**Figure 4.18:** Fabrication overview. (a) First, an L-F H-SiN layer is deposited on a silicon substrate with a 3  $\mu\text{m}$  thermal silicon oxide grown on top. Next, the QD layer is spin coated on top and another M-F H-SiN layer is deposited on the QD layer to encapsulate the QDs and form the hybrid SiN/QD/SiN stack. (b) Electron beam lithography to pattern the grating. (c) RIE etching to transfer the grating patterning to the top-SiN layer. (d) Contact lithography and RIE etching to pattern the waveguide.

To take into account the uncertainties in the fabrication process, we fabricated DFB lasers with grating period varying from 180 to 195 nm on the same chip. After the fabrication, we performed SEM to check the quality of the fabricated

devices. Figure 4.19 shows the tilted side SEM and a cross section taken in the phase shifter area. From Figure 4.19(a), we could see a well patterned grating on top of the waveguide with a phase shifter sitting in the middle. Figure 4.18(b) shows a grating with period 188 nm and etching depth around 35 nm, showing the value targeted for during the design is well achieved. At the back-side the laser are connected to a waveguide without grating, which ensures low residual reflections. The laser cavity length is approximately 100  $\mu\text{m}$ .

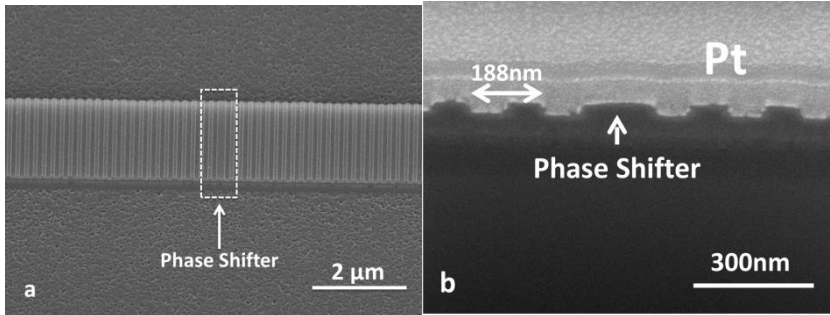


**Figure 4.19:** SEM graph of fabricated samples. (a) Tilted SEM picture near the phase shifter region. We could see a well patterned grating on top of the waveguide. (b) FIB cross section picture taken in the phase shifter region. The grating period is 188 nm and the etching depth is around 35 nm as designed.

### 4.3.3 Laser characterization

#### 4.3.3.1 Femtosecond laser pump

We first characterize the DFB lasers' properties using the femtosecond laser setup which has been previously used for the waveguide VSL gain measurement. The pump beam is still focused with a cylindrical lens and used to pump the laser. The emission from the waveguide facet was collected by a multimode fiber for analysis. The light (in)-light (out) curve for lasers with 188 nm grating period has been shown in Figure 4.20 (a). The curve shows a clear threshold around  $12 \mu\text{J}/\text{cm}^2$  @ 400 nm. Figure 4.20 (b) shows the evolution of the spectral width (FWHM) under the different pump intensity. The spectral narrowing can be observed, which also indicates the device is working in the lasing region.

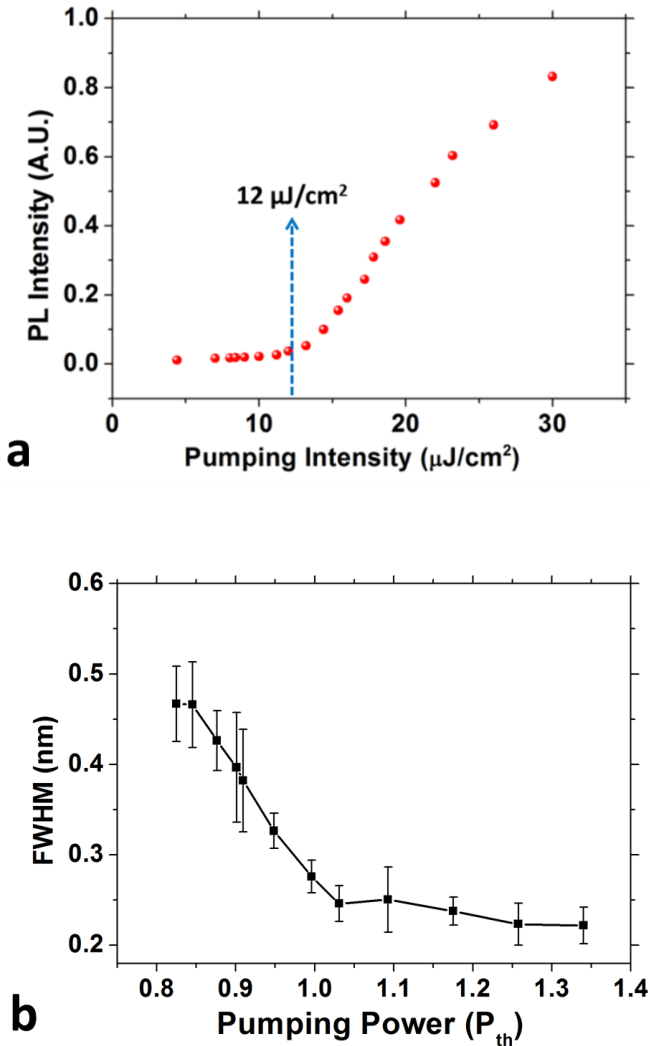


**Figure 4.20:** (a) Light (in)-light (out) measurement on double linear scale for DFB laser with 188nm period. The pump laser is the same femtosecond laser used in the gain measurement. (b) The evolution of the spectral width (FWHM) under the different pump intensity. The inset is the spectra under different pump fluence. Note that the noise level is around 600.

Figure 4.21(a) shows the emission spectra of three devices with varying grating period (pump fluence =  $15 \mu\text{J}/\text{cm}^2$  @ 400 nm). The ASE spectrum taken from a waveguide without grating is overlaid on top for comparison. The measured

spectra show the lasers are operating in a single longitudinal mode, with a high side mode suppression ratio. The three lasers exhibit 1 nm difference in grating period, which results in a 2.6 nm shift in the measured spectra, in line with the simulations ( $d\lambda/d\Lambda=2.64$ ). The lasing peaks have a 0.2 nm FWHM and fall within the ASE envelope.

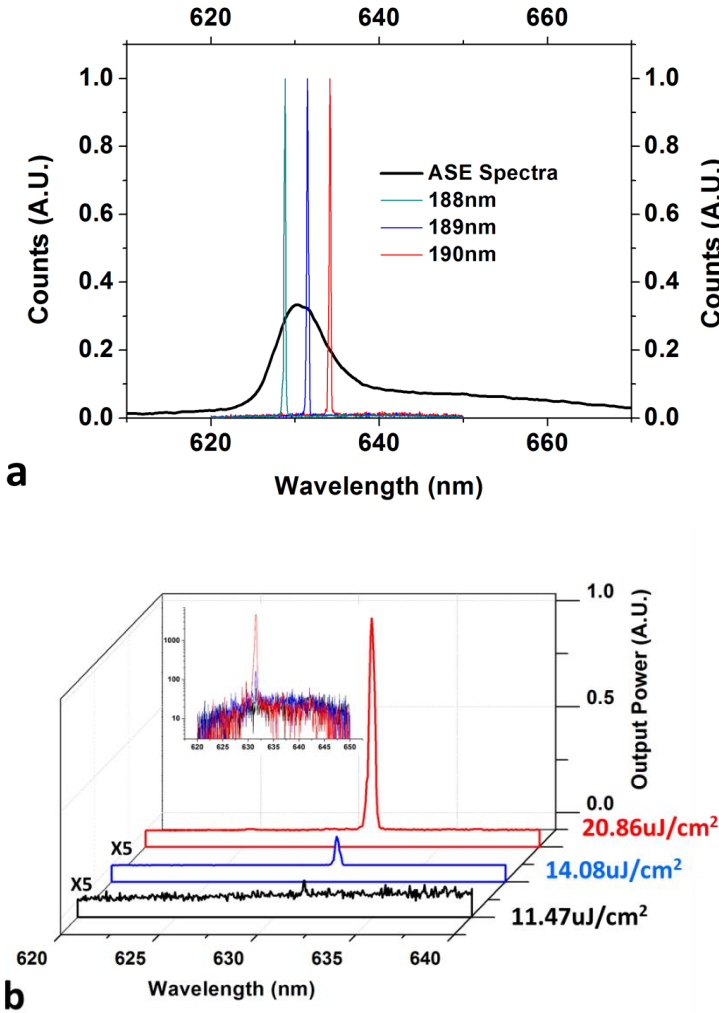


**Figure 4.21:** (a) Spectra measured from an unpatterned waveguide (black) and DFB lasers with different grating periods (colored). (b) Spectra measured from laser with 188 nm period at different pump fluence. The inset is the log-scale measured spectra under different pump fluence.

Figure 4.21b shows the spectra of the laser with 188 nm period at different pump fluence. The inset is the log-scale measured spectra under different pump fluence. The spontaneous emission stays the same with different pump fluence. Figure 4.22 shows the captured microscope picture of the laser under and above threshold. The left picture is the picture captured with pump power under the laser threshold. The right picture is the picture captured with pump power above the laser threshold. The scattered emission from the waveguide facet can be clearly seen from the right picture, which indicates the output from the laser.

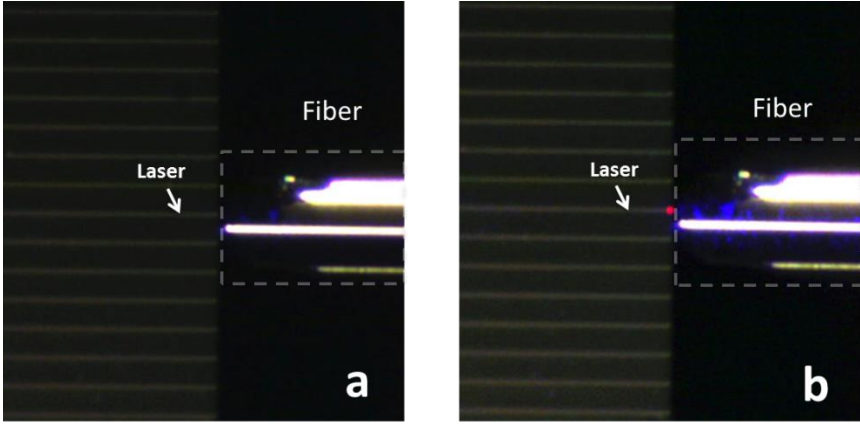


**Figure 4.22:** Captured microscope pictures of the laser under/above the threshold.  
(a) Under lasing threshold. (b) Above lasing threshold.

For the waveguide patterning for the DFB laser, we have also tried to pattern the waveguide with shallow etching, which can avoid etching through the QDs layer. The purpose is to reduce the sidewall roughness, which leads to lower internal losses to obtain a higher Q for the cavity. However, in this case, the embedded QDs in the trench area provide strong background ASE, when the laser is pumped, which brings troubles for the lasing characterization.

Some of the lasers with wider waveguide width ( $> 3 \mu\text{m}$ ) and longer cavities length ( $> 300 \mu\text{m}$ ) show multi-mode lasing with high pump fluence, which can be seen from the spectrum in Figure 4.23. Multi peaks can be seen from the spectrum, which indicates multi-mode lasing. For the lasers with wide waveguide width, this multimode lasing can be attributed to the multi-mode supported by the wider waveguide [17]. With narrowed waveguide ( $< 2 \mu\text{m}$ ) laser design, this multimode lasing is suppressed. For the long cavity length laser, the multimode lasing can be explained with lasing from different regions of the long cavities. This phenomenon comes from the high  $\kappa$  from the grating (see section 4.4.3.2). With the high  $\kappa$  long cavity, the laser can lase simultaneously in the different region of the grating which leads to a multimode

lasing. This multimode lasing can be eliminated with optimized laser cavity length.

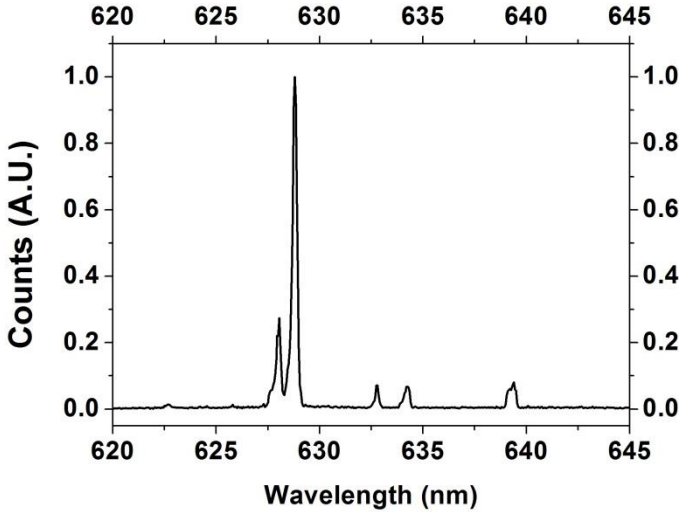


**Figure 4.23:** Multimode lasing with multi-peaks in the spectrum. The laser's waveguide width is 4  $\mu\text{m}$  width with a 400- $\mu\text{m}$  cavity length. The grating period is 188 nm.

### 4.3.3.2 Nanosecond laser pump

To further investigate the laser performance, we used a Q-switched frequency doubled Nd:YAG laser (532 nm) with a 7 nanosecond pulse width and a 938 Hz repetition rate for pump. Again, the laser light was focused with a cylindrical lens to a rectangular pattern to pump the DFB lasers.

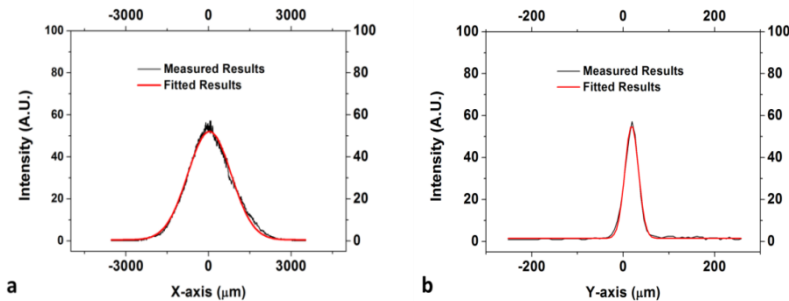


**Figure 4.24:** Beam calibration for the nanosecond laser along x-axis (a) and y-axis (b). The fitted results shows the  $\omega_x$  is 1115  $\mu\text{m}$  and  $\omega_y$  is 26  $\mu\text{m}$ .

The well-focused beam's power distribution has been again measured to accurately estimate the beam center's power density. The measured results have

been shown in Figure 4.23. By extracting the data from the beam field distribution, we could estimate a beam size  $\sim 3.15$  by  $0.07$  mm<sup>2</sup>.

Figure 4.24 shows the power emitted from the cleaved facet measured as a function of pump fluence, respectively on a double linear (Figure 4.24(a)) and a double logarithmic (Figure 4.24(b)) scale. The linearly scaled graph shows a clear lasing threshold at  $270$   $\mu\text{J}/\text{cm}^2$ . Taking into account the pulse length ( $7$  ns), the equivalent CW pump fluence (power per pulse divide by the pulse time width) is then  $39$  kW/cm<sup>2</sup>. The experimental data of Figure 4.24(b) was fitted to a static rate equation model [18-20], from which, a spontaneous emission factor ( $\beta$ ) of  $0.009$  was extracted.

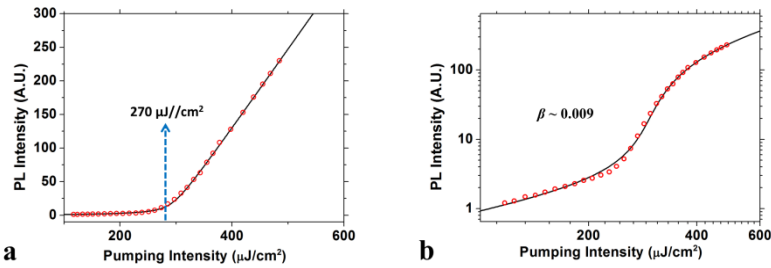


**Figure 4.25:** (a) The light(in)-light(out) curve on a double linear scale, with an indication of the lasing threshold around  $270$   $\mu\text{J}/\text{cm}^2$ , which has an equivalent CW power density of  $39$  kW/cm<sup>2</sup>. (b) The light(in)-light(out) curve on a double log-scale with rate equation fit (black solid). A spontaneous emission factor ( $\beta$ )  $0.009$  is extracted.

The DFB laser's  $\kappa L$ , where  $\kappa$  is the coupling coefficient and  $L$  is the length of the DFB cavity, is a measure for the strength of the grating, was calculated to be  $16.7$ , using the equation [17]:

$$\kappa L = \sqrt{\left(\frac{\Delta\lambda \cdot \pi \cdot n_{eff} \cdot L}{\lambda_{bragg}^2}\right)^2 - \pi^2} \quad (4.9)$$

where  $\Delta\lambda$  is the stopband width, which can be deduced from the spontaneous emission spectrum with and without grating as shown in Figure 4.26,  $\lambda_{bragg}$  is the grating Bragg wavelength and  $n_{eff}$  is the effective index of the waveguide. The stopband is obtained from the measured spectrum deducted with the normalized ASE spectrum. The large  $\kappa L$  indicates our DFB grating provides strong feedback, contributing to the laser's low threshold fluence.

For this DFB cavity, the cavity photon lifetime can be defined using the equation below [17]:

$$\frac{1}{\tau_{ph}} = [\alpha_{int} + 4 \cdot \kappa \cdot e^{(-\kappa \cdot L)}] \cdot v_g \quad (4.10)$$

whereby  $v_g$  is the group velocity. The above equation indicates the cavity photon lifetime is dominated by the internal losses  $\alpha_{int}$ . These could include waveguide scattering losses but also losses due to photon induced intraband transitions. We can estimate  $\alpha_{int}$  to be of the order  $2.5 - 20 \text{ cm}^{-1}$ , equivalent with a photon lifetime of  $30 - 3 \text{ ps}$ .

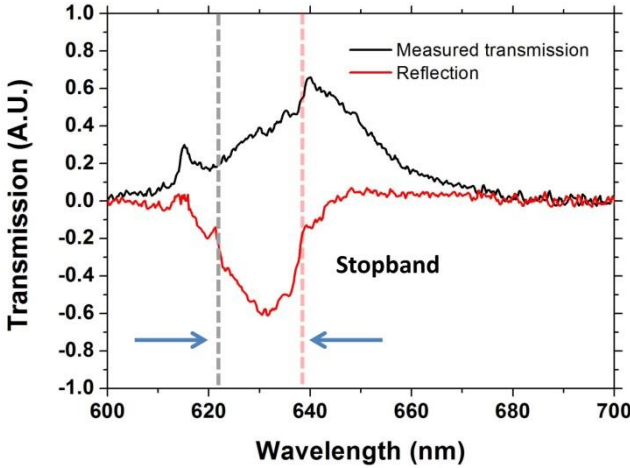


**Figure 4.26:** Below threshold spontaneous emission spectrum from DFB-laser before (black) and after (red) normalizing with spectrum of unpatterned waveguide.

### 4.3.4 Results analysis

The measurement in section 4.1 shows the *flash* CdSe/CdS core/shell colloidal QDs we used for our laser exhibit a  $2 \text{ ns}^{-1}$  biexciton decay rate, corresponding to a 500 ps biexciton lifetime. Compared to this biexciton lifetime, our 7 ns pump actually can be considered as quasi-CW pumping. This observation allows us to use the model developed by Park YS *et al.* elaborated in Chapter 2 to analyze and predict the CW pump threshold of our device. This model links the average QD occupancy  $\langle N^* \rangle$  to the pump fluence  $J$  as:

$$\langle N^* \rangle = \frac{J\sigma\tau_x + 2(J\sigma)^2\tau_x\tau_{xx}}{1 + J\sigma\tau_x + (J\sigma)^2\tau_x\tau_{xx}} \quad (4.11)$$

where  $\tau_x$  and  $\tau_{xx}$  are the single exciton and biexciton lifetimes and  $\sigma$  is the absorption cross section. For the QDs used, the single exciton lifetime is 26.8 ns as was derived in section 4.1. From the gain decay rate we estimated the biexciton lifetime to be  $\sim 500 \text{ ps}$ . The absorption cross section is  $2.75 \times 10^{-15} \text{ cm}^2$  @ 532 nm as mentioned in the previous section. By using this data, and assuming a 30 ps cavity photon lifetime, we can estimate a minimum lasing threshold pump fluence around  $10.9 \text{ kW/cm}^2$ . If the cavity photon lifetime

reduces to 3 ps the theoretical lasing threshold pump fluence increases to 46.2 kW/cm<sup>2</sup>. If we take into account that a fraction of the incident pump gets reflected by the layer interfaces, our observed equivalent CW pump intensity of 39 kW/cm<sup>2</sup> falls right within this range. Figure 4.27 shows the effect of biexciton lifetimes  $\tau_{xx}$  on the lasing threshold. The plot indicates a rapid increase in the threshold intensity with decreasing biexciton lifetime.

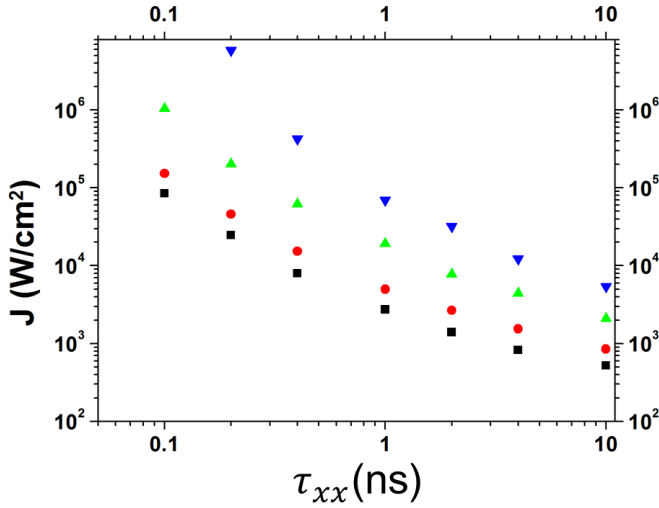


**Figure 4.27:** Effect of biexciton lifetime on lasing threshold. The CW lasing threshold is plotted as a function of biexciton lifetime  $\tau_{xx}$  with the 532 nm wavelength pump. Different cavity lifetimes are plotted with different colors:  $\tau_c=0.1$  ns (black);  $\tau_c=0.01$  ns (red);  $\tau_c=0.002$  ns (green);  $\tau_c=0.001$  ns (blue).

Previous reports showed colloidal QD lasers operating under nanosecond [7-8, 21] and microsecond excitations [22]. Recently, CW-pumped lasing has been demonstrated from a device consisting of a colloidal QD coating on a photonic crystal DFB structure [23]. Our work goes beyond these results by demonstrating a truly integrated QD laser operating under nanosecond pulsed excitation. This is altogether a remarkable feat as the 2 ns<sup>-1</sup> decay rate for the gain makes 7 ns pump almost equivalent to quasi-CW operation. Theoretical modelling built from previous work [14] agrees well with our experimental results. There are several aspects that allow our DFB lasers to exhibit a low lasing threshold and to operate in a quasi-CW pump regime. Most importantly, the *flash* quantum dots we are using have a suppressed non-radiative Auger recombination rate, which is now well understood to be essential for lasing applications [14, 23]. Moreover, our optimized embedding process does not only preserve the emission properties of the QDs, but also enhances the coupling

between the QD emission and the optical mode of the cavity. In this way, by combining the QDs with a SiN PIC platform, on-chip optical micro-cavities with compact size and low optical loss are achieved.

To further reduce the laser's lasing threshold, there are several ways that we can work with. One is to use QDs with further increased biexciton lifetime. This could still substantially reduce the lasing threshold. The other one is using optical cavities with even higher optical Q [24]. Also some other techniques might further improve the QD laser performance. Using inorganic-halide-capped QDs *et al* [22] could increase the packing density in the active layer, resulting in a higher modal gain and better thermal conductivity. Alternatively a ZnS-shell could be used to cap the current QDs and better preserve their optical properties after encapsulation into the SiN layer stack. It may also be relevant to provide on-chip heat sinking structures to avoid local heating that quenches the QD emission.

Even without these possible improvements, the laser equivalent CW threshold that we currently observe is at the same level as that of III-V semiconductor lasers epitaxially grown on silicon [9]. This opens strong prospects in terms of CW operation and, consequently, an extended application potential. One could now realistically envision CW-pumped on-chip integrated lasers using colloidal quantum dots as the gain medium. The intrinsic combination with the mature SiN-waveguide platform then immediately opens the path towards more complex devices such as tunable lasers and arrays of single mode lasers or integration with passive structures such as on-chip spectrometers. This in turn will enable applications such as on-chip biosensing, absorption spectroscopy and Raman spectroscopy that now require off-chip sources and complex optical coupling approaches [25,26].

## 4.4 Gain-coupled DFB laser design, fabrication and characterization

For many practical applications, stable single mode lasers are preferred. In this case, the favorite candidates are DFB lasers, in which the optical feedback required to initiate laser oscillation is provided by coherent reflection from periodic variation of the refractive index. The laser oscillations will occur only at wavelengths consistent with the Bragg condition, which exhibits a considerable spectral selection. In the coupled wave model used first by Kogelnik and Shank [26] to analyze the DFB laser operation near threshold, a parameter of major importance is the coupling coefficient  $\kappa$ . This parameter  $\kappa$ , which describes the amount of power transferred between the two contra-directional waves propagating along the laser, determines both the threshold gains and the oscillation frequencies of the longitudinal modes excited within

the laser. Kogelnik and Shank presented and discussed numerical results which describe the properties of these modes in two special cases. One is index-coupling, when the real part of the refractive index varies periodically and  $\kappa$  is real. The other one is gain-coupling, when there exists a periodic variation of the gain and  $\kappa$  is imaginary.

In real-world devices, one problem of the perfectly AR (anti-reflection)-coated index-coupled DFB laser is that it supports two degenerate modes, lying symmetric around the Bragg frequency [26]. One solution to this problem is the use of non-AR coated facets. This method, however, causes a yield problem associated with the uncertainty of the facet phases [27]. Another widely used solution is the introduction of a  $\lambda/4$  phase shifter in the center of the cavity. For perfect AR coatings, these lasers show a high yield. A drawback with this phase shifter technique, however, is the high level of spatial hole burning (SHB) caused by the phase shifter [28]. This can be reduced by modulation of the stripe width [29] or introducing multiple phase shifters. The latter type of laser has been extensively studied for various facet reflectivities and position of the phase shifters in [30].

According to coupled mode theory, a gain-coupled optical feedback laser works better than an index-coupled optical feedback laser and is predicted to operate more stable in a single longitudinal mode. Such gain-coupled optical feedback is immune to facet reflection. Also, it has been shown that even a small degree of gain coupling enhances the performance considerably in terms of threshold gain difference between the different modes and removes the degeneracy of the AR-coated DFB lasers. Moreover, complete elimination of SHB is possible. The consideration of SHB is important because this nonlinearity has a strong effect on various performance aspects of DFB lasers. It has been found both experimentally [28] and theoretically [31] that lasers can become multi-mode at low and moderate power levels due to strong SHB. Moreover, it can give rise to a less flat FM response [32], an increased linewidth [33], and nonlinearities of the LI curve. The latter property is crucial in optical communication analog systems where low harmonic distortion is desired [34].

The standard fabrication of gain-coupled DFB lasers involves patterning periodical structures into the gain layer. For traditional III-V materials, the etching required to form these periodical gain sections will introduce defects and these defects will degrade the performance of the gain material of the laser. Some gain-coupled III-V DFB lasers are experimentally demonstrated with active layers growing on the surface of the pre-patterned gratings, as shown in Figure 4.28 [35]. However, several epitaxy steps are needed, which leads to a complicated fabrication process.

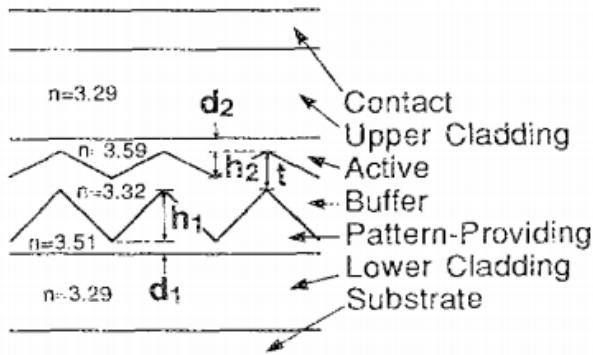
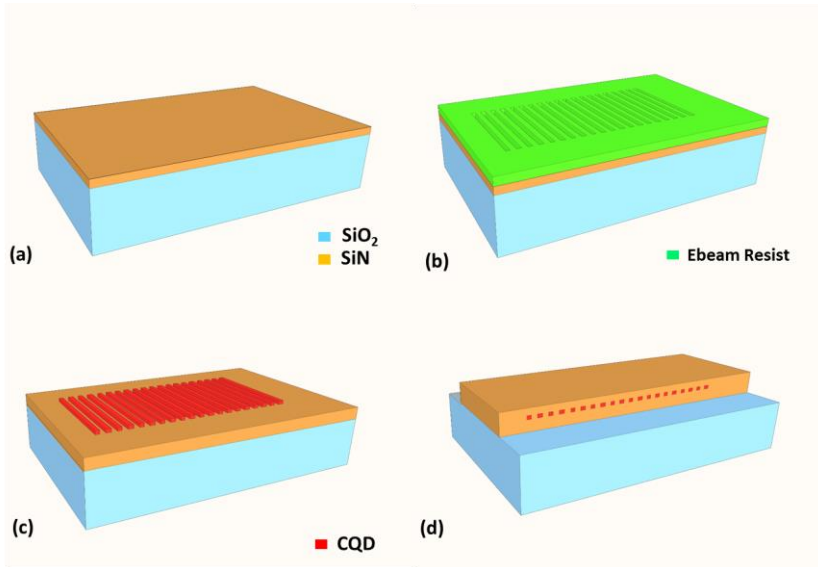


**Figure 4.28:** Schematic drawing of the longitudinal cross section of the gain-coupled DFB laser structure. Adapted from ref [35].

The use of colloidal QDs as the gain material can overcome this problem. As we mentioned at the beginning of this chapter, they are nanocrystal materials synthesized in a solution phase at low cost. They can be easily deposited on top of a substrate without expensive epitaxial deposition techniques. Simple traditional lift off methods can be used to pattern the colloidal QDs layers on top of the substrate surface with high accuracy. In this section, we, therefore, present the fabrication and characterization of a gain-coupled DFB type on-chip colloidal QDs laser.

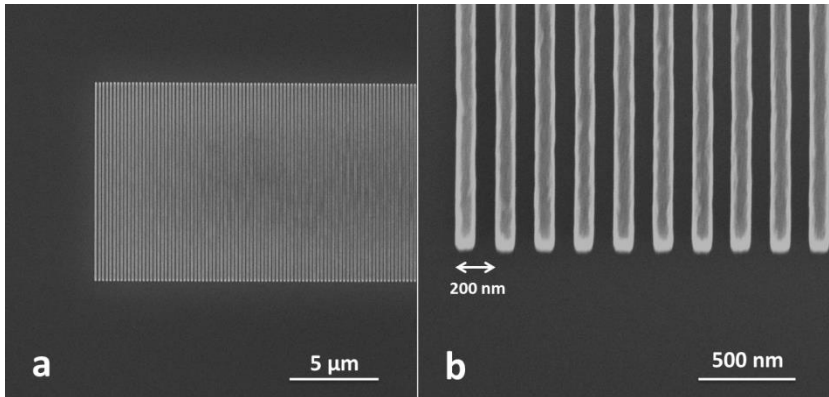
#### 4.4.1 Fabrication process

Figure 4.29 shows the fabrication flow of the gain-coupled DFB laser. Like the previously index-coupled DFB laser, a layer of 100 nm L-F H-SiN is deposited on top of a silicon wafer with 3  $\mu\text{m}$  thermal oxide grown on top. Later, Ebeam is used to pattern a grating for the QD layer lift off process. Note that there is no phase shifter in the middle of the grating. Then a compact colloidal QD layer is spin-coated on top of the patterned grating, followed by a lift off process. The layer thickness is around 50 nm. A periodically structured gain layer is formed. Another layer of 100 nm M-F H-SiN is deposited on top to encapsulate the colloidal QDs and is followed by standard contact lithography and a second RIE process to define the waveguide.



**Figure 4.29:** Fabrication overview. (a) First, an L-F H-SiN layer is deposited on a silicon substrate with a 3  $\mu\text{m}$  thermal silicon oxide grown on top. (b) Ebeam is used to pattern the grating for the lift off process. (c) Colloidal QD layer is spin-coated on top of the sample followed by a lift off process. Periodically structured gain layer is formed. (d) Contact lithography and RIE etching to pattern the waveguide. The gain sections are buried in the waveguide periodically to form the gain-coupled DFB laser.

We first used a silicon wafer to test the lift off process with the spin-coated colloidal QD layer. AR-P 617.06 from Allresist GmbH is used as the Ebeam resist. The resist is 290 nm thick, with 4000 rpm spin coating. After the development, a colloidal QD layer is spin coated on top. The sample has been put into acetone for around 8 hours to remove the Ebeam resist. SEM is used to check the lift off process quality afterwards. Figure 4.30 shows the SEM graph of the sample. Figure 4.30(a) shows the overall look of the patterned grating after the lift off. A well patterned grating can be seen. A close check of the detailed grating pattern is presented in Figure 4.30(b). The grating period is 200 nm as designed. A clean substrate can be seen without any residual colloidal QDs on the grating trench area, indicating a good lift off process.



**Figure 4.30:** SEM quality checking for the colloidal QDs layer lift off. (a) The overall of the patterned grating. (b) The detail check of the patterned grating. A 200 nm period is achieved as designed with no residual colloidal QDs in the grating trench region.

We later use the same lift off process to pattern colloidal QDs layer on top of SiN for the gain-coupled DFB laser. To take into account uncertainties in the fabrication process, we fabricated devices with grating period varying from 176 to 190 nm on the same chip. The laser cavity is around 100 μm long. Figure 4.30 shows a top view and a cross section of the fabricated sample. Figure 4.30(a) is the tilted sidewall SEM image of the fabricated 4 μm wide laser. The trench area can be seen to be non-uniform, which comes from the different etching

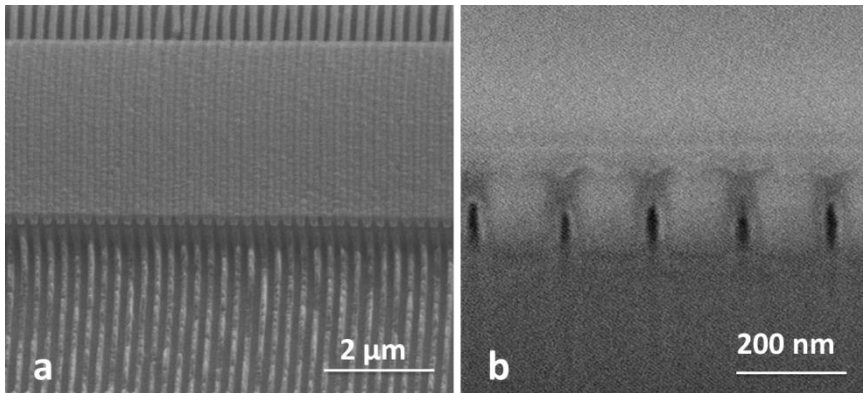


**Figure 4.31:** SEM picture of the fabricated gain-coupled DFB laser. (a) The tilted sidewall of the fabricated sample. (b) The cross section picture of the fabricated sample.

speed in the regions with and without embedded colloidal QDs. The top surface of the laser is also not very smooth, which comes from the height difference

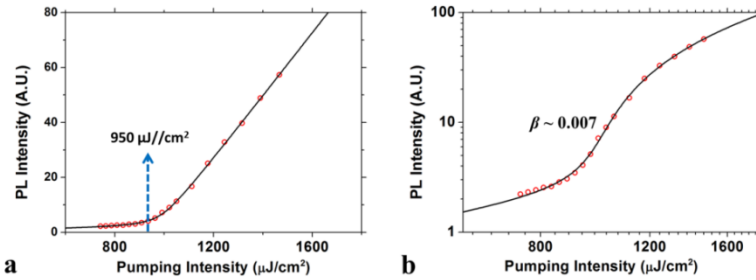
introduced by the embedded colloidal QDs. Figure 4.30(b) shows the cross section of the fabricated DFB laser. Gaps between the colloidal QDs layer can be seen, which indicates the SiN layer did not fill in the grating trench completely. This introduces a variation of the real part of the refractive index.

#### 4.4.2 Gain-coupled DFB laser characterization

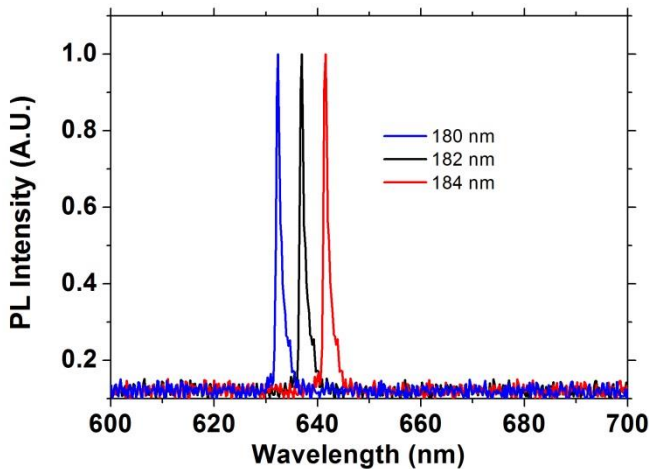
The same Q-switched frequency doubled Nd:YAG laser (532 nm) with a 7 nanosecond pulse width and a 938 Hz repetition rate was used to characterize the gain-coupled DFB laser. The beam has been again focused by a cylindrical lens to form a rectangular shape to pump the DFB laser.

Figure 4.30 shows the power emitted from the cleaved facet measured as a function of pump fluence, respectively on a double linear (Figure 4.31(a)) and a double logarithmic (Figure 4.30(b)) scale. The linearly scaled graph shows a clear lasing threshold at  $950 \mu\text{J}/\text{cm}^2$ . Taking into account the pulse length (7 ns), the equivalent CW pump fluence (power per pulse divided by the pulse time width) is then  $135.7 \text{ kW}/\text{cm}^2$ . The experimental data of Figure 4.31b was fitted to a static rate equation model [17-19], from which, a spontaneous emission factor ( $\beta$ ) of 0.007 was extracted. This threshold pump fluence is higher than for the index coupled laser. There could be different possible explanations for this higher threshold. One possibility is that the gain-coupled DFB lasers have a lower  $\kappa$  which leads to a higher threshold but also less spatial hole burning. Another possibility comes from these air cavities formed by the deposition (as shown in Figure 4.30(b)), which might lead to a lower optical cavity Q.

Figure 4.32 shows the emission spectra of three devices with varying grating period (pump fluence =  $1100 \mu\text{J}/\text{cm}^2$  @ 532 nm). The measured spectra show the lasers are operating in a single longitudinal mode. The three lasers exhibit 2 nm differences in grating period, which results in a 2.6 nm shift in the measured spectra.



**Figure 4.32:** (a) The light(in)-light(out) curve on a double linear scale, with an indication of the lasing threshold around  $950 \mu\text{J}/\text{cm}^2$ , which has an equivalent CW power density of  $135.7 \text{ kW}/\text{cm}^2$ . (b) The light (in)-light (out) curve on a double log-scale with rate equation fit (black solid). A spontaneous emission factor ( $\beta$ ) 0.007 is extracted.



**Figure 4.33:** Emission spectra of three devices with a varying grating period (pump fluence =  $1100 \mu\text{J}/\text{cm}^2$  @ 532 nm). Spectra measured from DFB lasers with different grating periods.

### 4.4.3 Conclusion

In this section, we have demonstrated gain-coupled DFB lasers using a periodically patterned layer of colloidal QDs as the gain layer. The measured spectra show the lasers are operating in a single longitudinal mode, without the need for introducing a phase shifter in the middle. Compared with previous III-V gain-coupled DFB lasers, the use of colloidal QDs as a chemically

synthesized gain material allows to achieve periodical structures without etching and without the need of complex epitaxial techniques. This shows the flexibility of colloidal QDs and points towards their application potential as a paint-on gain material for various substrates.

However, there is still room to further improve the performance of the colloidal QDs gain-coupled DFB laser. Limiting the patterned colloidal QDs sections to the region within the laser ridge will reduce sidewall roughness and hence internal losses of the device. An improved SiN deposition process and a chemical mechanical polishing (CMP) process can be used to planarize the top surface of the laser, further reducing the losses.

## 4.5 Colloidal nano-platelets integration

Unlike the sphere type colloidal QDs discussed thus far, which are usually at the size  $\sim 10$  nm and can be considered as zero dimensional nanocrystals, the recently developed colloidal nano-platelets (NPLs) are synthesized in a way that these nanocrystals are more like two-dimensional quantum wells. Here, in these types of nanocrystals, the energy levels are quantized in only one direction, which imposes a stricter momentum conservation rule for Auger recombination compared to zero dimensional colloidal QDs [36]. Time-resolved optical measurements have shown that high-energy carriers in NPLs relax to the band edge on time scales much faster than carrier recombination times, as needed for stimulated emission and lasing [37], which makes these NPLs promising for use as low threshold gain materials [38].

In this section, we will show that the hybrid SiN colloidal QDs integration platform developed for colloidal QDs integration can also be used for other colloidal nanocrystals like NPLs. We use CdSe NPLs, which have been demonstrated to exhibit optical gain in solution phase, and try to combine these NPLs with our SiN platform. We will show the NPLs can be embedded into SiN layer stacks while preserving their luminescence properties and stimulated emission. Waveguide based VSL measurements have been performed to determine the optical modal gain coefficient of the NPLs embedded in the SiN layers.

### 4.5.1 Transient Absorption Spectroscopy for the NPLs<sup>8</sup>

CdSe NPLs with a thickness of 1.21 nm (4 monolayers of CdSe) were synthesized according to the procedure outlined by Ihturria et al. [39]. Their

---

<sup>8</sup> Synthesis is carried out by Renue Tomar. Transient absorption spectroscopy is done by Renu Tomar and Pieter Geiregat from the PCN group UGent.

lateral dimension was measured using transmission electron microscopy (TEM) (as shown in Figure 4.33(a)) and found to be around  $34 \times 9.6 \text{ nm}^2$ . Hence the Bohr diameter of ca. 2 nm [40] is exceeded in both lateral dimensions leading to overall weak quasi-2D confinement. Figure 4.33(b) shows the absorption and emission spectrum of the sample dispersed in n-hexane. As is common for direct gap II-VI semiconductor quantum wells, two excitonic features are observed and attributed to the heavy (HH, 510nm) and light hole (LH, 480 nm) excitons [41]. The spontaneous photoluminescence shows no Stokes shift indicating the absence of any phonon-coupling. [42]

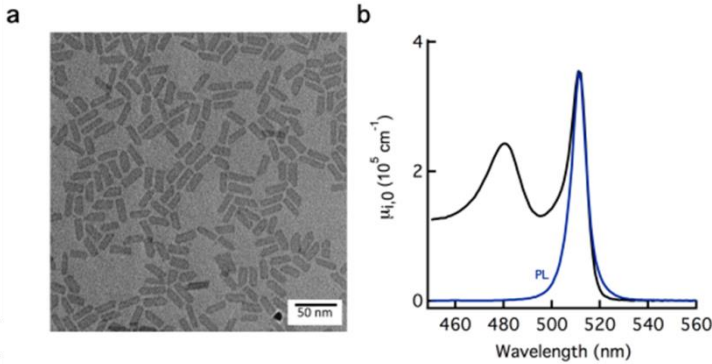


**Figure 4.34:** (a) Transmission Electron Microscope (TEM) image of 4 monolayers thick CdSe nano-platelets with an average lateral area of  $34 \times 9.6 \text{ nm}^2$ . (b) Photoluminescence (blue) linear absorption spectrum (black) of CdSe NPLs dispersed in hexane, normalized to represent the intrinsic absorption coefficient.

A TAS measurement has been carried out to characterize the spectroscopy under low-excitation conditions. We use absorbance  $A (= \Delta A + A_0)$  to quantify the optical gain development. Figure 4.34(a) shows a false color map showing only the region where  $A < 0$  upon photo-excitation with 400 nm light and a fluence creating  $\langle N \rangle = 10$ , corresponding to  $45 \mu\text{J}/\text{cm}^2$ . We observe that the absorbance turns negative in a band stretching from 525 to 560 nm and then narrows down and vanishes after *ca.* 100 ps. Figure 4.34(b) shows a map of the photoluminescence under similar excitation conditions. Asymmetric broadening towards lower energy (longer wavelengths) is observed, vanishing on a timescale similar as the net gain. Figure 4.34(c) shows spectral cuts for varying carrier densities at 2.5 ps of (a) and (b), where the absorbance is translated into an intrinsic absorption coefficient. Similar to the concept of negative absorbance implying gain, we can also relate this negative value for  $\mu_i$  to optical gain. Figure 4.34(d) summarizes the gain threshold, expressed in photo-generated electron-hole pairs per platelet at time zero, as a function of the probe

wavelength. Remarkably, the number of electron-hole pairs required to achieve net optical gain is  $5.3 (\pm 0.3)$ . This corresponds to a fluence of only  $12 \mu\text{J}/\text{cm}^2$ .

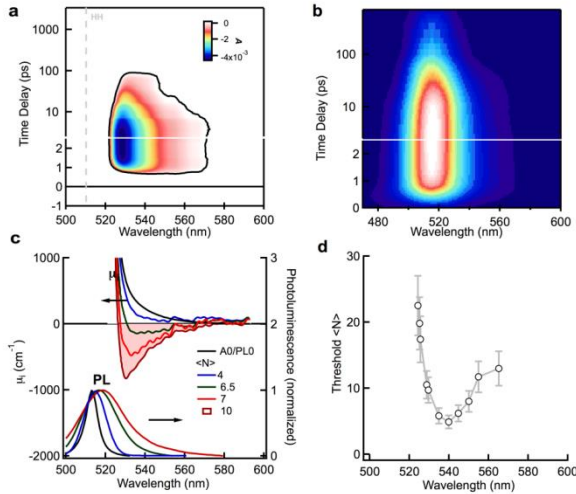


**Figure 4.35:** Overview of pump-probe and luminescence spectroscopy under low-excitation conditions. (a) 2D time-wavelength map of the negative part of the absorbance  $A(\lambda, t)$ , for photo-excitation at 400 nm with  $45 \mu\text{J}/\text{cm}^2$ , creating  $\langle N \rangle = 10$  electron hole-pairs at time zero. The gain is red shifted from the HH exciton peak at 510 nm and initially extends from 528 nm to 570 nm, only to narrow down and vanish after *ca.* 100 ps. Note that the gain spectrum extends up to 250 meV redshifted from the HH exciton line. (b) Photoluminescence as function of wavelength and time for similar excitation conditions as (a). A clear asymmetric broadening towards longer wavelengths is observed at early times, vanishing on a timescale similar to the net gain in (a). (c) At 2.5 ps, we take horizontal cuts from data sets as shown in (a) and normalize them appropriately to represent the intrinsic absorption coefficient  $\mu_i$  for increasing pump fluence expressed as  $\langle N \rangle$ . The shaded region indicates the gain band where intrinsic gain up to  $1000 \text{ cm}^{-1}$  is achieved for densities of 10 electron hole pairs per platelet. Bottom spectra show the photoluminescence spectra at 2.5 ps showing an increased contribution from a red-shifted (lower energy) component. Note that the gain spectrum  $\mu_i < 0$  overlaps perfectly with the region of increased PL bandwidth. (d) Threshold density of electron hole pairs for net optical gain to occur at a given wavelength. The minimum density is  $5.3 (\pm 0.3)$  and remarkably no gain is achieved at the position of the HH exciton line itself. Figures courtesy Renu Tomar

## 4.5.2 Waveguide modal gain measurement

We fabricate ridge waveguide with variable lengths containing these NPLs. The samples are fabricated following the process shown in Figure 4.7 replacing the spin coated colloidal QDs by NPLs. Here we use 2000 rpm spin coating to obtain a  $\sim 60$  nm thick NPLs layer. Also, note that the NPLs we used have 4 monolayers of CdSe without any shell structures. We found that the M-F H-SiN deposition quenches the photoluminescence, probably due to the high chamber temperature. Therefore, here we use a top M-F L-SiN ( $120^\circ\text{C}$ ) layer to encapsulate the NPLs layer to avoid material damage due to the chamber temperature.

Compared with SiN samples with *flash* colloidal QDs, the top surface of the sample with embedded NPLs is rougher. Figure 4.35 shows the comparison of a sample with *flash* dots and NPLs under the microscope. Note that compared with Figure 4.35(a), the color of the surface of the NPL (Figure 4.35(b)) sample is not uniform, indicating none uniform layer thickness. This roughness comes from the NPLs layer. Spin coating cannot guarantee a smooth surface for NPLs layer.

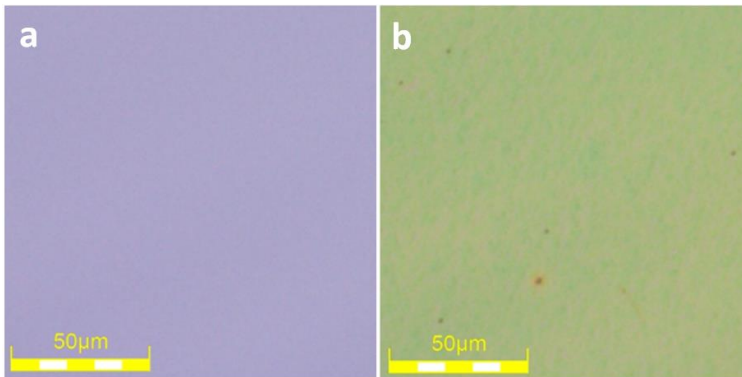


**Figure 4.36:** The microscopy picture comparison. (a) SiN stack sample with embedded *flash* dots. (b) SiN stack sample with embedded NPLs

A sample with  $4\ \mu\text{m}$  wide waveguides with variable length is fabricated. To check the quality of the layer stack and the etching profile, we made SEM images and a cross section of fabricated samples, as shown in Figure 4.36. Figure 4.36(a) shows a tilted SEM image of the waveguide sidewall. The waveguide side wall is quite smooth. However, small steps at the interfaces between the top SiN layer and the middle NPLs layer can be seen. Figure 4.36(b) shows a cross section of the fabricated sample. The sample was prepared using focus ion beam milling under the protection of a Platinum (Pt) layer, deposited by electron and ion beams. It is obvious that a layer of NPLs with a thickness

$\sim 60$  nm is perfectly embedded between the two layers of SiN. The top and bottom SiN layer thickness is around 100 nm.

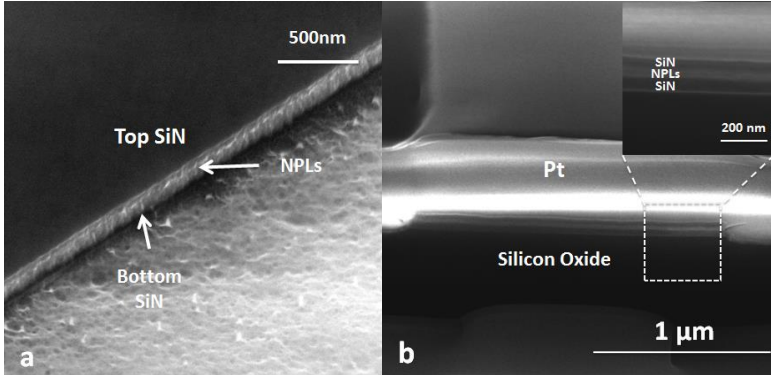


**Figure 4.37:** SEM picture of the fabricated sample. (a) The titled SEM picture showing the top SiN layer and waveguide side wall. (b) The cross section of the waveguide.

The sample is again pumped with the femtosecond laser system used in Chapter 4.2.2. Figure 4.37(a) is the ASE spectrum collected from the waveguide facet. The result shows an emission centered around 533.5 nm with an FWHM of 5.1 nm. Figure 4.37(b) shows the measured output power versus the waveguide length with a pump fluence around  $440 \mu\text{J}/\text{cm}^2$ . The figure shows a pronounced super-linear power increase as a function of waveguide length and the emission saturates for waveguides exceeding  $\sim 90 \mu\text{m}$ . If we consider a 5% reflection from the waveguide back, a confinement factor  $\Gamma = 0.33$  and a volume fraction  $f$  around 0.3; we can estimate the material gain to be around  $3500 \text{ cm}^{-1}$ . The results show the NPLs have higher gain coefficient compared with the *flash* colloidal QDs, with a gain threshold at the same order.

The intrinsic absorption coefficients  $\mu_i$  are strongly thickness and aspect ratio dependent. The platelets' intrinsic absorption coefficients are 3-4 times higher than the QDs. That means the platelets can absorb more to create more excitons with the same pumping condition [43].

A recent result from [44] shows a room temperature CW lasing by using the CdSe/CdS core-shell NPLs. In their work, the large gain from the NPLs enables lasing using short 1D photonics crystal cavities with a threshold input power less than  $1 \mu\text{W}$ . This work proves the NPLs lasing applications potential. It also gives the potential to use them as gain media to realize on-chip short cavities lasers with our hybrid SiN waveguide platform.

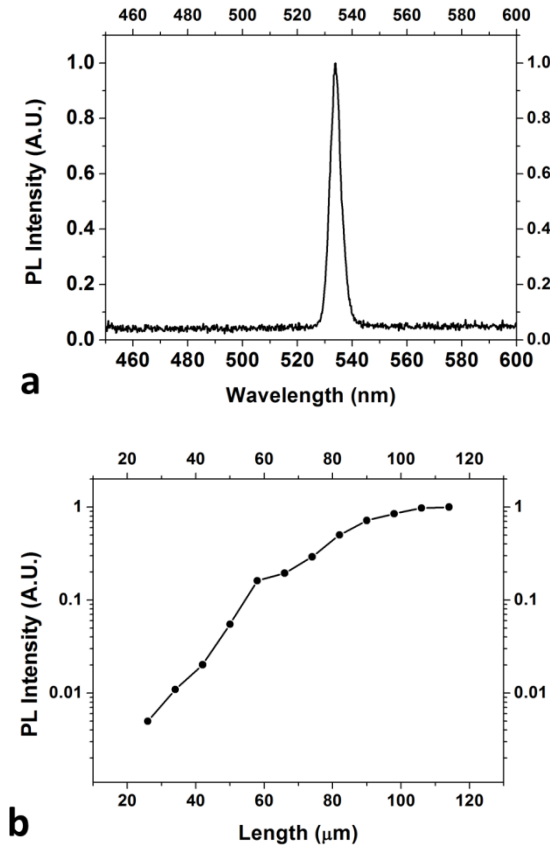


**Figure 4.38:** (a) Emission spectrum of a 4  $\mu\text{m}$  wide 100  $\mu\text{m}$  long waveguide with pump fluence 440  $\mu\text{J}/\text{cm}^2$  @ 400 nm. (b) Measured output power versus the waveguide length with pump fluence 440  $\mu\text{J}/\text{cm}^2$  @ 400 nm.

### 4.5.3 Conclusion

In this section, we have demonstrated that our hybrid SiN platform can also be used for integration of other colloidal gain materials such as NPLs. The NPLs can be embedded into SiN layer stacks without quenching their luminescence and light amplification properties. Using our waveguide based VSL measurement method a material gain around  $3500\text{ cm}^{-1}$  was extracted. This large intrinsic material gain can potentially enable short cavity lasers.

The NPLs we used consist of just a 4 monolayer CdSe layer with organic ligands. Their luminescence tends to be quenched using a 270°C PECVD chamber temperature. However, with a lower 120°C PECVD chamber temperature, their luminescence is well preserved. A CdS shell could be used to

cap the current NPLs and better preserve their optical properties after encapsulation into the SiN layer stack.

## 4.6 Conclusion

In this chapter, we present the work using colloidal QDs as gain material. The gain coefficient of the embedded colloidal QDs has been first measured using an improved waveguide based VSL methods. Later, we have shown the TAS measurement results of the *flash* CdSe/CdS colloidal QDs. The alloyed interface between the CdSe core and CdS shell in these CdSe/CdS QDs suppresses the Auger process. This improves the performance of the colloidal QDs with a longer bi-exciton lifetime, which is beneficial for lowering the lasing threshold. Later, a DFB based laser is designed, fabricated and characterized. The laser shows a quasi-CW pump threshold around  $39 \text{ kW/cm}^2$ . This measured threshold is at the same level as that of III-V semiconductor lasers epitaxially grown on silicon. This opens strong prospects in terms of CW operation and, consequently, application potential. To be fair, it is actually far from trivial to demonstrate beyond any doubt that observed behavior is lasing and not just amplified spontaneous emission. However, we believe we have very strong indications this is indeed laser operation. Following the laser checklist now provided by Nature Photonics [44], the following indications for laser operation are listed:

- Strong increase in output power. As shown in Figure 4.20 (a) and Figure 4.25, we see a clear threshold and strong increase of output power
- Spectral narrowing. As shown in Fig 4.20 (b) we see strong linewidth narrowing around the threshold. Above the threshold, further linewidth narrowing is limited by the length of the lasing pulse (under fs excitation) or due to transient carrier dispersion effects (under ns operation). As is shown for a similar device [45] the emitted pulse length above threshold reduces to a  $\sim 10 \text{ ps}$ . This is in agreement with the measured linewidth above threshold ( $\sim 0.2 \text{ nm}$ )
- High output power. We estimate the equivalent output power of the laser to be around  $100 \text{ mW}$  (The laser gives around  $-60 \text{ dBm}$  average output. If we consider the  $1000 \text{ Hz}$  repetition rate from the pump source, and the pulse length around  $10 \text{ ps}$ , we are having a  $100 \text{ mW}$  average output)
- SE-clamping. We have some indication the SE besides the laser mode is clamped above threshold in Figure 4.21 (b), indicating the gain is clamped to its threshold level.

We also present the design, fabrication and characterization of a gain-coupled DFB laser based on colloidal QDs. The gain-coupled laser shows single mode lasing under nanosecond laser pump without the phase shifter in the middle of the laser cavity. At the end of this chapter, we have also shown that

this hybrid SiN colloidal QDs integration platform can also be used for a new class of solution processed nanomaterials, i.e. NPLs. These NPLs can be embedded into SiN layer stacks without quenching their luminescence and light amplification properties. The NPLs shows higher optical gain coefficient with the same gain threshold compared with *flash* CdSe/CdS colloidal QDs. This gives application potential to realize lasers with shorter optical cavities with our hybrid SiN waveguide platform. However, NPLs still shows some disadvantages. The NPLs are not as robust as *flash* CdSe/CdS colloidal QDs. Their luminescence tends to quench with high temperature. Also, spin coating cannot provide a uniform layer for NPLs. This brings challenges to realize high quality optical microcavities.

## References

- [1] Pietryga, Jeffrey M., Young-Shin Park, Jaehoon Lim, Andrew F. Fidler, Wan Ki Bae, Sergio Brovelli, and Victor I. Klimov. "Spectroscopic and device aspects of nanocrystal quantum dots." *Chem. Rev* 116, no. 18 (2016): 10513-10622.
- [2] Wang, Yue, Van Duong Ta, Yuan Gao, Ting Chao He, Rui Chen, Evren Mutlugun, Hilmi Volkan Demir, and Han Dong Sun. "Stimulated emission and lasing from CdSe/CdS/ZnS core - multi - shell quantum dots by simultaneous three - photon absorption." *Advanced Materials* 26, no. 18 (2014): 2954-2961.
- [3] Dang, Cuong, Joonhee Lee, Craig Breen, Jonathan S. Steckel, Seth Coe-Sullivan, and Arto Nurmikko. "Red, green and blue lasing enabled by single-exciton gain in colloidal quantum dot films." *Nature nanotechnology* 7, no. 5 (2012): 335-339.
- [4] Roh, Kwangdong, Cuong Dang, Joonhee Lee, Songtao Chen, Jonathan S. Steckel, Seth Coe-Sullivan, and Arto Nurmikko. "Surface-emitting red, green, and blue colloidal quantum dot distributed feedback lasers." *Optics express* 22, no. 15 (2014): 18800-18806.
- [5] Dang, Cuong, Joonhee Lee, Kwangdong Roh, Hanbit Kim, Sungmo Ahn, Heonsu Jeon, Craig Breen, J. S. Steckel, Seth Coe-Sullivan, and Arto Nurmikko. "Highly efficient, spatially coherent distributed feedback lasers from dense colloidal quantum dot films." *Applied Physics Letters* 103, no. 17 (2013): 171104.
- [6] Min, Bumki, Sungjee Kim, Koichi Okamoto, Lan Yang, Axel Scherer, Harry Atwater, and Kerry Vahala. "Ultralow threshold on-chip microcavity nanocrystal quantum dot lasers." *Applied physics letters* 89, no. 19 (2006): 191124.
- [7] Guilhabert, B., Caroline Foucher, Anne-Marie Haughey, E. Mutlugun, Y. Gao, Johannes Herrnsdorf, H. D. Sun, H. V. Demir, M. D. Dawson, and Nicolas Laurand. "Nanosecond colloidal quantum dot lasers for sensing." *Optics express* 22, no. 6 (2014): 7308-7319.
- [8] McLellan, Luke Jonathan, Benoit Guilhabert, Nicolas Laurand, and Martin D. Dawson. "CdS x Se 1-x/ZnS semiconductor nanocrystal laser with sub 10kW/cm<sup>2</sup> threshold and 40nJ emission output at 600 nm." *Optics express* 24, no. 2 (2016): A146-A153.

- [9] Wang Z, Tian B, Pantouvaki M, Guo W, Absil P, Van Campenhout J, Merckling C, Van Thourhout D. "Room-temperature InP distributed feedback laser array directly grown on silicon." *Nature Photonics*. 2015 Dec 1; 9(12):837-42.
- [10] Cirillo, Marco, Tangi Aubert, Raquel Gomes, Rik Van Deun, Philippe Emplit, Amelie Biermann, Holger Lange, Christian Thomsen, Edouard Brainis, and Zeger Hens. "'Flash' Synthesis of CdSe/CdS Core-Shell Quantum Dots." *Chemistry of Materials* 26, no. 2 (2014): 1154-1160.
- [11] Drijvers, Emile, Jonathan De Roo, Pieter Geiregat, Krisztina Fehér, Zeger Hens, and Tangi Aubert. "Revisited Wurtzite CdSe Synthesis: A Gateway for the Versatile Flash Synthesis of Multishell Quantum Dots and Rods." *Chemistry of Materials* 28, no. 20 (2016): 7311-7323.
- [12] Bae, Wan Ki, Lazaro A. Padilha, Young-Shin Park, Hunter McDaniel, Istvan Robel, Jeffrey M. Pietryga, and Victor I. Klimov. "Controlled alloying of the core-shell interface in CdSe/CdS quantum dots for suppression of Auger recombination." *ACS nano* 7, no. 4 (2013): 3411-3419.
- [13] Hens, Zeger, and Iwan Moreels. "Light absorption by colloidal semiconductor quantum dots." *Journal of Materials Chemistry* 22, no. 21 (2012): 10406-10415.
- [14] Park, Young-Shin, Wan Ki Bae, Thomas Baker, Jaehoon Lim, and Victor I. Klimov. "Effect of Auger recombination on lasing in heterostructured quantum dots with engineered core/shell interfaces." *Nano letters* 15, no. 11 (2015): 7319-7328.
- [15] Dal Negro, L., P. Bettotti, M. Cazzanelli, D. Pacifici, and L. Pavesi. "Applicability conditions and experimental analysis of the variable stripe length method for gain measurements." *Optics communications* 229, no. 1 (2004): 337-348.
- [16] Zhu, Yunpeng, Weiqiang Xie, Pieter Geiregat, Suzanne Bisschop, Tangi Aubert, Edouard Brainis, Zeger Hens, and Dries V. Thourhout. "Hybrid colloidal quantum dot silicon nitride waveguide gain measurement based on variable stripe length method." In *CLEO: Applications and Technology*, pp. AT1J-5. Optical Society of America, 2016.
- [17] Morthier, Geert, and Patrick Vankwikelberge. *Handbook of distributed feedback laser diodes*. Artech House, 2013.
- [18] Yokoyama, H., and S. D. Brorson. "Rate equation analysis of microcavity lasers." *Journal of Applied Physics* 66, no. 10 (1989): 4801-4805.

- [19] Shore, K. A., and M. Ogura. "Threshold characteristics of microcavity semiconductor lasers." *Optical and quantum electronics* 24, no. 2 (1992): S209-S213.
- [20] Stöferle, Thilo, Nikolaj Moll, Thorsten Wahlbrink, Jens Bolten, Thomas Mollenhauer, Ullrich Scherf, and Rainer F. Mahrt. "Ultracompact silicon/polymer laser with an absorption-insensitive nanophotonic resonator." *Nano letters* 10, no. 9 (2010): 3675-3678.
- [21] Yakunin, Sergii, Loredana Protesescu, Franziska Krieg, Maryna I. Bodnarchuk, Georgian Nedelcu, Markus Humer, Gabriele De Luca, Manfred Fiebig, Wolfgang Heiss, and Maksym V. Kovalenko. "Low-threshold amplified spontaneous emission and lasing from colloidal nanocrystals of caesium lead halide perovskites." *Nature communications* 6 (2015): 8056.
- [22] Adachi, Michael M., Fengjia Fan, Daniel P. Sellan, Sjoerd Hoogland, Oleksandr Voznyy, Arjan J. Houtepen, Kevin D. Parrish, Pongsakorn Kanjanaboos, Jonathan A. Malen, and Edward H. Sargent. "Microsecond-sustained lasing from colloidal quantum dot solids." *Nature communications* 6 (2015): 8694.
- [23] Fan, Fengjia, Oleksandr Voznyy, Randy P. Sabatini, Kristopher T. Bicanic, Michael M. Adachi, James R. McBride, Kemar R. Reid et al. "Continuous-wave lasing in colloidal quantum dot solids enabled by facet-selective epitaxy." *Nature* (2017).
- [24] Yang, Zhili, Matthew Pelton, Igor Fedin, Dmitri V. Talapin, and Edo Waks. "A room temperature continuous-wave nanolaser using colloidal quantum wells." *Nature Communications* 8 (2017).
- [25] Martens, Daan, and Peter Bienstman. "Comparison between Vernier-cascade and MZI as transducer for biosensing with on-chip spectral filter." *Nanophotonics* (2017).
- [26] Kogelnik, H., and C. V. Shank. "Coupled - wave theory of distributed feedback lasers." *Journal of applied physics* 43, no. 5 (1972): 2327-2335.
- [27] Buus, J. "Mode selectivity in DFB lasers with cleaved facets." *Electronics Letters* 21, no. 5 (1985): 179-180.
- [28] Soda, Haruhisa, Yuji Kotaki, Hisao Sudo, Hiroshi Ishikawa, Sigeyuki Yamakoshi, and Hajime Imai. "Stability in single longitudinal mode operation in GaInAsP/InP phase-adjusted DFB lasers." *IEEE Journal of Quantum Electronics* 23, no. 6 (1987): 804-814.

- [29] Nakano, Y. O. S. H. I. A. K. I., and Kunio Tada. "Analysis, design, and fabrication of GaAlAs/GaAs DFB lasers with modulated stripe width structure for complete single longitudinal mode oscillation." *IEEE journal of quantum electronics* 24, no. 10 (1988): 2017-2033.
- [30] Kinoshita, J., and Kenji Matsumoto. "Yield analysis of SLM DFB lasers with an axially-flattened internal field." *IEEE Journal of Quantum Electronics* 25, no. 6 (1989): 1324-1332.
- [31] Vankwikelberge, Patrick, Geert Morthier, and Roel Baets. "CLADISS-a longitudinal multimode model for the analysis of the static, dynamic, and stochastic behavior of diode lasers with distributed feedback." *IEEE Journal of Quantum Electronics* 26, no. 10 (1990): 1728-1741.
- [32] Vankwikelberge, P., F. Buytaert, A. Francois, R. Baets, P. I. Kuindersma, and C. W. Fredriksz. "Analysis of the carrier-induced FM response of DFB lasers: Theoretical and experimental case studies." *IEEE Journal of Quantum Electronics* 25, no. 11 (1989): 2239-2254.
- [33] Whiteaway, J. E. A. "The Influence of Longitudinal Mode Spatial Hole Burning on the Linewidth and Spectrum of  $\pi/4$ -Phase Shifted DFB Laser." *J O, OC UM ER* Th. N PAGE: 104.
- [34] Takemoto, A., H. Watanabe, Y. Nakajima, Y. Sakakibara, S. Kakimoto, H. Namizaki, J. Yamashita, T. Hatta, and Y. Miyake. "Low harmonic distortion distributed feedback laser diode and module for CATV systems." In *Optical Fiber Communication Conference*, p. FE2. Optical Society of America, 1990.
- [35] Luo, Y., Y. Nakano, K. Tada, T. Inoue, H. Hosomatsu, and H. Iwaoka. "Purely gain - coupled distributed feedback semiconductor lasers." *Applied Physics Letters* 56, no. 17 (1990): 1620-1622.
- [36] Grim, Joel Q., Sotirios Christodoulou, Francesco Di Stasio, Roman Krahné, Roberto Cingolani, Liberato Manna, and Iwan Moreels. "Continuous-wave biexciton lasing at room temperature using solution-processed quantum wells." *Nature nanotechnology* 9, no. 11 (2014): 891-895.
- [37] Pelton, Matthew, Sandrine Ithurria, Richard D. Schaller, Dmitriy S. Dolzhanikov, and Dmitri V. Talapin. "Carrier cooling in colloidal quantum wells." *Nano letters* 12, no. 12 (2012): 6158-6163.
- [38] She, Chunxing, Igor Fedin, Dmitriy S. Dolzhanikov, Arnaud Demortière, Richard D. Schaller, Matthew Pelton, and Dmitri V. Talapin. "Low-threshold stimulated emission using colloidal quantum wells." *Nano letters* 14, no. 5 (2014): 2772-2777.

- [39] Ithurria, S., M. D. Tessier, B. Mahler, R. P. S. M. Lobo, B. Dubertret, and Al L. Efros. "Colloidal nanoplatelets with two-dimensional electronic structure." *Nature materials* 10, no. 12 (2011): 936.
- [40] Naeem, Ali, Francesco Masia, Sotirios Christodoulou, Iwan Moreels, Paola Borri, and Wolfgang Langbein. "Giant exciton oscillator strength and radiatively limited dephasing in two-dimensional platelets." *Physical Review B* 91, no. 12 (2015): 121302.
- [41] Pelant, Ivan, and Jan Valenta. *Luminescence spectroscopy of semiconductors*. Oxford University Press, 2012.
- [42] Achtstein, Alexander W., Andrei Schliwa, Anatol Prudnikau, Marya Hardzei, Mikhail V. Artemyev, Christian Thomsen, and Ulrike Woggon. "Electronic structure and exciton–phonon interaction in two-dimensional colloidal CdSe nanosheets." *Nano letters* 12, no. 6 (2012): 3151-3157.
- [43] Yang, Zhili, Matthew Pelton, Igor Fedin, Dmitri V. Talapin, and Edo Waks. "A room temperature continuous-wave nanolaser using colloidal quantum wells." *Nature Communications* 8, no. 1 (2017): 143.
- [44] <https://www.nature.com/authors/policies/laserchecklist.pdf>
- [45] W. Xie, T. Stoferle, G. Raino, T. Aubert, S. Bisschop, Y. Zhu, R. Mahrt, P. Geiregat, E. Brainis, Z. Hens, D. Van Thourhout, "On-chip Integrated Quantum-dot Silicon Nitride Microdisk Lasers", *Advanced Materials* 29, no. 16 (2017).



# 5

## **Colloidal quantum dot as single photon source in SiN platform**

Solid state photon emitters which can provide single photons on-demand are an essential building block in photonic quantum technology. Currently, there are several options in terms of material platform to realize single photon generation. The platforms include color centers or defects in crystalline hosts [1-3], carbon nanotubes [4], transition metal dichalcogenides [5] and epitaxial [6-8] and colloidal semiconductor nanocrystals or quantum dots [9-12]. As already discussed in Chapter 2, colloidal QDs are promising candidates since they offer extensive design freedom in terms of the synthesis as well as room temperature operation. The emission wavelength of colloidal QDs can be readily tuned by changing their diameter. Moreover, colloidal synthesis methods offer extensive control over the QD size and shape, which enables complex heterostructures to be formed.

Room temperature photon anti-bunching in the luminescence of single colloidal QDs was first reported for CdSe/ZnS core/shell QDs. This observation was attributed to the efficient, non-radiative Auger recombination of the multi-excitons [13-14]. This enabled the emission of a single photon to be triggered by

a high-intensity excitation pulse, with a near-unity probability of photo-excitation and a high-purity single photon emission [9-10].

The characterization of these dots is usually done by diluted solution spin coating to a glass substrate. This approach relies on the possibility to find single QD on the substrate, lacking accurate control of the position of the single QDs. In addition, most of the emission from the single QD goes to the free space and can only be collected with microscopy systems.

PICs, originally developed mainly for telecom applications, are now also finding widespread application in domains as diverse as bio-sensing [15], spectroscopy [16] and quantum optics [17-18]. For large-scale quantum optic circuits, PICs can enable complicated quantum information processing [19]. Other than early experimental demonstrations of quantum optics, which relied on bulky optical components, a PIC platform for integrated quantum optics can not only improve the thermal and mechanical stability but also has advantages in term of scalability. However, a glass substrated waveguide platform that allows efficient collection of the emission from a single dot is hard to achieve to realize further large-scale PIC aiming for more complicated quantum information processing.

In Chapter 3, we have demonstrated a low loss SiN waveguide platform for colloidal QDs integration. By combining this waveguide platform with individual colloidal QDs, we could realize on-chip single photon sources.

Previously, Weiqiang Xie and *et al.* have demonstrated using high-quality LB deposition and a residue-free lift off the process to pattern single colloidal QDs onto substrate [20]. With this process, single dot patterning of colloidal QD films can be realized. The experiment shows feature sizes down to ~30 nm for a continuously uniform film of QDs and a yield up to 40% for single QD positioning can be obtained. Figure 5.1 shows the SEM picture of lift off results with LB colloidal QDs layer deposition, using ~ 33 nm thickness resist with pattern holes ~ 31.6 nm in diameter. The 5 by 5 grid image has the same scale bar of 50 nm, which has been shown in Figure 5.1.

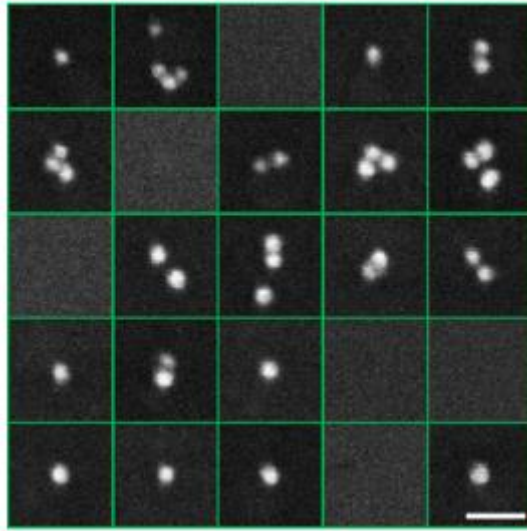


**Figure 5.1:** SEM picture of lift off results with LB colloidal QDs layer deposition, using  $\sim 33$  nm thickness resist with pattern holes  $\sim 31.6$  nm in diameter. The 5 by 5 grid image has the same scale bar of 50 nm. The scale bar has been put at the right bottom corner. Adapted from ref [20].

To integrate single colloidal QD directly on a photonic chip, a major challenge also consists in efficiently coupling the emission from the single QDs into a single guided mode [21]. This is seen by many as stumbling block precluding the usage in practical implementations. Using FDTD simulations, the emission from dipole-like nanometer-sized inclusions embedded into different silicon nitride photonic waveguide designs was studied by Suzanne Bisschop and *et al.* [21] The simulations show that, for suspended strip waveguides, one can simultaneously achieve a good coupling factor up to  $\beta = 60\%$  and a high polarization ratio up to  $\beta_y/\beta = 95\%$ , as shown in Figure 5.2. For suspended slot waveguides, a higher coupling factor up to  $\beta = 65\%$  is achievable in combination with a similar polarization ratio up to  $\beta_z/\beta = 96\%$ , as shown in Figure 5.3. Note here the x-axis is the light propagation direction, y-axis is parallel to the waveguide surface plane, z-axis is perpendicular to the waveguide surface plane.  $\beta_y/\beta$  denotes the ratio of the TE components over all the coupled emission;  $\beta_z/\beta$  denotes the ratio of the TM components over all the coupled emission.

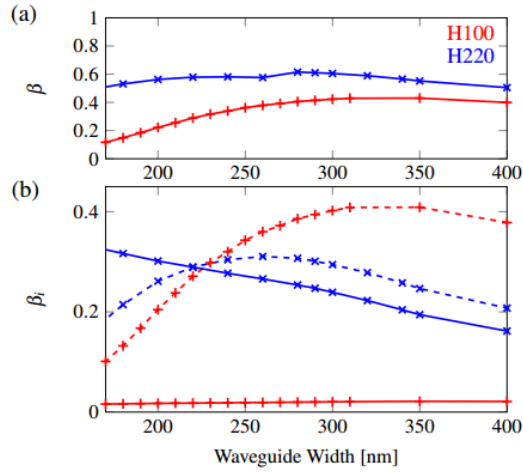


**Figure 5.2:** The coupling factor and polarization ratio for a suspended SiN waveguide with a dipole-like emitter in the middle of the waveguide. (a) Total coupling factor  $\beta$  to the guided modes as a function of the waveguide width  $W$  for two different waveguide heights  $H = 100$  nm (red) and  $220$  nm (blue). (b) Polarization dependent coupling factors  $\beta_y$  (dashed line) and  $\beta_z$  (plain line) as a function of the waveguide width  $W$  for two different waveguide heights  $H = 100$  nm (red) and  $220$  nm (blue). Adapted from ref [21].

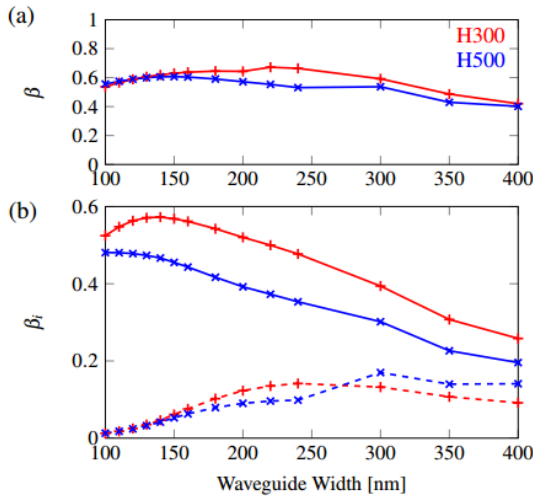


**Figure 5.3:** The coupling factor and polarization ratio of a suspended SiN slot-waveguide with a dipole-like emitter in the middle of the waveguide.. (a) Total coupling factor  $\beta$  to the guided modes as a function of the waveguide width  $W$  for two different waveguide heights  $H = 300$  nm (red) and  $500$  nm (blue). (b) Polarization dependent coupling factors  $\beta_y$  (dashed line) and  $\beta_z$  (plain line) as a function of the waveguide width  $W$  for two different waveguide heights  $H = 300$  nm (red) and  $500$  nm (blue). Adapted from ref [21].

As mentioned above colloidal CdSe/CdS core-shell QDs have been shown to be a potential candidate as single-photon emitter in the visible wavelength range [9-10,13]. Vigneshwaran Chandrasekaran and et al. from the PCN group have demonstrated anti-bunching for the flash core-shell CdSe/CdS colloidal QDs, spincoated on a glass substrate at room temperature, as shown in Figure 5.4 [22]. The second order intensity correlation function is generally used to determine the quality of the single photon sources, as has been already discussed in Chapter 2.2. For an ideal single photon source,  $g^{(2)}(0) = 0$ . From the measurement in Figure 5.4,  $g^{(2)}(0) = 0.1$  can be extracted which indicates quite good anti-bunching, both for continuous and pulsed excitation.

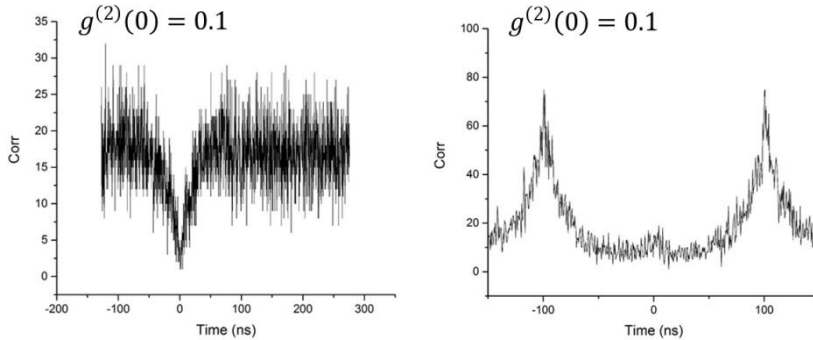


**Figure 5.4:** Anti-bunching established with both continuous and pulse excitation proving that the *flash* CdSe/CdS core/shell QD is a good single photon emitter. Adapted from [22].

Combining the work described above, we believe an on-chip single photon source exploiting colloidal QDs is feasible. In this chapter, we will first design, fabricate and characterize an ultra-compact silicon nitride grating coupler to maximize the coupling between the optical mode of a waveguide to a microscopy system and help to characterize the on-chip single photon source. We will then also show a suspended waveguide with an embedded mono-layer of colloidal QDs patches. This will allow studying if the emission from the embedded colloidal QD patches can be efficiently coupled to the optical mode of the suspended waveguide and further coupled out by the ultra-compact grating coupler.

## 5.1 Ultra-compact silicon nitride grating coupler for microscopy systems<sup>9</sup>

Grating couplers are now extensively used to couple light between optical fibers and PICs. The use of grating couplers allows avoiding expensive processing and packaging steps such as facet polishing and lensed fiber alignment. Grating couplers with high efficiency and relatively large optical bandwidth [24-27] have been successfully demonstrated for traditional telecom wavelengths and near infrared wavelengths [28]. They have become standard components in PIC platforms and enable wafer scale testing.

As discussed above a key building block for PIC based quantum optics is an integrated single photon source, required in applications as diverse as quantum teleportation [29], quantum computation [30] and several schemes for quantum cryptography [31]. Current efforts to realize integrated single photon sources rely, amongst others, on using nonlinear four-wave mixing [32] and epitaxially

<sup>9</sup> The text in this section is adapted from ref [23]

grown quantum dots [33]. Also colloidal CdSe/ZnS core-shell quantum dots (QD) have been shown to be efficient single-photon emitters [9-10, 13]. Further, as mentioned in the previous section, we recently have demonstrated a hybrid QD-SiN platform, which allows combining colloidal quantum dots with low loss waveguides [34]. Moreover in [21] we showed that a dipole emitter embedded in a SiN waveguide with optimized dimensions can couple up to 43% of its emission to a single waveguide mode, with a 95% polarization ratio. Finally, we experimentally demonstrated the capability for positioning individual quantum dots at a predefined location with high yield [20]. The combination of these results shows the hybrid QD-SiN platform offers the potential for realizing efficient on chip single photon sources in combination with complex photonic circuits.

However, to characterize these QDs based integrated single photon sources and the associated photonic circuits, it is desired to use a high numerical aperture (NA) microscopy system, since it can help to accurately localize the optical excitation and maximize the collection efficiency. An important building block for such systems is an efficient, compact and broad band coupler that can extract the light from the PIC towards a standard microscopy system. Standard grating couplers, which are optimized for fiber-to-chip coupling, typically not only have dimensions similar to those of the core of single mode optical fibers ( $100\ \mu\text{m}$ ) but also need an optimized taper between the waveguide and the grating coupler to achieve high coupling efficiency. Therefore, they are usually not compact enough for large NA microscopy applications. On the other hand, single mode optical fibers have a small numerical aperture (NA) compared to a typical microscopy system. The much larger NA of a microscopy system allows a wider collection angle, possibly leading to higher coupling efficiency and wider bandwidth. Hence there is a need for compact, efficient and broad-band components, which can couple light from a chip to an objective. There has been some work describing compact on-chip couplers before [35-36]. A similar design has also been used as an optical antenna unit in a nanophotonic phased array, to couple light from a waveguide to free space, focusing on beam steering applications [37]. However, these designs are based on silicon or III-V PICs, which exhibit a higher index contrast. Compared with the silicon and III-V PIC platforms, the SiN PIC platform offers a wider optical transparent window with lower optical propagation loss [38]. However, its lower index contrast makes realizing efficient grating couplers more challenging.

Therefore, we present a methodological approach for the design, fabrication and characterization of an ultra-compact SiN grating for coupling light from PIC waveguide to a microscopy system.

### 5.1.1 Grating coupler design

As shown in Figure 5.5(a), the parameters of a diffraction grating that can be optimized are usually its period, the etching depth, the filling factor, the number of periods and the distance between grating and substrate. All simulations were carried out at the He-Ne laser's lasing wavelength of 632.8 nm. This wavelength lies in the range of our colloidal QDs emission bandwidth and it allows for straightforward experimental verification of the simulation results. We choose silicon nitride ( $n=1.91@ 632.8$  nm) as the waveguide material and fixed the thickness of the waveguide to 220 nm. In previous work, simulations showed that this waveguide thickness optimizes light coupling between emission from an embedded QD emitter to the waveguide optical mode [21]. The top view of the proposed grating coupler is shown in Figure 5.5(b). The grating coupler has been designed in a circular shape. We are aiming to under etch the substrate material beneath the grating, on the one hand because it enhances the coupling of the emission of an embedded dipole emitter to the waveguide optical mode, while on the other hand it further enhances the efficiency of the grating coupler. Therefore, a small supporting beam has been added between the grating coupler and the waveguide to ensure a fully suspended structure is realistic.

We choose to etch completely through the grating to increase its contrast while in the meantime also making the fabrication process easier. The filling factor is fixed to 0.5 to guarantee an easier process. To determine the best parameters for the grating coupler, 3D finite difference time domain (FDTD) simulations were carried out. The fundamental TE mode of the suspended waveguide (600 nm in width, 220 nm in thickness) has been used to excite the grating. A field and power monitor have been placed  $0.5 \mu\text{m}$  above the grating to check the power scattered upwards by the grating coupler. Since we are more interested in how much light will be captured by an objective, also the far field radiation pattern of this field and power monitor has been simulated, to be able to calculate the power collected by an objective with a given NA (0.65 in the remainder of this section).

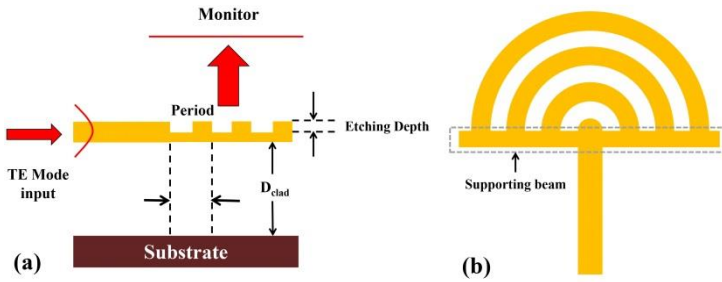


**Figure 5.5:** (a) The schematic of the grating coupler design; (b) The top view of the proposed circular shape grating coupler, a small supporting beam is added between the grating coupler and the waveguide to ensure a fully suspended structure realistic.

We first varied the period of a grating coupler consisting of only 3 periods without substrate. We calculated the total power coupled upwards and the far field as collected by an objective with  $NA = 0.65$ . The results are shown in Figure 5.6(a). The dip around 525 nm corresponds to the period for which the first order diffraction is radiated nearly vertically and the second order diffraction is coupled backwards in the waveguide, leading to reduced upwards coupling. We can also find a reduced upwards diffraction for periods around 800 nm and 1050 nm, corresponding to the situations whereby the third and fourth order diffraction are coupled in the waveguide. Also note that the N.A. 0.65 collection efficiency decreases dramatically with increasing period, which can be attributed to the fact that more light goes outside of the collection angle for larger grating periods (more light is coupled in higher order diffraction angle with large inclination).

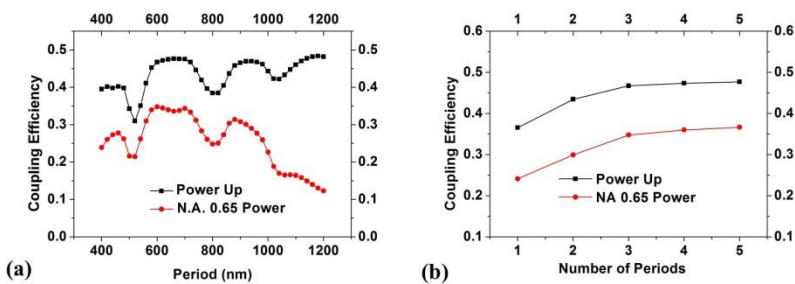


**Figure 5.6:** (a) 3D FDTD simulation results of period length vs power up/power collected with  $NA = 0.65$ ; (b) 3D FDTD simulation results of number of periods vs power up/power collected  $NA = 0.65$  (the period length is 600 nm).

As we aim to minimize the grating coupler size, we also simulated the influence of the number of periods. Figure 5.6(b) shows the power coupled

upwards and the power collected within an  $NA = 0.65$  as function of the number of periods, with the period of the grating fixed to 600 nm. The results clearly show that with an increased number of periods, more light gets deflected upwards. Fully etching the grating ensured a high contrast and results in an efficient diffraction for the light from the waveguide. From the simulation, we can conclude that 3 periods form a good balance between the coupling efficiency and the compactness of the grating coupler.

We have also done the filling factor scan. Figure 5.7 shows the power coupled upwards as a function of the filling factor with 3 periods grating and 600 nm period length. The result indicates a maximum coupling efficiency with a 0.45 filling factor.

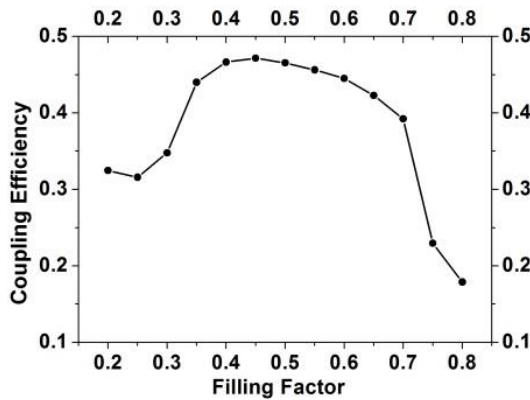


**Figure 5.7:** the power coupled upwards as a function of the filling factor with 3 periods grating with 600 nm period length

The distance between the substrate and the grating plays a major influence in controlling the grating coupler's upwards efficiency. Without substrate, the grating deflects the light upwards and downwards evenly because of the symmetric index distribution. With the substrate, the light radiated downwards by the grating coupler will get reflected at the substrate interface. By carefully choosing the distance between grating and substrate ( $D_{\text{clad}}$ ), this field can interfere constructively with the field coupled directly upwards. Improving the reflection from the substrate interface can also improve the upwards coupling efficiency.

Silicon is a high index material, which can already provide 34.9% reflection. However, a metal mirror is a better choice since it can provide higher reflection with only a few tens of nanometer thickness. It can also act as a stop layer during wet etching since we are aiming for suspended waveguides. Table 5.1 shows the reflectance of commonly used metals at 632.8 nm.

Metal	Ag	Al	Au	Cr	Ti
Reflectance	98. 8%	90. 8%	96. 0%	55. 3%	61. 2%

**Table 5.1:** Reflectance at 632.8 nm of commonly used metals.

From Table 5.1, Ag, Al and Au show better performance in terms of the reflection at 632.8 nm. However, a Ag layer can easily get oxidized which will reduce the reflection. Au needs the addition of a thin Cr layer between Si and Au to improve the adhesion. Moreover, a thicker Au layer is needed for high reflection. Figure 5.8 shows calculation results with varying Al and Au thickness as a function of the reflectance at 632.8 nm. An Al layer around 30 nm can already guarantee a strong reflection while around 80 nm thickness is needed for Au to achieve the same reflection. So we choose Al as the metal to enhance the reflection from the substrate.

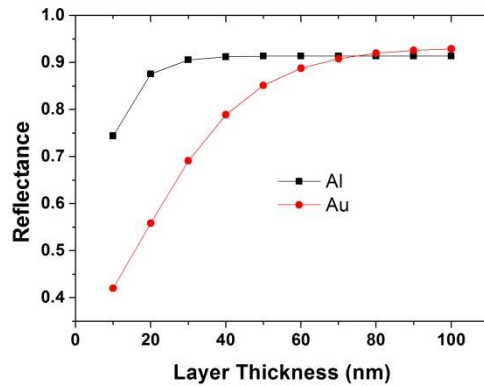


**Figure 5.8:** The reflectance with different metal layer thickness at 632.8 nm. Al layer and Au layer is compared.

Figure 5.9(a) shows how the coupling efficiency varies as a function of the distance between the substrate and the grating. In this simulation, the grating coupler's period length has been set to 600 nm with a 0.5 filling factor. We compare the results for a standard silicon substrate and for a substrate with a 50 nm Aluminium (Al) ( $n_{\text{real}}=1.38$ ;  $n_{\text{imaginary}}=7.62$  @ 632.8 nm) layer coated on top. The total power radiated upwards and the power collected within an  $\text{NA} = 0.65$  results are presented. By coating the silicon substrate with Al, the reflection is improved, which enhances the grating coupler's performance. Figure 5.9(b) shows the far field radiation pattern of the grating coupler with optimized parameters (Al coating; 600 nm period length; 950 nm  $D_{\text{clad}}$  distance). An NA of 0.65 corresponds to a collection half angle of  $40.54^\circ$ . The simulated far field

radiation distribution shows a well-controlled field distribution: most of the scattered energy stays inside of this half angle, which will be efficiently collected. Figure 5.9(c) shows how the coupling efficiency varies as function of the collection NA. With a high-NA objective (NA=0.95) almost 75% of the light can be collected. We have also simulated the optical bandwidth of the grating couplers. Figure 5.9(d) shows the simulated bandwidth and collecting efficiency comparison for different gratings. The black curve is the result for the ultra-compact grating; maximum 59.1% efficiency with a 116 nm 1dB bandwidth can be achieved. The red curve is the result for the ultra-compact grating with silicon oxide layer underneath (with Al layer below silicon oxide layer). Result shows a decreased efficiency due to the low contrast of the grating. The blue curve is the result of the 1d normal grating [28] (10  $\mu\text{m}$  in width; 0.43  $\mu\text{m}$  period length; 70 nm shallow etched; 20 periods), a maximum 38% efficiency with a 71 nm 1dB bandwidth is achieved. Our ultra-compact grating's large bandwidth results both from the high index contrast of the grating coupler and the large NA of the microscopy system (compared to a single mode fiber).

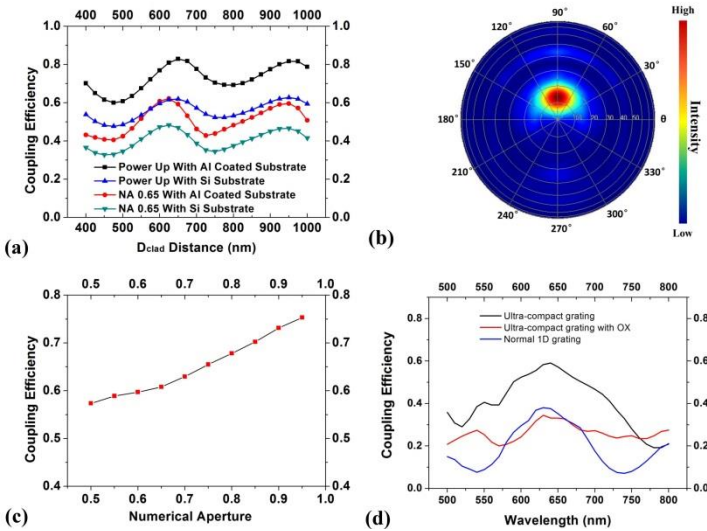


**Figure 5.9:** (a) 3D FDTD simulation results of total power radiated upwards and power collection with NA = 0.65 versus distance  $D_{\text{clad}}$ . Results for substrates with/without Al coating are shown. (b) 3D FDTD simulation of far field radiation pattern of the grating coupler with optimized parameters (600 nm period length; 950nm  $D_{\text{clad}}$  distance). (c) Simulation results of coupling efficiency with different NA. (d) Simulation results of bandwidth and collecting efficiency comparison of different grating couplers.

### 5.1.2 Fabrication

To validate our design, we aimed to experimentally verify the relationship between coupling efficiency to a microscopy system and the period of the grating coupler. As shown in Figure 5.10, we propose to fabricate a suspended waveguide with grating couplers at both sides. One is used to couple the light into the waveguide, the other one to out couple that light into an objective lens. The period of the in-couple grating is kept constant (such that the power in each waveguide is the same); we only vary the period of the out coupling grating coupler. In this way, we can measure the out coupling efficiency versus the grating period.

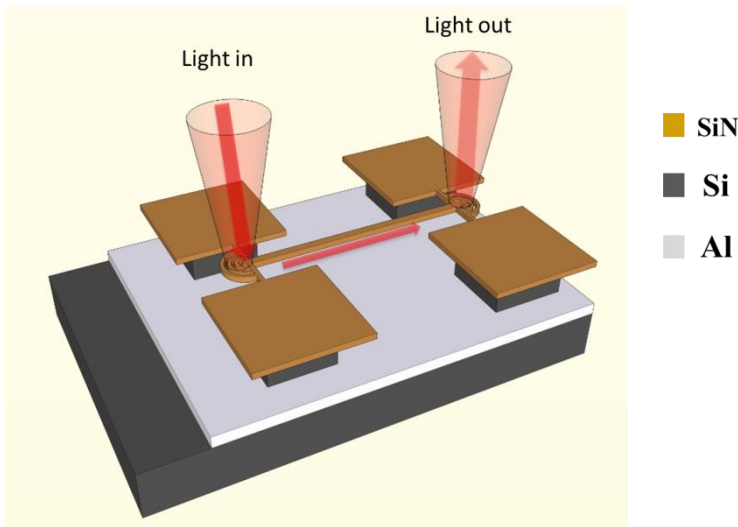


**Figure 5.10:** Proposed device structure to measure the efficiency of the ultra-compact grating coupler. The structure contains suspended waveguide with grating couplers at both sides.

We fabricated the test structures by electron beam lithography (e-beam). Figure 5.11 schematically shows the fabrication flow. First, 50nm Al is deposited onto a silicon wafer by an electron beam evaporation process. This layer is used to enhance the substrate reflection. A thin layer of Al oxide (5 nm) and silicon oxide (5 nm) are then deposited on the Al layer to protect it from oxidation and wet etching. Then an amorphous silicon (a-Si) layer is deposited by an optimized plasma enhanced chemical vapor deposition (PECVD) process performed at a temperature of 180 °C. This layer serves as a sacrificial layer during the wet etching. The targeted thickness is 950 nm, which is the optimized

layer thickness between the grating and the substrate derived from the simulation shown in Figure 5.8(a).

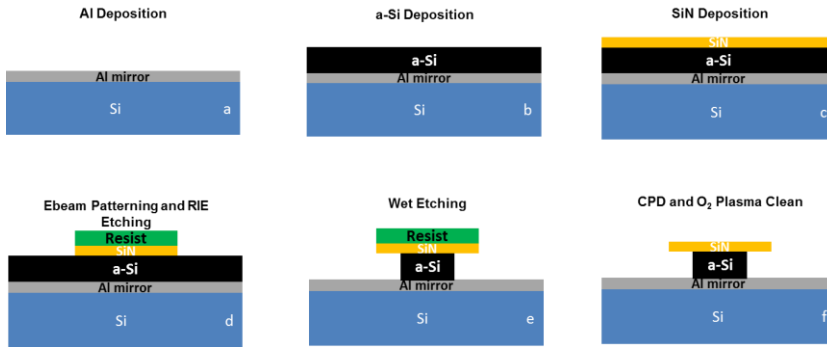


**Figure 5.11:** Schematics of the fabrication flow. (a) Deposition of 50 nm Aluminium layer on top of the silicon substrate. Thin layer of Aluminium oxide (5 nm) and silicon oxide (5 nm) are later deposited on the Al layer to protect the Al layer from oxidation and wet etching. (b) 950 nm of a-Si is deposited on top of Al layer. (c) 220 nm of SiN is deposited on top of a-Si layer as the waveguide layer. (d) E-beam is used to pattern the test structure and RIE etching transfers the pattern from e-beam resist to SiN layer. (e) Wet etching is used to undercut the grating and the waveguide. Some a-Si is left to support the pillar, as shown in the figure. (f) CPD process is used to release the structure and oxygen plasma cleaning is used to remove the residual e-beam resist.

A 220 nm thick H-F SiN layer is then deposited onto the a-Si layer by a PECVD process, carried out 180 °C and an RF bias 30 W at 13.56 MHz. The latter is optimized to obtain tensile strain in the deposited SiN layer, which guarantees good suspension after releasing the whole structure. Next, the grating coupler and waveguide structures are patterned using electron beam lithography (Raith Voyager). As mentioned in Section 2, a small beam (280nm in length) is added at each side, between the grating coupler and the waveguide, to support the whole structure with the attached pillars. The length of the suspended waveguide has been set to 35  $\mu\text{m}$ , ensuring sufficient separation of the input and output grating couplers, while being short enough to avoid the collapsing of the structure. An optimized reactive ion etching (RIE) process is used to transfer the pattern to the SiN layer [34]. An alkaline based Tetramethylammonium hydroxide (TMAH) wet etch step is carried out at 65 °C to remove the a-Si layer. Then a critical point drying (CPD) process is carried out to release the structure. Finally, oxygen plasma cleaning is needed to remove the residual e-beam resist.

As we discussed in Chapter 3.4, the L-F SiN layer has compressive stress, which will cause the suspended waveguide and free hanging structure to bend

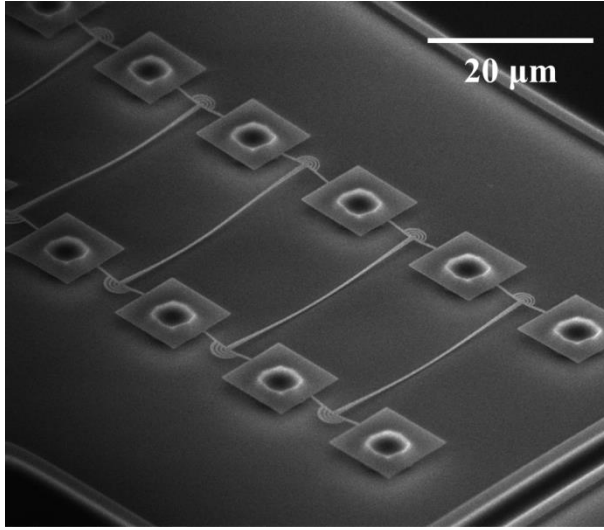


**Figure 5.12:** SEM picture of the structures after release with L-F H-SiN layer. From the picture. The compressive stress introduced by the SiN layer leads to a failure released structure.

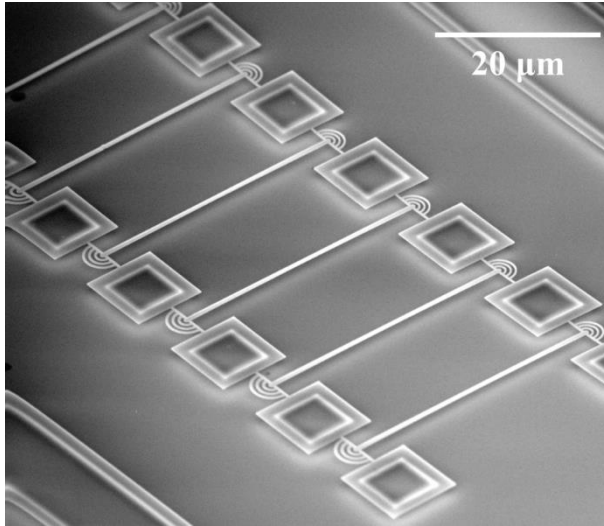


**Figure 5.13:** SEM picture of fabricated device array with H-F SiN layers. The tensile stress introduced by the SiN layer guarantees a successful release after wet etching.

after releasing the structure. Figure 5.12 shows a typical failure structure with L-F SiN layers deposited with PECVD. From the picture, downwards bending suspended waveguide can be seen, leading to a collapsed waveguide. Moreover,

with the existence of the compressive stress, the free hanging gratings at each side of the waveguide are also randomly bending upwards and downwards, leading to a non-controllable  $D_{\text{clad}}$  distance, which is also not desired.

Figure 5.13 shows the fabricated device array with H-F SiN layer. The tensile stress introduced by the SiN layer guarantees a successful release after wet etching. No bending in the suspending waveguide and grating region can be observed. With the tension from the SiN layer, the  $D_{\text{clad}}$  distance will be the same as the thickness of the a-Si layer. That helps to accurate control the  $D_{\text{clad}}$  which can maximize the efficient of the grating coupler.

### 5.1.3 Characterization

We measured the grating coupler structure efficiency using a microscopy system setup. Figure 5.14 shows the scheme of the measurement arrangement. The beam from the He-Ne laser has been adjusted so that the input beam is perpendicular to the surface of the sample. The laser beam is focused on the input grating coupler by the objective lens from the setup while the iris diaphragm blocks the reflection from the input beam and lets the light coupled out from the second grating pass through in the image plane. The intensity of the light coupled out can be measured after the iris by a detector. The insert of

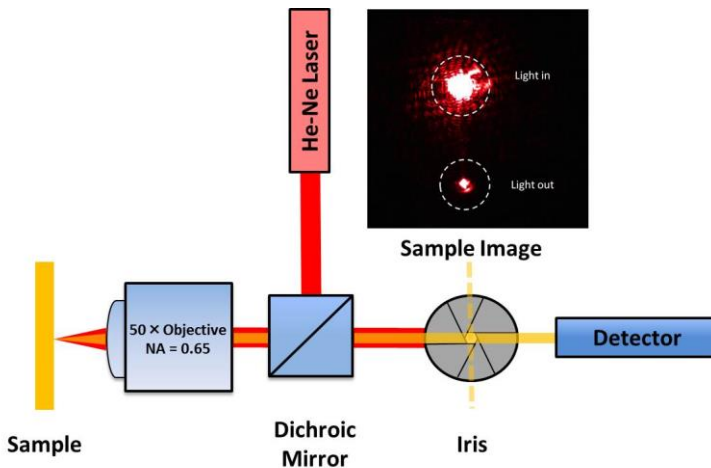


**Figure 5.14:** Microscopy system setup for the measurement. The laser is focused by a lens with  $NA = 0.65$ . There is an iris to block the reflection from the input laser in the image plane. The light from the out coupling grating can be measured with the detector. Insert: optical microscope picture of the grating couplers with input reflection and output spot (without the iris).

Figure 5.14 shows an image of the sample with the laser input turned on. We can clearly see a good separation between the reflection of the input beam and the light coupled out from the opposite coupler. The input intensity of the beam can be calibrated by measuring its reflection. We use a standard bare silicon wafer with known reflectivity (34.8%) to calibrate the reflection. By doing the calibration, the input beam intensity can be extracted. With the calibrated input beam, we can measure the reflection of the Al layer, which is 80.5%. The waveguide propagation loss can be estimated from previous measurement results [34], and is only a few dB per centimeter. Given the total length of the suspended waveguide is 35  $\mu\text{m}$  this results in a negligible loss. The main insertion loss is coming from the mode mismatch between the focused Gaussian beam of the laser and the input grating coupler. We have simulated the coupling efficiency between this Gaussian beam and the suspended waveguide with the grating coupler. For a Gaussian beam with a 1.5  $\mu\text{m}$  waist radius (as measured), the simulation shows 15.9% of the light can be coupled to the fundamental TE mode through the grating structure with 560 nm period (as shown in Figure 5.15).

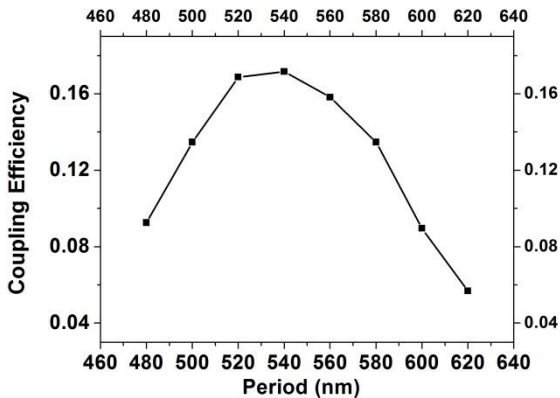


**Figure 5.15:** 1.5  $\mu\text{m}$  waist radius Gaussian laser beam coupling in efficiency with changed grating period.

Figure 5.16 shows the measured coupling efficiency versus the period of the second grating coupler. Also the simulated coupling efficiency is shown. As expected, the coupling efficiency is strongly dependent on the grating coupler's period. The maximum efficiency is achieved for a period of 620 nm, in which case 53% of the light from the TE mode from the waveguide can be coupled out by the grating coupler to the microscope. The measured results agree well with the simulated results. The remaining difference with simulated results might be related to an overestimation of the light coupled in the input grating coupler or

small deviations in the fabricated structure and in particular the exact distance towards the substrate.

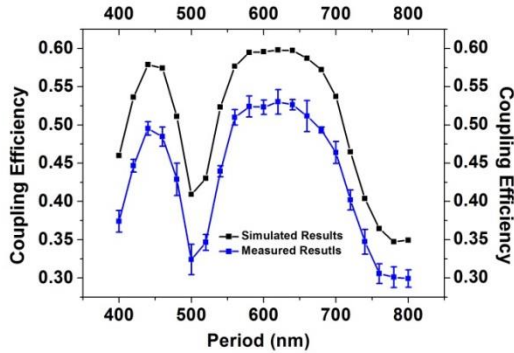


**Figure 5.16:** Measurement results: the black curve is the simulated power couple to a microscopy system with  $NA=0.65$ ; the blue curve is the measured results with a 950 nm distance between the grating coupler and the Al substrate.

#### 5.1.4 Conclusion and discussion

In conclusion, we have demonstrated the design, fabrication and characterization of an ultra-compact SiN grating coupler. The grating coupler is designed to maximize the coupling between a suspended SiN waveguide and a microscopy system. With the optimized parameters and using only 3 periods, we have experimentally demonstrated a 53% coupling efficiency from the fundamental TE mode (@ 632.8 nm) to a microscopy system with 0.65 NA. Simulations show that for an  $NA = 0.95$  it should be possible to increase the coupling efficiency above 75%. For standard grating coupler can provide 4dB loss for the waveguide to fiber coupling @900 nm, which is about 40% coupling efficiency [28]. Around 116 nm 1dB bandwidth can be theoretically achieved, due to the high contrast of the grating and a large collection angle from the microscopy system. The coupling efficiency can be further improved by using a more complicated distributed Bragg reflector layer on top of the substrate to improve the reflection compared to the currently used Al-mirror. Using a lens with a larger NA will also improve the coupling efficiency. Using a non-uniform grating period can help to reduce the return loss and also further improve the coupling efficiency.

## 5.2 Waveguide with embedded monolayer QDs

In this section, we fabricate waveguides with a patterned monolayer of QDs embedded. The proposed device structure has been shown in Figure 5.17. The structures are similar to those used for the ultra-compact SiN grating coupler characterization, except that the grating couplers at both side are identical (period = 620 nm).

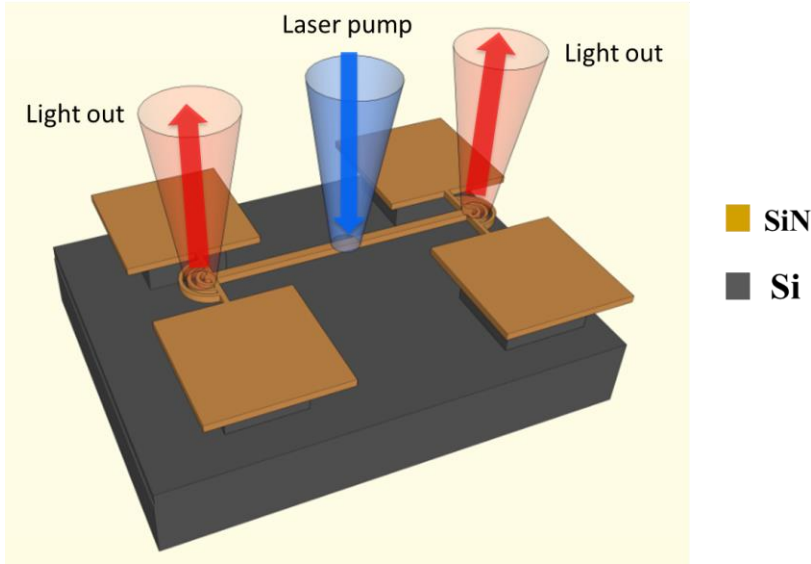


**Figure 5.17:** Proposed device structure to embed monolayer QDs into waveguide. Optimized grating couplers are at both sides. The QDs section will be pumped by a blue laser and emission will be coupled into waveguide mode and couple out by the grating coupler at both sides.

Small patches of QDs will be embedded in the suspended waveguide. Then we will check if the emission from the embedded QDs pumped with a laser beam can be collected from the grating region. This is an intermediate step towards the demonstration of an on-chip single photon source..

### 5.2.1 Fabrication

We fabricated the structure proposed in Figure 5.17 by e-beam lithography. Figure 5.18 schematically shows the fabrication flow. First, a 110 nm H-F H-SiN layer is deposited on top of a Si substrate. Later, an e-beam patterning process is used to define the Au markers for the following overlay exposures. A 50 nm thick Au layer is deposited onto the sample by an electron beam

evaporation process, followed by a lift off process to form the markers on the SiN layer. With the patterned Au marker, a first e-beam patterning process is used to define the colloidal QDs pattern, combining an L-B process and lift off. Later, another layer of H-F L-SiN is deposited on top to encapsulate the colloidal QDs. Note that low temperature SiN is used here to not only better preserve the photoluminescence of the embedded colloidal QDs, but also because it provides a low background fluorescence from the SiN layer (see chapter 3). A second e-beam step is used to pattern the grating and waveguide. Note that the waveguide width is 600 nm, and the grating couplers' period is 620 nm, as optimized in last section. After RIE etching to transfer the patterning to the SiN layer, an alkaline based TMAH wet etch step at 65 °C is carried out to partly remove the Si substrate layer. Then a critical point drying (CPD) process is carried out to release the free hanging structure. Finally, oxygen plasma cleaning is needed to remove the residual e-beam resist.

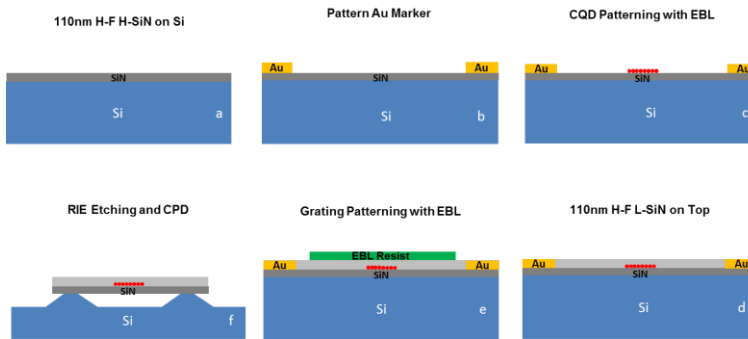


**Figure 5.18:** Schematics of the fabrication flow. (a) Deposition of 110 nm H-F H-SiN layer on top of the silicon substrate. (b) Au marker patterning has been done with e-beam and lift off process (c) First overlay e-beam and L-B process is used to pattern the monolayer colloidal QDs layer (d) 110 nm H-F L-SiN is deposited to encapsulate the colloidal QDs layer (e) Second overlay e-beam is use to pattern the grating (f) Alkaline based TMAH wet etching is used to remove the silicon under the waveguide and make the structure free hanging. CPD process is used to release the structure and oxygen plasma cleaning is used to remove the residual e-beam resist.

SEM is used to check the quality of the monolayer QDs layer patterned by e-beam lithography, L-B deposition and lift off. Figure 5.19(a) shows the result, indicating a well patterned 50 nm wide monolayer of colloidal QDs with almost no cracks.

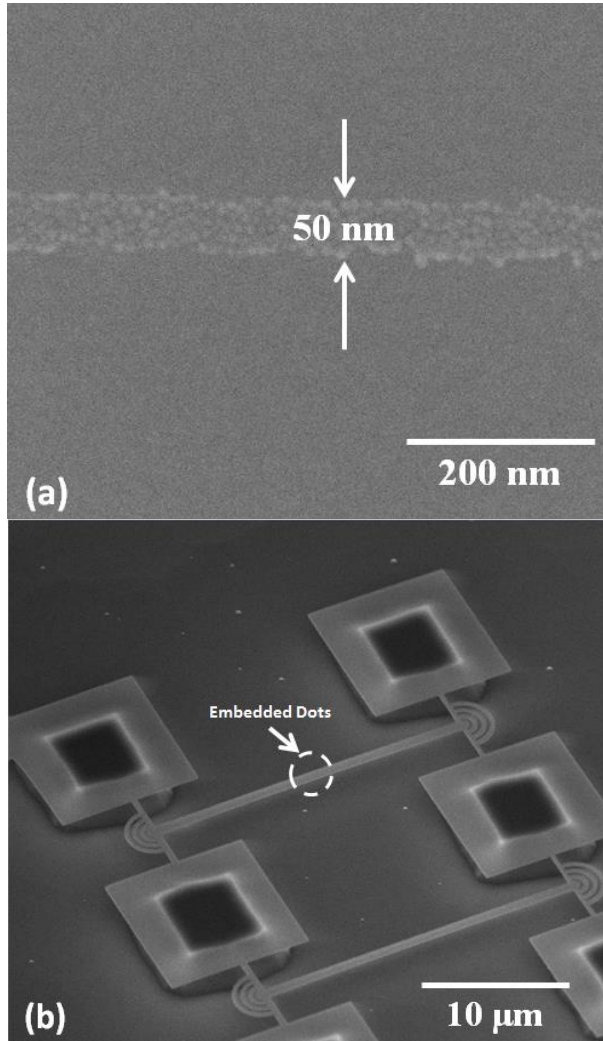


**Figure 5.19:** SEM image of the fabricated sample. (a) The monolayer QDs layer deposited on top of the SiN layer by overlay e-beam, L-B process and lift off process. The strip QDs layer has a width about 50 nm. (b) The fabricated sample after the CPD release. The whole device is free hanging. The embedded QDs are in the middle of the free hanging waveguide.

A SEM image has been taken after releasing the waveguide. Figure 5.19(b) shows the fabricated sample after the CPD release. The tensile stress from the H-F SiN layer guarantees a successful release with good free hanging

waveguide arrays. Note that the embedded monolayer QD patches are in the middle of the free hanging waveguide.

## 5.2.2 Characterization

The device characterization is done in a micro-photoluminescence ( $\mu$ -pl) setup. The schematic of the  $\mu$ -pl setup diagram has been show in Figure 5.20.

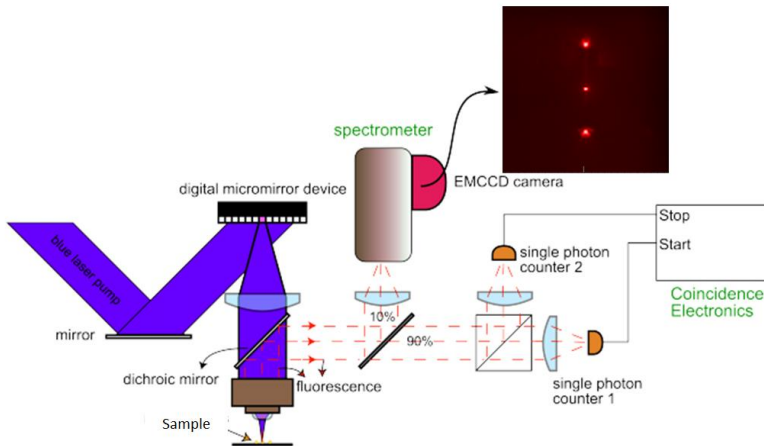


**Figure 5.20:** The schematic of the micro-photoluminescence setup diagram.

The excitation beam of the setup is produced by a PicoQuant LDH-DC-440M laser diode. The laser diode operates in either cw or pulsed mode (in which case it produces short pulses of less than 100 ps). The excitation beam was focused on the sample using an Olympus objective lens (100x 0.75NA) and shaped using a digital micro-mirror device (Texas Instrument, 0.55" XGA 2x LVDS DMD) to allow custom excitation patterns (e.g. exciting a single diffraction-limited spot or the entire field of view). The luminescence was collected through the same objective lens and directed either to an imaging spectrometer (Andor Shamrock 330i) equipped with an EMCCD camera (Andor iXon DU897) or to a Hanbury-Brown Twiss setup. The imaging spectrometer was used to image the surface of the sample and record the emission spectra of the sample. The Hanbury-Brown Twiss setup consisted of a 50/50 beam-splitter, two silicon photon-counting modules (Perkin Elmer SPCM-AQRH-14) with a time resolution of about 500 ps, and start-stop time correlator (PicoQuant, PicoHarp 300). The Hanbury-Brown Twiss setup was used to measure the luminescence decay, the  $g(2)$ -function and the blinking statistics of samples.

We use the cw mode of the laser diode to characterize our fabricated sample. The beam is adjusted to a small spot with diameter around  $1.5 \mu\text{m}$  to only pump the embedded dots in the middle of the free hanging waveguide using the digital

micro-mirror device. The power intensity of the pumping spot is around  $300 \text{ W/cm}^2$ . Figure 5.21 shows the image captured with the EMCCD camera. A top view SEM image of the device structure, approximately scaled to the same dimensions is also shown in Figure 5.20.

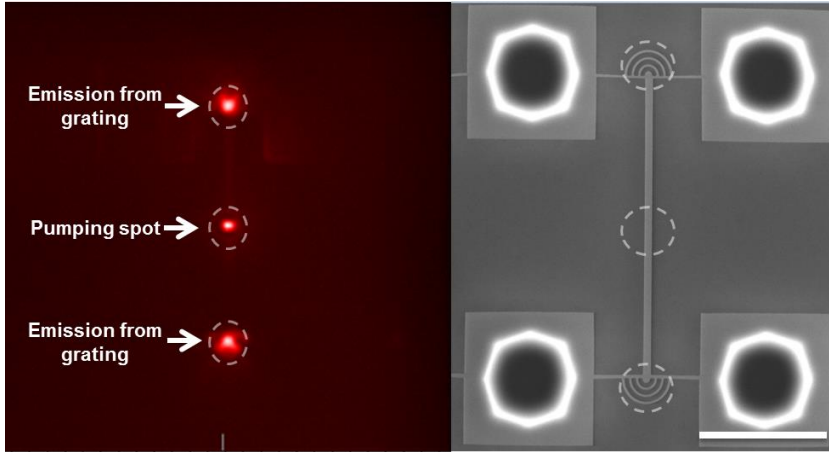


**Figure 5.21:** The captured image with the EMCCD camera. A top view SEM image of the device structure is also shown on the right as a compare. The scale bar is  $10 \mu\text{m}$ .

The result shows that part of the emission of the embedded monolayer colloidal QDs is not coupled into the optical mode of the suspended waveguide. This is expected from the simulation results in Figure 5.2. For the suspended SiN waveguide with  $220 \text{ nm}$  by  $600 \text{ nm}$  geometry, we expect 24% of the emission can be coupled to the waveguide and 76% of the emission is coupled to the free space. Taking into account the coupling efficiencies, we expect 9.6% emission will be coupled out from the grating. The emission can be observed in the grating area from Figure 5.21. The not coupled emission goes to free space and gets captured by the EMCCD, which can be seen from Figure 5.21 as the emission from the pumping spot. However, also part of the emission of the embedded QDs is coupled to the optical mode of the suspended waveguide. This emission is coupled out by the grating couplers sitting at both ends of the waveguide, which can be seen from the captured image. We actually measure and compare the counts in the embedded region and the two grating coupler regions. which shows a ratio around 3.5:1. These measurement results are close to the simulation results.

We further analyse the spectra of the different emitted beams with the imaging spectrometer from the setup. Figure 5.22 shows the spectral information of the emission from the pumping spot and the grating coupler. The spectrum from the pumping spot region is approximately centered at  $620 \text{ nm}$  and exhibits

a FWHM of 42 nm, which is the same as the colloidal QDs spot in the solution phase. This spectrum indicated the emission from this region is mainly from the embedded dots and not from the background photoluminescence from the SiN layer (the spectrum of background photoluminescence is generally much wider). The spectra from the grating couplers region are approximately centered at 615 nm and exhibits a FWHM around 42 nm. This result indicates also the captured emission from the grating couplers region mainly comes from the emission coupled to the waveguide mode.

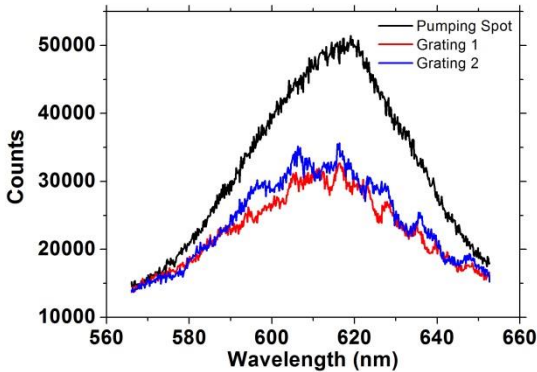


**Figure 5.22:** The spectra of the emission from the pumping spot and the grating couplers using the imaging spectrometer.

### 5.2.3 Conclusion and discussion

We have demonstrated devices with nano-patches monolayer colloidal QDs embedded in suspended SiN waveguide. The embedded QDs still maintain their emission after the full process. Part of the emission from these embedded QDs is coupled to the optical mode of the suspended waveguide. The ultra-compact grating coupler can efficiently out couple light from the waveguide to a  $\mu$ -pl setup. This is an important intermediate step towards the on-chip single photon source.

The current QD-pattern contained approximately 200 QDs. The measured emission reaches  $\pm 10.5$  times above the background noise level. To realize a real on-chip single photon source and be able to measure its emission with this setup, there is still work to be done. The single dot patterning technique should be used, to pattern single colloidal QDs in the desired position. To further improve the coupling efficiency, optimized waveguide dimension should be used to enhance the coupling efficiency between the embedded QD and the optical waveguide mode. And an Al metal layer should be used

to enhance the grating couplers coupling efficiency to the  $\mu$ -pl setup, similar to what has been done in the previous section.

For the possible device layout for future practical devices, we could locally under etch the SiN waveguide with optimized dimension containing a single colloidal QD to enhance the coupling efficiency, while leaving the other parts of the waveguide attached to the substrate to maintain a robust structure. Also other more efficient coupling structures can replace the ultra-compact grating coupler. E.g. an inverted taper can be used, to maximize the coupling between the waveguide and collecting fiber.

### 5.3 Conclusion

In this chapter, we present the work on the integration of patches of mono layer colloidal QDs in a suspended SiN waveguide aiming to demonstrate on chip single photon sources. In the first part of this chapter, we show the design, fabrication and characterization of an ultra-compact grating coupler optimized to maximize the power coupling between the suspended SiN waveguide and a microscopy system. The experiment shows up to 53% power coupling efficiency to a  $NA = 0.65$  microscopy system can be achieved. And our simulations show the coupling efficiency can increase up to 75% for microscopy system with  $NA = 0.95$ . Also our grating is very compact with a size only 4 by 2  $\mu\text{m}^2$ , which is suitable for the microscopy system with limited field-of-view. In the second part, we embedded patches of monolayer colloidal QDs into the suspended SiN waveguide. The photoluminescence properties of the colloidal QDs can still be preserved after all the fabrication processes. The emission from the embedded colloidal QDs can be well coupled to the waveguide. With the help of the optimized ultra-compact grating, the emission coupled to the waveguide can be also well coupled out and captured by the microscopy systems. In combination with the earlier developed single colloidal QD patterning technique, our work shows the potential to realize single photon sources with our optimized hybrid integration platform.

## References

- [1] Aharonovich, Igor, and Elke Neu. "Diamond nanophotonics." *Advanced Optical Materials* 2, no. 10 (2014): 911-928.
- [2] Morfa, Anthony J., Brant C. Gibson, Matthias Karg, Timothy J. Karle, Andrew D. Greentree, Paul Mulvaney, and Snjezana Tomljenovic-Hanic. "Single-photon emission and quantum characterization of zinc oxide defects." *Nano letters* 12, no. 2 (2012): 949-954.
- [3] Utikal, Tobias, Vahid Sandoghdar, Lutz Petersen, Alois Renn, Stephan Güzinger, and Emanuel Eichhammer. "Detection, spectroscopy and state preparation of a single praseodymium ion in a crystal." *Nature Commun.* 5, no. arXiv: 1310.8180 (2013): 3627.
- [4] Ma, Xuedan, Nicolai F. Hartmann, Jon KS Baldwin, Stephen K. Doorn, and Han Htoon. "Room-temperature single-photon generation from solitary dopants of carbon nanotubes." *Nature nanotechnology* 10, no. 8 (2015): 671-675.
- [5] He, Yu-Ming, Genevieve Clark, John R. Schaibley, Yu He, Ming-Cheng Chen, Yu-Jia Wei, Xing Ding et al. "Single quantum emitters in monolayer semiconductors." *Nature nanotechnology* 10, no. 6 (2015): 497-502.
- [6] Buckley, Sonia, Kelley Rivoire, and Jelena Vučković. "Engineered quantum dot single-photon sources." *Reports on Progress in Physics* 75, no. 12 (2012): 126503.
- [7] Patel, Raj B., Anthony J. Bennett, Ian Farrer, Christine A. Nicoll, David A. Ritchie, and Andrew J. Shields. "Two-photon interference of the emission from electrically tunable remote quantum dots." *Nature photonics* 4, no. 9 (2010): 632-635.
- [8] Sapienza, Luca, Marcelo Davanço, Antonio Badolato, and Kartik Srinivasan. "Nanoscale optical positioning of single quantum dots for bright and pure single-photon emission." *Nature communications* 6 (2015).
- [9] Brokmann, Xavier, E. Giacobino, Maxime Dahan, and Jean-Pierre Hermier. "Highly efficient triggered emission of single photons by colloidal CdSe/ZnS nanocrystals." *Applied Physics Letters* 85, no. 5 (2004): 712-714.
- [10] Brokmann, X., G. Messin, P. Desbiolles, E. Giacobino, M. Dahan, and J. P. Hermier. "Colloidal CdSe/ZnS quantum dots as single-photon sources." *New Journal of Physics* 6, no. 1 (2004): 99.
- [11] Pisanello, Ferruccio, Luigi Martiradonna, Godefroy Leménaquer, Piernicola Spinicelli, Angela Fiore, Liberato Manna, Jean-Pierre Hermier et al. "Room

- temperature-dipolelike single photon source with a colloidal dot-in-rod." *Applied Physics Letters* 96, no. 3 (2010): 033101.
- [12] Pisanello, Ferruccio, Godefroy Leméner, Luigi Martiradonna, Luigi Carbone, Stefano Vezzoli, Pascal Desfonds, Pantaleo Davide Cozzoli et al. "Non - blinking single - photon generation with anisotropic colloidal nanocrystals: towards room - temperature, efficient, colloidal quantum sources." *Advanced Materials* 25, no. 14 (2013): 1974-1980.
- [13] Michler, P., A. Imamoglu, M. D. Mason, and P. J. Carlson. "Quantum correlation among photons from a single quantum dot at room temperature." *Nature* 406, no. 6799 (2000): 968.
- [14] Lounis, B., H. A. Bechtel, D. Gerion, P. Alivisatos, and W. E. Moerner. "Photon antibunching in single CdSe/ZnS quantum dot fluorescence." *Chemical Physics Letters* 329, no. 5 (2000): 399-404.
- [15] Lai, Wei-Cheng, Swapnajit Chakravarty, Yi Zou, and Ray T. Chen. "Silicon nano-membrane based photonic crystal microcavities for high sensitivity bio-sensing." *Optics letters* 37, no. 7 (2012): 1208-1210.
- [16] Nitkowski, Arthur, Long Chen, and Michal Lipson. "Cavity-enhanced on-chip absorption spectroscopy using microring resonators." *Optics express* 16, no. 16 (2008): 11930-11936.
- [17] Politi, Alberto, Martin J. Cryan, John G. Rarity, Siyuan Yu, and Jeremy L. O'Brien. "Silica-on-silicon waveguide quantum circuits." *Science* 320, no. 5876 (2008): 646-649.
- [18] Imamog, A., David D. Awschalom, Guido Burkard, David P. DiVincenzo, Daniel Loss, M. Sherwin, and A. Small. "Quantum information processing using quantum dot spins and cavity QED." *Physical review letters* 83, no. 20 (1999): 4204.
- [19] Wang, Jianwei, Stefano Paesani, Raffaele Santagati, Sebastian Knauer, Antonio A. Gentile, Nathan Wiebe, Maurangelo Petruzzella et al. "Experimental quantum Hamiltonian learning." *Nature Physics*. Jun 1; **13**(6):551-5 (2017).
- [20] Xie, Weiqiang, Raquel Gomes, Tangi Aubert, Suzanne Bisschop, Yunpeng Zhu, Zeger Hens, Edouard Brainis, and Dries Van Thourhout. "Nanoscale and Single-Dot Patterning of Colloidal Quantum Dots." *Nano letters* 15, no. 11 (2015): 7481-7487.
- [21] Bisschop, Suzanne, Antoine Guille, Dries Van Thourhout, Zeger Hens, and Edouard Brainis. "Broadband enhancement of single photon emission and

- polarization dependent coupling in silicon nitride waveguides." *Optics express* 23, no. 11 (2015): 13713-13724.
- [22] V. Chandrasekaran, D. Dupont, M. D. Tessier, E. Drijvers, T. Aubert, Z. Hens, and E. Brainis. "New materials for Single Photon Emission from Colloidal Quantum Dots " Proceedings Symposium IEEE Photonics Society Benelux, 2016, Ghent, Belgium
- [23] Y. Zhu, J. Wang, W. Xie, B. Tian, Y. Li, E. Brainis, Y. Jiao, D. Van Thourhout, "Ultra-compact Silicon Nitride Grating Coupler for Microscope System", *Optics Express*, 25(26), p.33297-33305 (2017)
- [24] D. Taillaert, W. Bogaerts, P. Bienstman, T.F. Krauss, P. Van Daele, I. Moerman, S. Verstuyft, K. De Mesel, R. Baets, "An out-of-plane grating coupler for efficient butt-coupling between compact planar waveguides and single-mode fibers," *IEEE Journal of Quantum Electronics*. Jul, 38(7):949-55 (2000).
- [25] D. Taillaert, P. Bienstman, and R. Baets, "Compact efficient broadband grating coupler for silicon-on-insulator waveguides," *Optics Letters* 29(23), 2749-2751 (2004).
- [26] A. Mekis, S. Gloeckner, G.Masini, A. Narasimha, T. Pinguet, S. Sahni, P. De Dobbelaere, "A grating-coupler-enabled CMOS photonics platform," *IEEE Journal of Selected Topics in Quantum Electronics*, May, 17(3):597-608 (2011).
- [27] G. Roelkens, D. Van Thourhout, R.Baets, "High efficiency Silicon-on-Insulator grating coupler based on a poly-Silicon overlay," *Optics Express*, Nov 27; 14(24):11622-30 (2006).
- [28] A.Z. Subramanian, S. Selvaraja, P. Verheyen, A. Dhakal, K. Komorowska, and R. Baets, "Near-infrared grating couplers for silicon nitride photonic wires," *IEEE Photonics Technology Letters* 24(19), pp.1700-1703 (2012).
- [29] D. Bouwmeester, J. Pan, K. Mattle, M. Eibl, H. Weinfurter, and A. Zeilinger, "Experimental quantum teleportation," *Nature* **390**, 575–9 (1997).
- [30] E. Knill, R. Laflamme, and G. J. Milburn, "A scheme for efficient quantum computation with linear optics," *Nature* **409**, 4652 (2001).
- [31] Nielsen, Michael A., and I. L. Chuang. "Quantum computation." *Quantum Information*. Cambridge University Press, Cambridge (2000).
- [32] J.W. Silverstone, D. Bonneau, K. Ohira, N. Suzuki, H. Yoshida, N. Iizuka, M. Ezaki, CM. Natarajan, MG. Tanner, RH. Hadfield, V.Zwiller, "On-chip quantum interference between silicon photon-pair sources," *Nature Photonics*. Feb 1, 8(2):104-8 (2014).

- [33] CP. Dietrich, A. Fiore, MG. Thompson, M. Kamp, S.Höfling, “GaAs integrated quantum photonics: Towards compact and multi-functional quantum photonic integrated circuits,” *Laser & Photonics Reviews*, Sep 1 (2016).
- [34] Xie, W., Zhu, Y., Aubert, T., Verstuyft, S., Hens, Z. and Van Thourhout, D., “Low-loss silicon nitride waveguide hybridly integrated with colloidal quantum dots,” *Optics Express* 23(9), pp.12152-12160 (2015).
- [35] Faraon, A., Fushman, I., Englund, D., Stoltz, N., Petroff, P. and Vučković, J., “Dipole induced transparency in waveguide coupled photonic crystal cavities”, *Optics Express* 16(16), pp.12154-12162 (2008).
- [36] Luxmoore, I.J., Wasley, N.A., Ramsay, A.J., Thijssen, A.C.T., Oulton, R., Hugues, M., Kasture, S., Achanta, V.G., Fox, A.M. and Skolnick, M.S., “ Interfacing spins in an InGaAs quantum dot to a semiconductor waveguide circuit using emitted photons”, *Physical Review Letters* 110(3), p.037402 (2013).
- [37] Sun, J., Timurdogan, E., Yaacobi, A., Hosseini, E.S. and Watts, M.R., “Large-scale nanophotonic phased array”, *Nature* 493(7431), pp.195-199 (2013).
- [38] Rahim, A., Ryckeboer, E., Subramanian, A.Z., Clemmen, S., Kuyken, B., Dhakal, A., Raza, A., Hermans, A., Muneeb, M., Dhoore, S. and Li, Y., 2017. “Expanding the Silicon Photonics Portfolio With Silicon Nitride Photonic Integrated Circuits,” *Journal of Lightwave Technology*, **35**(4), pp.639-649 (2017).

# 6

## Conclusions and perspectives

### 6.1 Conclusions

In this thesis, we have developed a heterogeneous integration platform aiming to combine the excellent optical emission properties of colloidal QDs with a SiN waveguide platform. First, a passive SiN photonics waveguide platform based on a plasma enhanced chemical vapor deposition process has been developed and demonstrated. With the optimized deposition and etching recipe, we have achieved low-loss waveguides with  $\sim 1$  dB/cm optical loss for wavelengths around 900 nm. Moreover, we demonstrated colloidal QDs can be embedded in between of two SiN layers without quenching their photoluminescence. With the optimized deposition and etching recipe, a SiN waveguide containing one embedded layer of colloidal QDs can still achieve low waveguide losses as low as  $\sim 2$ -3 dB/cm, which is already sufficiently low for many applications relying on integrated waveguide circuits. We have also characterized the stress and material fluorescence of SiN layers deposited with different recipes, as these might impact the different targeted applications.

To investigate the properties of the embedded QDs further, we developed a waveguide based variable stripe length method to measure the modal gain coefficient of waveguide, which contains embedded colloidal QDs. We showed the embedded QDs exhibit amplified spontaneous emission (ASE) under femtosecond pulsed laser pumping. The results are consistent with the results we got from Transient Absorption Spectroscopy (TAS) on solution phase QDs.

Exploiting the optical gain properties from the embedded colloidal QDs, we have designed, fabricated and characterized on-chip distributed feedback lasers based on this hybrid SiN colloidal QDs waveguide platform. The laser shows

single mode lasing under femtosecond pulsed laser pumping with a lasing threshold around  $12 \mu\text{J}/\text{cm}^2$  @ 400 nm. To further investigate the laser performance, we used a Q-switched frequency doubled Nd:YAG laser (532 nm) with a 7 nanosecond pulse width and a 938 Hz repetition rate for pumping. The laser still shows lasing with a lasing threshold around  $270 \mu\text{J}/\text{cm}^2$ . For the *flash* CdSe/CdS core/shell colloidal QDs we used for our laser, measurement in section 4.1 shows these dots exhibit a  $2 \text{ ns}^{-1}$  biexciton decay rate, which corresponds to a 500 ps biexciton lifetime. Compared to this biexciton lifetime, our 7 ns pump actually can be considered as quasi-CW pumping. This opens strong prospects in terms of CW operation and, consequently, an extended application potential. The intrinsic combination with the mature SiN-waveguide platform then immediately opens the path towards more complex devices such as tunable lasers and arrays of single mode lasers or integration with passive structures such as on-chip spectrometers.

Since colloidal QDs are solution processed materials at low cost, which can be directly patterned onto a substrate, we have also used this feature and demonstrated on-chip gain-coupled DFB lasers based on an optimized colloidal QDs patterning technique. The laser shows single mode lasing without phase shifter in the middle of the laser cavity. The threshold is around  $950 \mu\text{J}/\text{cm}^2$  @532 nm Nd:YAG laser pumping.

We have also tried to combine the colloidal nano-platelets (NPLs) with the SiN waveguide platform. The NPLs still show their ASE after embedding them into the SiN layer stacks. A material gain coefficient around  $3500 \text{ cm}^{-1}$  can be extracted from the VSL measurement. This showcases the versatility of the hybrid integrated photonics platform we developed and the fact that our optimized hybrid SiN waveguide platform can potentially be used for integration with other colloidal nano-crystals.

Colloidal QDs are candidates as single photon emitter at room temperature. Our developed SiN waveguide platform can also be used to integrate colloidal QDs to realize on-chip single photon sources. However, to characterize these QDs based integrated single photon sources and the associated photonic circuits, compact, efficient and broad-band couplers are needed to couple light from a chip to an objective. In this thesis, we have demonstrated the design, fabrication and characterization of an ultra-compact SiN grating coupler. The grating coupler is designed to maximize the coupling between a suspended SiN waveguide and a microscopy system. With the optimized parameters and using only 3 periods, we have experimentally demonstrated a 53% coupling efficiency from the fundamental TE mode (@ 632.8 nm) to a microscopy system with 0.65 NA. Around 116 nm 1dB bandwidth can be theoretically achieved, due to the high contrast of the grating and a large collection angle from the microscopy system. We also have embedded nano patches of monolayer colloidal QDs into

the suspended waveguide. With optical pumping, the emission from the embedded nano patches can be well coupled to the optical mode of the waveguide. With the help of the grating coupler, these emissions can be also coupled out to the collection objective.

## 6.2 Perspectives

For the on-chip lasers using colloidal QDs as a gain material, the next target is to demonstrate lasing under CW optical pumping. One direction is to further improve the optical gain properties from the colloidal QDs themselves. Colloidal QDs with longer biexciton lifetime and higher gain coefficient will be beneficial to lower the lasing threshold and allow for a CW pumped laser. Using inorganic-halide-capped colloidal QDs could increase the packing density in the active layer, resulting in a higher modal gain and better thermal conductivity. A ZnS-shell can be used to cap the colloidal QDs and better preserve their optical properties after encapsulation into the SiN layer stack. The other direction is to improve from the integration side. Currently, the waveguide is defined with a one-step etching. We could use different optimized etching recipes to etch the SiN and colloidal QDs layer separately to achieve a smoother waveguide sidewall for higher Q optical cavities. Another option is to pattern the colloidal QDs layer inside the waveguide to avoid etching the colloidal QDs layer. Other than the potential optimization which can improve the Q factor of the cavity, it is relevant to provide on-chip heat sinking structures to avoid local heating that quenches the colloidal QDs' emission.

Also for the on-chip single photon sources using colloidal QDs, further work is needed. The single dot pattern technique should be used, to pattern single colloidal QDs in the desired position. To further improve the coupling efficiency, optimized waveguide dimension should be used to enhance the coupling efficiency between the embedded QD and the optical waveguide mode. And an Al metal layer should be used to enhance the grating couplers coupling efficiency to the  $\mu$ -pl setup.



